A new flow analysis technique: Fourier-Averaged Navier-Stokes equations

by

Benjamin R. S. Freeman

a thesis submitted in partial fulfilment of the requirements for the degree of

master of science

Department of MECHANICAL ENGINEERING

University of Alberta

© Benjamin R. S. Freeman, 2023

ABSTRACT

This dissertation introduces a new flow analysis technique based on the Fourier-Averaged Navier-Stokes (FANS) equations. It details their application to educing the effect of fluid forces on flow physics. The derivation and interpretation of the method is described, and details of how to calculate key terms are presented. The method is then applied to several case studies to illustrate its applicability, interpretability, and limitations across flows of different complexities. Three of these case studies are used to evaluate the characteristics of FANS and verify that the method is interpretable. Specifically, conclusions are made from FANS and these conclusions are compared to known physics and the findings of other methods. These cases consist of 2D laminar vortex shedding over a square cylinder, axisymmetric swirling jet flow, and irregular asymmetric vortex shedding over a pair of square cylinders. FANS is shown to be simple to calculate and easy to interpret for analysing fluid flows with increasing complexity, including cases with broadband spectrum. The final case study looks at 3D flow over normally-oriented, thin flat plates. This case illustrates the practicality of FANS in exploring unknown physics in a fully 3D, nonperiodic flow. Three flat plates with varying end conditions are compared to investigate the effect of end plates on the fluctuating and mean flow. FANS shows the effect of friction from the end plates on dampening transverse velocity fluctuations. It also shows how interaction between the rollers with the boundary layer induces coherent spanwise flow at the shedding frequency. Overall, the proposed method is shown to be applicable in investigating the physics of flows with cyclic characteristics, including those with nonperiodic behaviour.

PREFACE

Elements of this thesis are the result of a collaborative effort between myself and my supervisor, Dr. Arman Hemmati. Some sections of Chapters 2 and 3, as well as the entirety of Chapters 5 and 6 have been thoroughly reviewed and edited by Dr. Hemmati and Dr. R.J. Martinuzzi, as co-authors in publications under review in the Journal of Fluid Mechanics and International Journal of Heat and Fluid Flow. The concept, derivation, simulation setup and analysis, and figures are my own work.

For Julia

ACKNOWLEDGEMENTS

There are obviously a huge number of people who are directly and indirectly involved in completing a project of this scale.

First, the people who supported or inspired this project. I would like to thank Dr. Arman Hemmati for agreeing to do this project with me despite the risks involved, and for his patience and guidance through this process. As well, I would like to thank Dr. Robert Martinuzzi for his expertise and support on the project. I think it suffices to say that without these two men this idea would not have gotten anywhere. I am endlessly grateful to Suyash Verma and Shubham Goswami for their help on so many aspects of this degree: admin, simulations, presentations, papers, analysis, and so on. There are also professors whose effective teaching indirectly inspired this project: Drs. Marc Secanell, Sina Ghaemi, and Carlos Lange.

Second, on a personal level I would obviously like to thank my family, particularly my father and sister Pam for insufficiently discouraging me from pursuing grad school. Thanks to friends and roommates Revan, Rebecca, Kieran, Kayla, Kyle, John, and Thomas for making the first, pandemic-driven year of this degree bearable. And of course, I would like to thank my girlfriend, Julia, for her love for me and her (increasingly strained) patience for my meandering career trajectory.

Finally, I would like to thank Alberta Innovates, the National Science and Engineering Research Council, and Canada First Research Excellence for their financial support of this work.

Contents

List of Tables

List of Figures

LIST OF ABBREVIATIONS, SYMBOLS, AND NOMENCLATURE

Latin Symbols

j	Imaginary unit
h	plate height (chord)
W	plate spanwise width
AR	aspect ratio
Re	Reynolds number
t	time
$\mathbf{u}$	Instantaneous vector velocity field
U_∞	free-stream velocity
u	Cartesian $x-$wise instantaneous velocity component
v	Cartesian $y-$wise instantaneous velocity component
w	Cartesian $z-$wise instantaneous velocity component
p	Instantaneous pressure field
$\mathbf{U}$	Mean velocity field
P	Mean pressure Field
$\hat{\mathbf{u}}_k$	kth vector velocity Fourier mode
$\hat{p}_k$	kth pressure Fourier mode
$C[\square, \square]$	Discrete convection operator
$G[\square]$	Discrete gradient operator

$L[\square]$	Discrete Laplacian operator
T	Interval length
St	Strouhal number
f	Frequency
$f^* = fh/U_\infty$	Reduced frequency
$C_d = \frac{2F_d}{\rho U_\infty^2 Wh}$	coefficient of drag
$C_l = \frac{2F_l}{\rho U_\infty^2 Wh}$	coefficient of lift
$C_s = \frac{2F_s}{\rho U_\infty^2 Wh}$	coefficient of Span force
F_d	drag force
F_l	lift force
F_s	span force
L_w	mean recirculation length

Greek Symbols

η	Kolmogorov length scale
ω	vorticity
$\tilde{\chi}$	Continuous Fourier Stresses
χ	Discrete Fourier Stresses
ν	kinematic viscosity
λ_1	BMD complex mode bispectrum
ϕ_{k+l}	BMD Bispectral mode
$\phi_{k \circ l}$	BMD cross-frequency field

$\psi_{k,l}$	BMD interaction map

Other Symbols

$\nabla\square$	Continuous Gradient operator
$\nabla\cdot\square$	Continuous Divergence operator
$\nabla^2\square$	Continuous Laplacian operator

Abbreviations

$2D$	Two Dimensional
$3D$	Three Dimensional
NS	Navier-Stokes
DNS	Direct Numerical Simulation
LES	Large Eddy Simulation
$RANS$	Reynolds Averaged Navier Stokes
$URANS$	Unsteady Reynolds Averaged Navier Stokes
$FANS$	Fourier-Averaged Navier Stokes
RMS	Root-Mean-Square
LSA	Linear Stability Analysis
SCM	Self-Consistent Method
POD	Proper Orthogonal Decomposition
$SPOD$	Spectral Proper Orthogonal Decomposition
DMD	Dynamic Mode Decomposition
BMD	Bispectral Mode Decomposition
DFT	Discrete Fourier Transform

FFT	Fast Fourier Transform
$PISO$	Pressure-Implicit with Splitting of Operators
$GAMG$	Generalized Geometric-Algebraic Multigrid
$PBiCG$	Preconditioned Biconjugate Gradient
$DILU$	Diagonal-based Incomplete Lower Upper
UT	Unsteady Term
VB	Vortex Breakdown

Chapter 1

INTRODUCTION

A new flow analysis technique based on Fourier decomposition of the Navier-Stokes equations is presented in this dissertation. The equations are used as a momentum balance at each timescale. This work details the derivation of the equations and interprets the resulting terms. Analysis based on this momentum balance is applied to several case studies to establish their applicability and interpretation. The strength of the new technique for providing insights into new flow dynamics is then examined through a complex wake problem with that is not well understood.

1.1 Overview

Despite the complex nature of turbulent phenomena, incompressible Newtonian fluids behave in a way that satisfies the governing equations of fluid mechanics, the Navier-Stokes equations (Drazin and Riley, 2006). These equations describe the momentum transport within fluids, and when coupled with the conservation of mass, can be used to simulate fluid flow (Ferziger et al., 2019). However, the Navier-Stokes equations are nonlinear, with no exact solution in most practical problems (Drazin and Riley, 2006). Moreover, turbulence is a multi-scale phenomenon (Durbin and Pettersson, 2011), which has led to several efforts to simplify the description of turbulent flow and find more intuitive understandings of the mechanisms that govern it.

One avenue to arriving at simpler descriptions of fluid flow lies in manipulating the governing equations. Simple averaging of the flow over multiple realizations of a flow leads to the Reynolds-Averaged Navier-Stokes (RANS) equations. These equations describe fluid flow in terms of the mean and covariance of the velocity and pressure fields over time. This simplifies the description by only considering these statistical quantities at the expense of time-dependent information (Durbin and Pettersson, 2011). However, other operations have been applied to the Navier-Stokes equations besides averaging to gain insight into flow dynamics. For instance, linearization of the governing equations has been widely applied to investigate other characteristics of fluid flow (Seydel, 2010). These linearizations can then be used to find transitions in the flow, such as steady to unsteady (Schmid and Henningson, 2001) in Linear Stability Analysis, or from two-dimensional to three-dimensional flow in Floquet analysis (Barkley and Henderson, 1996; Gioria et al., 2009). Generally speaking, the governing equations are highly malleable and they can be repurposed for specialized analysis, with the proper operations.

The complexity of turbulent flow has also led to methods that simplify the description of a flow without any consideration of the governing equations (Foias et al., 2001). These methods, such as Proper Orthogonal Decomposition, Dynamic Mode Decomposition, and their variants (Lumley, 1970; Chen et al., 2012; Noack et al., 2016; Sieber et al., 2016; Towne et al., 2018), arise from nonlinear dynamics treatments of fluid flow. Commonly, a decomposition method will produce a series of modes and dynamics that represent the spatial and temporal characteristics of the flow, respectively. These simplified descriptions are highly useful when an equation-free representations of a flow is desirable, such as in control systems (Kutz et al., 2016). Decomposition methods have been widely and successfully used to investigate flow physics. Applications have included Ahmed body models (He et al., 2021), jets (Schmid et al., 2011; Towne et al., 2018), flat plate wakes (Agrey, 2021), wind turbines (Araya et al., 2017; Schmidt and Colonius, 2020), and fluid-structure interaction (Khalid et al., 2020).

Simplified representations of the flow provided by decomposition methods can suffer in terms of interpretability (Towne et al., 2018; Sieber et al., 2016). Important characteristics of the flow can

also be lost in the simplification process (Rowley and Dawson, 2017). Likewise, the modes provided by a model reduction can be related to each other through their dynamics (Noack et al., 2016), but this does not provide key spatial information. Occasionally, modes are reincorporated into the governing equations through a Galerkin projection of the equations onto the modes (Noack et al., 2003, 2016; Kutz et al., 2016). Reincorporating them produces a dynamical system that allows for future predictions of the flow behaviour using momentum conservation and the interactions between modes. However, this entails a volume integration that removes all spatial information about the system. Spatial information about inter-mode interactions is only provided by a small number of highly specialized methods, such as higher order spectral methods (Qing, 2004), or Bispectral Mode Decomposition (Schmidt, 2020). However, these methods do not consider the momentum or energy transport that governs fluid flow. As a result, these methods do not have a mechanism to relate nonlinear interactions to other processes that are important, such as diffusion and pressure. Consequently, there is room to use the governing equations alongside a modal decomposition to provide useful spatial information about the momentum transport processes that drive the flow.

The concept of decomposing force or energy fluctuations into manageable components have appeared previously in literature. Two are (1) decomposition of fluctuations into mean, coherent, and incoherent components, and (2) phase averaging. These two methods are closely related, as the phase-averaging is sometimes used to extract coherence (Balachandar et al., 1997; Braun et al., 2020). Phase averaged or coherent-incoherent representations have been used in determining the effect of different mechanisms on forces (Najjar and Balachandar, 1998), Reynolds stresses (Balachandar et al., 1997), and turbulent kinetic energy (Braun et al., 2020). However, there are limitations to these techniques. For instance, basic phase averaging is sensitive to modulation in the phase between cycles. For signals with natural variation in phase, additional techniques must be applied to ensure consistency (Ostermann et al., 2015; Bauer et al., 2022), making the application and interpretation of the method more complex.

In this dissertation, modal representation of the Navier-Stokes equations is proposed to analyze flow data. Fourier decomposition is used for the modes as this process is simple and interpretable.

This decomposition of the Navier-Stokes equations, referred to here as the Fourier-Averaged Navier-Stokes (FANS) equations, is used to simplify the description of the forces that transport momentum within a fluid flow. This simplification is achieved by representing the flow as a collection of modes, while also leveraging information from the governing equations.

Fourier decomposition is a simple method that is widely used in literature, both by itself and as a part of other methods (Noack et al., 2003; Rowley et al., 2009; Chen et al., 2012; Sieber et al., 2016; Towne et al., 2018; Schmidt, 2020). However, it requires a cyclic behaviour in the flow. For the purposes of this thesis, cyclic and periodic flows are defined as follows:

Cyclic flow: a flow with distinct patterns that recur over time. The recurrences can occur regularly or irregularly.

Periodic flows: a subset of cyclic flows that recur exactly over regular intervals. That is, a periodic flow has a finite period T and satisfies the property $q(t + T) = q(t)$ for all quantities (e.g. pressure and velocity). The frequency spectrum of a periodic flow will consist of a fundamental frequency and harmonics.

Nonperiodic flows: cyclic flows without an identifiable period over which they recur. Nonperiodic flows have broadband frequency spectrum.

Cyclic and periodic behaviours are common in fluid flows. Examples of these flows appear in jets (Schmid et al., 2011; Herrada et al., 2009; Schmidt and Colonius, 2020), bluff body wakes (Mantic-Lugo et al., 2015; Hemmati et al., 2016a; Jang et al., 2021; Braun et al., 2020), cavities (Meliga, 2017). Periodic behaviour may be enforced through gusts (Afgan et al., 2013), fluttering or oscillating foils (Garrick, 1936; Verma et al., 2022), or rotating machinery (Hall et al., 2002; Beneddine, 2017; Araya et al., 2017).

The newly proposed technique is evaluated in terms of its application, interpretation, and limitations in this dissertation. This is accomplished through several case studies. Cases include periodic and nonperiodic 2D wakes of bluff bodies, multi-frequency jet flow, and 3D wakes. The

technique is also evaluated in terms of its ability to educe new physics in a study of 3D wake dynamics behind thin flat plates with different end conditions.

1.2 Motivations and Objectives

The governing equations of fluid dynamics are highly accurate, but they are impractical to use in many cases due to their complexity (Foias et al., 2001; Durbin and Pettersson, 2011; Kutz et al., 2016; Ferziger et al., 2019). Ways around this complexity have been sought out for decades. As a result, the equations can be simplified to fit specialized purposes (Durbin and Pettersson, 2011; Girimaji, 2005; Seydel, 2010), or ignored entirely (Kutz et al., 2016). However, equation-free methods, which do not consider the governing equations, can lack crucial spatial information about the interactions that govern the flow (Schmidt, 2020). A few methods that exist to find these interactions do not have ways to compare them to the other governing processes (Qing, 2004; Schmidt, 2020). As a result, this work proposes incorporating Fourier decomposition of the flow in time into the Navier-Stokes equations. This technique provides a new method to simplify fluid flow analysis. This representation will provide useful, interpretable information that can be connected to the flow physics. This dissertation will introduce and derive the method, and then test it against several case studies to show its interpretability. This method is widely applicable in fluid mechanics due to the prevalence of cyclic characteristics in many flows (Hall et al., 2002; Schmid et al., 2011; Ma et al., 2017; Mantic-Lugo et al., 2015; Hemmati et al., 2016a).

The main objective of this dissertation is to develop, apply, and evaluate a new flow analysis technique that is easy to implement and interpret. The specific objectives of this work are to:

1. Detail the derivation and implementation of momentum analysis using Fourier decomposition applied to the Navier-Stokes equations.

2. Verify that the equations are indeed applicable to analysis of flows by cross-comparing interpretation of the momentum terms to established physics.

3. Assess the limitations of the method by applying it to multiple cases of increasing complexity. This will consist of 2D and 3D flows, including both periodic and nonperiodic cases.

4. Assess the ability of the method to educe meaningful, new physics in a typical use case - namely, a nonperiodic, fully 3D wake.

1.3 Novelty

The primary novelty of this research is the direct application of FANS equations to analyse flow data. This form of analysis allows for studying the transport processes that govern velocity fluctuations in flows with recurring characteristics. The strength and interpretability of FANS in exploring new flow physics is also investigated, by characterizing the effect of end conditions on 3D wake dynamics behind thin flat plates.

1.4 Structure of the thesis

In this dissertation, Chapter 2 discusses the background of turbulence, decompositions of the Navier-Stokes equations, and decomposition methods, with a focus on the Discrete Fourier Transform and its applications to other order reduction and simulation methods.

Chapter 3 derives the Fourier-Averaged Navier Stokes equations in discrete and continuous form and details the interpretation and naming of each term in the equations. The setup and interpretation of terms in these equations serves as the starting point to using these equations to analysing unsteady flows. Some details of the application of these terms to experimental or simulation data will also be elaborated.

Chapter 4 introduces the case studies that will be used to explore the application and interpretation of FANS results. The computational method and descriptions of the basic physics that will be relevant to further chapters will be elaborated here. The setup of four case studies are

explained here. The first three involve known physics, while the final case is a more complex 3D wake problem.

Three case studies will be presented in chapter 5 to validate the usage of FANS against established physics. The first case study consists of analysis of 2 dimensional, periodic flow around a square cylinder. This flow results in a simple Karman vortex street with regular shedding. The flow can be reduced to the mean flow and a pair of Fourier modes. The simplicity and periodicity of the flow makes it an ideal candidate for the FANS analysis. The second case study involves a swirling, axisymmetric jet impinging on a wall. This flow remains periodic, but has a highly modulated time signature, and a larger number of relevant Fourier modes. Finally, a non-periodic (irregular vortex shedding) case of flow over two cylinders arranged side by side is investigated. The addition of a non-periodic case is used to establish the applicability of the method to a case with broadband Fourier spectrum.

Chapter 6 builds upon the understanding of FANS interpretation in studying the effect of end-conditions on the wakes of normal flat plates, which are complex, 3D and underexplored. FANS terms are compared between cases to establish the ability of FANS-based analysis to explore unknown physics that result in complex flow dynamics.

Chapter 7 contains the concluding arguments on the derivation and application of the FANS equations for analysing flow data. Some discussions are also included on possible future directions to enhance the applicability of the FANS equations.

Chapter 2

BACKGROUND

2.1 Turbulence and the Navier-Stokes equations

Fluid flow is governed by the Navier-Stokes equations, which describe the conservation of momentum in a fluid from a continuum mechanics perspective (Drazin and Riley, 2006). These equations were developed in the 19th century by Claude-Louis Navier and George Gabriel Stokes, and relate the evolution of the velocity or momentum field to the pressure, shear, and body forces of a flow (Bistafa, 2018). At their most complex, they represent the forces that govern fluid motion in terms of the changes in density, pressure, body forces, and velocity in a fluid (Batchelor, 1999):

$$\rho\frac{\partial \mathbf{u}}{\partial t} + \rho\mathbf{u}\cdot\nabla\mathbf{u} = \rho\mathbf{F} - \nabla p + \nabla\cdot\left(\rho\nu\left(\nabla\mathbf{u} + (\nabla\mathbf{u})^T - \frac{2}{3}\nabla\cdot\mathbf{u}\right)\right), \tag{2.1}$$

where ρ is the fluid density, $\mathbf{u}$ is the velocity field, F are the body forces, p is the pressure, and ν is the kinematic viscosity. These equations are unclosed, as the density, velocity, and pressure represent five unknowns in three equations. Equations for the conservation of mass, energy, and an "equation of state" that relates the pressure, density, and temperature are used to close the system (Schlichting et al., 2000). The full equations are only necessary for applications with large temperature gradients or gases traveling at high speeds (roughly 30% of the speed of sound). For many applications, a simplified form of these equations, referred to as the incompressible Navier-Stokes equations may

be used instead:

$$\frac{\partial \mathbf{u}}{\partial t} + \mathbf{u} \cdot \nabla \mathbf{u} = -\frac{1}{\rho} \nabla p + \nu \nabla^2 \mathbf{u}, \tag{2.2}$$

where the equations are closed with the conservation of mass, known as the continuity equation:

$$\nabla \cdot \mathbf{u} = 0. \tag{2.3}$$

The Navier-Stokes equations (Equation 2.2) are second-order, nonlinear partial differential equations. As a result, their behaviour is complicated and does not admit many analytical solutions. However, there are general qualitative characteristics to assist in analyzing these equations. The first is that the equations are independent of scale and their behaviour only depends on the Reynolds number $Re = U_\infty h/\nu$, where U_∞ and h are some appropriate velocity and length scale, respectively (Aris, 1989). When Re is below a certain threshold, which varies from case to case, the flow is "steady" (u and p are unchanging in time) and "laminar", which means that the streamlines of the flow stay organized and parallel to one another. Flow in 2D or axisymmetric geometries will also remain 2D or axisymmetric (Schlichting et al., 2000). As Re increases, the convective term becomes more important, which induces unsteadiness. Further increasing Re leads to breaking of symmetries and laminarity, which leads to the flow transitioning to turbulence (Durbin and Pettersson, 2011). Turbulence is a qualitative description and its exact definition varies from amongst scientists. Generally agreed-upon characteristics of turbulent flow include three-dimensionality, chaotic flow, variations in time and space, and prevalence of several time- and length scales (Lumley, 1970; Durbin and Pettersson, 2011; Holmes et al., 2012). Turbulent flows exhibit greater mixing and higher gradients than laminar flows, which has significant consequences for heat transfer, mixing, and forces (Durbin and Pettersson, 2011).

Simply describing a flow as turbulent is not helpful. More specifically, there is a desire for a more complete understanding of the structure and consequences of turbulent flows. Significant progress has been made on this problem since 1932, when Horace Lamb reportedly stated: "I am an old man now, and when I die and go to Heaven there are two matters on which I hope for

enlightenment. One is quantum electrodynamics, and the other is the turbulent motion of fluids. And about the former I am really rather optimistic." (Goldstein, 1969). One piece of progress is the understanding that even turbulent flows contain "coherent structures" (CS), which are spatially and temporally coherent vortical patterns that may be identified using a number of criteria (Jeong and Hussain, 1995). Another is the utilization and practicality of statistical and spectral representations of turbulence (Lumley, 1970; Foias et al., 2001; Durbin and Pettersson, 2011). The success of decomposition methods in simplifying turbulent dynamics has also been established (Foias et al., 2001; Rowley and Dawson, 2017). A brief overview of the latter two topics will be presented in the following sections.

2.2 Reynolds Averaged Navier Stokes Equations

The Navier-Stokes equations (Equation 2.2) have been repeatedly shown to be accurate for incompressible Newtonian fluids, even when highly turbulent (Drazin and Riley, 2006; Durbin and Pettersson, 2011). However, the full, time-dependent equations are not practical for most analysis (Foias et al., 2001). Thus, mathematically manipulated versions of these equations are used instead. Perhaps the most famous version of the momentum equations in turbulence are the Reynolds Averaged Navier-Stokes (RANS) equations. These equations arise from decomposing the instantaneous flow field ($\mathbf{u}$) into mean ($\mathbf{U}$) and time-varying ($\mathbf{u}'$) components (Durbin and Pettersson, 2011; Foias et al., 2001):

$$\mathbf{u} = \mathbf{U}(\mathbf{x}) + \mathbf{u}'(\mathbf{x}, t). \tag{2.4}$$

This decomposition can be inserted into Equation 2.2, which is then averaged to obtain:

$$\mathbf{U} \cdot \nabla \mathbf{U} = -\nabla P + \nu \nabla^2 \mathbf{U} - \overline{\mathbf{u}' \cdot \nabla \mathbf{u}'}. \tag{2.5}$$

The final term ($\overline{\mathbf{u}' \cdot \nabla \mathbf{u}'}$) is known as the "Reynolds stresses", which creates a closure problem. The Reynolds stresses arise from convection of the fluctuating part of a turbulent flow, and tend to have

a diffusive effect on the mean field (Durbin and Pettersson, 2011). This means that the Reynolds stresses must be modeled, which has spawned several strategies (e.g. Durbin and Pettersson, 2011; Jakirlić and Maduta, 2015; Duraisamy et al., 2019; Krumbein et al., 2020). The Reynolds stresses lead to the concept of "turbulent kinetic energy" ($k = \overline{\mathbf{u}' \cdot \mathbf{u}'}$), which enables modeling of turbulent effects (Durbin and Pettersson, 2011). A transport equation for k can also be derived based on Reynolds transport theorem. The balance of terms in this transport equation is known as the turbulent kinetic energy budget, which can be used to study the origins and effects of fluctuating components of turbulent flow (Durbin and Pettersson, 2011; Hemmati et al., 2018; Agrey, 2021).

Manipulations of the Navier-Stokes equations for modeling purposes and flow analyses are not limited to the basic RANS equations. Allowing the statistics of a turbulent flow to evolve over time leads to the Unsteady-RANS (URANS) equations (Durbin and Pettersson, 2011). For simulations, URANS is simple to implement from normal RANS formulations, as it only requires the addition of a time-derivative term. URANS has been shown to better replicate experimental results than steady RANS (e.g. Girimaji, 2005; Iaccarino et al., 2003; Jakirlić and Maduta, 2015). More advanced methods have also been proposed, which attempt to bridge between direct numerical simulation (DNS) of the Navier-Stokes equations, Large Eddy Simulation (LES) and RANS/URANS models. These methods involve further manipulations to the Navier-Stokes equations or turbulent transport equations (Jakirlić and Maduta, 2015; Menter and Egorov, 2010; Girimaji, 2005).

2.3 Decomposition methods

Just as the motivation of the RANS method is to simplify usage of the Navier-Stokes equations by applying an averaging process, there is a similar motivation to simplify the representation of a turbulent flow when its behaviour has already been measured. The belief that descriptions of turbulent flows can be substantially simplified without losing critical spatial or temporal information is also supported by theoretical treatment (Foias et al., 2001). As a result, there have been many methods proposed over the past decades to investigate the underlying characteristics of turbulent

flows (e.g., as detailed in Picard and Delville, 2000; Noack et al., 2003; Qing, 2004; Chen et al., 2012; Sieber et al., 2016; Schmidt, 2020). These methods have succeeded in representing the flow dynamics associated with complex systems. However, it remains that the interpretation of these processes in the physical domain is often difficult and non-intuitive.

There are several approaches to analyse these systems through dimensionality reduction. Two well-established methods are Proper Orthogonal Decomposition (POD, Lumley, 1970) and Dynamic Mode Decomposition (DMD, Chen et al., 2012), which are linear decompositions of the flow dynamics. The two methods decompose a set of snapshots of a velocity field into a series of spatially-varying modes ϕ_i with time-varying coefficients a_i, which are called the dynamics:

$$\mathbf{u}(\mathbf{x}, t) = \sum_i a_i(t)\phi_i(\mathbf{x}). \tag{2.6}$$

The methods use different strategies to calculate the modes and dynamics. In POD, Singular Value Decomposition (SVD) is performed on N snapshots of flow data $\mathbf{u_n}$:

$$\mathbf{Q} = \mathbf{U}\Sigma\mathbf{V}^H. \tag{2.7}$$

Where $\mathbf{Q} = [\mathbf{u}_0\, \mathbf{u}_1 \ldots \mathbf{u}_{N-1}]$ is an $3m$ by N matrix whose columns are made up of the flow snapshots (m being the number of sample points). The columns of $\mathbf{U}$, which is a $3m$ by N matrix, are the spatial modes, $\mathbf{V}$ is an N by N matrix of time-varying information, and Σ is an N by N diagonal matrix that determines the magnitudes of the dynamics. SVD optimizes the modes in terms of energy content, so the large-scale dynamics are captured compactly. For instance, Wang et al. (2022) used POD on the streamwise component of a boundary layer to investigate the properties of wall-attached eddies, arguing that the resulting modes were a strong statistical representation of the eddies. He et al. (2021) used POD to compare the processes of wake asymmetry and switching on two Ahmed bodies, using the modes to aid analysis of the two mechanisms. While interactions between modes can be identified, e.g. through phase portraits of the temporal dynamics or establishing a dynamical system that relates them (Noack et al., 2003), the physical interpretation

of these interactions remains challenging. Likewise, one limitation of POD is that isolating the highest-energy modes does not always capture important dynamics. Low-energy modes can be highly important to the evolution of a flow as noted by Rowley and Dawson (2017).

In Dynamic Mode Decomposition snapshots of the flow variables are used to identify a sparser set of dynamics (Schmid et al., 2011). DMD "fits" an approximate linear system that describes the transitions between a series of flow snapshots. That is, given N snapshots of data u_n, DMD finds a matrix $\mathbf{A}$ that satisfies

$$\mathbf{u}_{n+1} = \mathbf{A}\mathbf{u}_n \tag{2.8}$$

for all n. Eigenvalue decomposition is then performed on the matrix $\mathbf{A}$ in order to find the modes and dynamics. There is a rich mathematical background to DMD through its connection to the Koopman operator, as described for instance in Chen et al. (2012). There are several variant methods derived by changing the optimization target or adding a mode ranking process, e.g. in the Optimized DMD of Chen et al. (2012) or Recursive DMD of Noack et al. (2016). An early example on the topic is the jet study of Schmid et al. (2011), where it was shown that DMD could successfully isolate the large-scale structures, frequencies, and forcing response of jet flows from PIV and Schlieren snapshots. Gómez et al. (2014) used DMD on a turbulent pipe flow, where they successfully linked DMD results about the energy and frequency content of turbulence to predictions from resolvent analysis. This investigation showed how DMD results could connect to the fundamental fluid dynamics equations. However, this connection required an external method in the form of resolvent analysis. The study of Jang et al. (2021) on oscillatory flow over a surface-mounted circular cylinder showed that DMD was able to accurately model the bed shear stress with relatively few modes, but required a large number of modes to represent the flow around the cylinder body. This highlights the potential difficulties and limitations regarding sparsity in DMD representations.

POD and DMD are widely and successfully employed, but gaps remain in their applicability and interpretability. POD loses dynamical information due to averaging, and returns modes that are only coherent in space. It can also result in modes that contain contributions from several

timescales, reducing interpretability. Meanwhile, DMD does not have an energy optimization procedure, and will restrict modes to single frequencies, which may not be desirable in flows with broadband frequency content. Two distinct methods have been introduced that address these shortcomings, both referred to as Spectral Proper Orthogonal Decomposition (SPOD). The first corresponds originally to a formulation of POD used by Lumley and named by Picard and Delville (2000), which was then formalized by Towne et al. (2018). The second is a method based on POD, which was introduced by Sieber et al. (2016) and expanded upon by Sieber (2021). It includes a filtering strategy that can be adjusted to replicate results from POD or a discrete Fourier Transform (DFT), depending on the selected filter. These methods will be elaborated upon as part of a more complete discussion of Fourier decomposition for turbulent flows in the following section.

2.3.1 Temporal Fourier Decomposition

There is a large body of research and application of Fourier decomposition for characterizing the behaviour of time-dependent flows. Fourier decomposition is applied through a Discrete Fourier Transform (DFT) on discretely sampled data. The output of the DFT can be used to analyse the frequency content of force signatures or flow fields, for instance to detect the timescales associated with particular structures. This way, it is also viewed as a basic order reduction method, like POD or DMD (Noack et al., 2003; Sieber et al., 2016). In fact, Fourier decomposition and DMD are identical in some circumstances (Rowley et al., 2009; Chen et al., 2012; Towne et al., 2018). The DFT is known to be limited as it is only applicable to statistically stationary data and it does not attempt to construct modes that are energetically optimal or coherent. However, the simplicity of understanding the results of a DFT has led to its utilization in more advanced methods. Lumley (1970) originally formulated a version of POD applied to ensembles of Fourier modes that was then named Spectral Proper Orthogonal Decomposition (SPOD) by Picard and Delville (2000). The method is formulated as follows: Obtain a set of M DFTs of flow data over several windows of length N ($\hat{u}_k^i$, where $i \in M$ is the ensemble number and $k \in N$ is the mode number). Then,

collect all M estimates of a particular mode into a matrix and perform SVD:

$$[\hat{u}_k^0 \ \hat{u}_k^1 \ ... \ \hat{u}_k^{N-1}] = \mathbf{U}\Sigma\mathbf{V}^H. \tag{2.9}$$

Performing this operation on every set of Fourier modes creates a frequency-domain description of the flow in terms of $M \cdot N$ SPOD modes. The structures identified by this method are claimed by Towne et al. (2018) to evolve coherently in space and time, unlike those identified by basic POD or DMD. The modes found by this method correspond to individual frequencies due to the Fourier decomposition and are optimized in terms of energy due to the SVD.

The other formulation of SPOD, introduced by Sieber et al. (2016), uses a filter on the temporal correlation matrix of flow snapshots (the correlation matrix is often used to calculate the POD). The filter is implemented through a convolution of the correlation matrix coefficients with a windowing function of custom width (Sieber, 2021). The method recovers the Fourier modes and Power Spectral Density of the flow in the limit of filtering over the whole window. It was shown that SPOD was able to obtain "much better separation of individual fluid dynamic phenomena into single modes" (Sieber et al., 2016) compared to either POD or Fourier modes.

While these data analysis methods (i.e. POD, DMD, and both SPODs) are useful for educing structures or dynamics of particular flows, they conspicuously do not include a direct connection to the involved physical processes. This would be useful when avoiding the complexity of the full Navier-Stokes equations. For instance, a common application is a Galerkin projection of the governing equations onto the spatial modes. This approach is useful when short-term predictions of the flow dynamics are desirable (Noack et al., 2003). However, this does not provide spatial information for characterizing regions where nonlinear interactions are important (Schmidt, 2020).

Other nonlinear analysis methods include higher-order spectral methods (Qing, 2004), which introduce the idea of the "bispectrum". The bispectrum is used to characterize relationships between Fourier modes of a nonlinear system, specifically by measuring the degree of correlation between triads of frequency or wavenumber components. This makes it natural for analysing

systems with quadratic nonlinearity, such as incompressible flows described by the Navier-Stokes equations. These triadic interactions between structures at different wavenumbers have been successfully applied, for example to the turbulent kinetic energy cascade (Durbin and Pettersson, 2011). However, interactions between modes of different frequencies has been less extensively studied. Recently, the Bispectral Modal Decomposition was proposed by Schmidt (2020), which is a promising method to analyse triadic interactions through a specialized decomposition technique that maximizes the bicorrelation between frequency or wavenumber components of a flow. The quantity of interest for BMD is a vector of complex expansion coefficients ($\mathbf{a}_{k,l} = a^j_{k,l}$) for each triad ($k$, l, $k+l$) that maximizes the quantity

$$\mathbf{a}_1 = \underset{\|\mathbf{a}_{k,l}\|=1}{\arg\max} \left| \mathbf{a}^H_{k,l} \hat{\mathbf{Q}}^H_{k\circ l} \mathbf{W} \hat{\mathbf{Q}}_{k+l} \mathbf{a}_{k,l} \right|, \tag{2.10}$$

such that

$$\lambda_1 = \mathbf{a}^H_1 \hat{\mathbf{Q}}^H_{k\circ l} \mathbf{W} \hat{\mathbf{Q}}_{k+l} \mathbf{a}_1. \tag{2.11}$$

The quantity λ_1 can be interpreted as representing a maximized bicorrelation for a particular triad. $\mathbf{W}$ is a weight matrix that is used to approximate spatial integration. $\hat{\mathbf{Q}}_{k\circ l} = [\hat{\mathbf{q}}^0_k \circ \hat{\mathbf{q}}^0_l ... \hat{\mathbf{q}}^n_k \circ \hat{\mathbf{q}}^n_l]$[1], and $\hat{\mathbf{Q}}_{k+l} = [\hat{\mathbf{q}}^0_{k+l} ... \hat{\mathbf{q}}^n_{k+l}]$ are matrices formed from the Fourier modes ($\hat{\mathbf{q}}^i_k$) of sequences of snapshots that have been split into n blocks. The coefficients a_1 are then used to construct modes that represent the driving interaction and result of a triadic interaction. It relies on coincidence of local components of Fourier modes. However, this method cannot directly relate the magnitude of the nonlinear interactions to the physical transportation processes that govern the flow.

The concept of temporal Fourier decomposition have also been applied to simulation methods. Spatial Fourier modes are often used in, for example, three-dimensional simulation with a homogeneous direction (Najjar, 1994; Durbin and Pettersson, 2011) or to investigate transitions to three dimensionality (e.g. Gioria et al., 2009; Barkley and Henderson, 1996). Temporal decomposition, however, is less common. Simulation methods exploiting periodicity have been independently

[1] $\hat{\mathbf{q}}_k \circ \hat{\mathbf{q}}_l$ is the elementwise product of two vectors

introduced by three groups in the last three decades. Initially, Carte et al. (1995) introduced the Spectral Time Discretization as a method to quickly simulate flows with distinct periodicity. This method involves the assembly of a fully coupled system of equations to solve for the velocity and pressure Fourier modes of a flow. Independently, Hall et al. (2002) developed a similar method for turbomachinery applications called the Harmonic Balance Technique, which built upon earlier research on calculating harmonics based on a known mean flow. The Harmonic Balance is typically applied to cases where the periodicity is applied externally, for instance in turbomachinery. The method includes compressibility effects and turbulence modeling by applying the spatial discretizations in the time domain, and then returning to the frequency domain to solve the resulting systems of equations. Development of new solvers based on the Spectral Time Discretization and Harmonic Balance Technique have continued in recent years. For example, Beneddine (2017) proposed a matrix-free, implicit treatment of the decomposed equations to address some stability issues with the Spectral time method. Another example is the Fourier-Galerkin method of Sierra-Ausin et al. (2022), which is an extension of the Harmonic Balance technique. The method compares favourably with the Spectral Time Discretization in terms of computational resources, and is able to detect the fundamental frequency of a flow during simulation.

More recently, another temporal Fourier decomposition-based method was introduced as an extension of linear stability analysis. Named the Self Consistent Method by Mantic-Lugo et al. (2015), it involves repeated application of both linear stability analysis and the decomposed momentum equations that result from applying a Fourier decomposition to the Navier-Stokes equations. The method is shown to be able to detect the growth rate and saturation amplitude of periodic wakes (Mantic-Lugo et al., 2015; Meliga, 2017) and it can be used for flow sensitivity (Meliga et al., 2016).

2.4 Background of case studies

The case studies of this dissertation involve a jet flow as well as bluff body wakes of square cylinders and flat plates. A brief background on these cases is presented here.

Bluff bodies are an important class of fluid flow due to their engineering application. These bodies are characterized by their separated flow and large drag (Roshko, 1993). Examples of these bodies are found in motor vehicles (Ahmed et al., 1984), buildings (Wang et al., 2012), energy harvesting systems (Liu and Oztekin, 2018), and solar panels (Fogaing et al., 2019). Even aerodynamic structures like wind turbines can act like bluff bodies in some circumstances (Eriksen and Krogstad, 2017; Araya et al., 2017), which has an impact on their performance.

A common feature of bluff body wakes is vortex shedding (Roshko, 1993), which is an unsteady phenomenon induced by instability of the free shear layers. Two widely studied examples include shedding from circular and square cylinders. These cases are used as a simple representative model for all bluff bodies (Williamson, 1996; Roshko, 1993; Balachandar et al., 1997; Bai and Alam, 2018). Flow over these bodies is characterized by a steady separated flow under $Re = 50$. Above this point they transition to periodic unsteady 2D vortex shedding, which also results in changes in the mean wake, such as shortening of the recirculation region (Williamson, 1996; Bai and Alam, 2018). The flow undergoes transitions to three-dimensionality around $Re = 140 - 194$ for circular cylinders (Williamson, 1996) and $Re = 150 - 200$ for squares. There is a wide range for this transition as it is highly sensitive to experimental conditions. The transition to three-dimensionality is also swiftly followed by breakdown of the periodicity and onset of turbulence. The difference in geometry significantly alters mean and fluctuating properties of the wake. The most significant change lies in the sharp edges at the leading and trailing edge of the square cylinder, which defines the separation points of the flow. Meanwhile, the separation point of a square cylinder is unfixed (Bai and Alam, 2018), which results in altered physics.

Multiple adjacent bluff bodies are also important to characterize due to the interaction between the wakes. For instance, when two cylinders are arranged side-by-side, the resulting combined wake changes based on the size of the gap (Ma et al., 2017). For small gaps - less than half of

the cylinder diameter - little fluid is able to penetrate between the two cylinders and the overall effect is that of a single object. For large gaps, there is little interaction between the cylinders and their wakes are independent. However, this behaviour does not uniformly change between the two extremes. For some gap sizes, the flow through the gap forms a jet that interacts strongly with the shedding behind the cylinders. This leads to an overall asymmetry in the flow and a phenomenon known as flip-flopping (Carini et al., 2014; Burattini and Agrawal, 2013; Ma et al., 2017). The flip-flopping process involves random changes in the jet direction over time, which affects the drag and lift forces on each cylinder.

Another important concept in bluff body turbulence research is the idea of "nominal two-dimensionality". Nominally two-dimensional bodies have a span that is much larger than their length or chord. The hypothesis behind nominally 2D flow is that with an appropriately designed experimental setup, extraneous three-dimensionality due to end effects could be eliminated (Roshko, 1993). This is important for reconciling theoretical, numerical, and experimental results on bluff body wakes (Lisoski, 1993). However, the intrinsic three-dimensionality of the flows are important (Williamson, 1996; Najjar, 1994; Hemmati et al., 2018). That is, spanwise variations of the bluff body wake arise naturally and have a significant effect on the flow. Additionally, extrinsic three-dimensionality are a major factor in the wake development and evolution, even for long bodies (Williamson, 1996).

Thin flat plates represent a particularly interesting case of bluff bodies due to the lack of an afterbody (Williamson, 1996; Balachandar et al., 1997). They are "sharp-edged", so flow separates at corners on the body (Sychev et al., 1998), and it is unable to reattach due to the thinness of the plate (Hemmati, 2016). This destabilizes the free shear layers behind the plate, and changes the mean flow characteristics with respect to other bodies. Like all bluff bodies, the flow is intrinsically three-dimensional except at very low Reynolds number ($Re < 250$) (Najjar, 1994). Consequently, the deceptively simple geometry and setup results in complicated physics. The wake of a flat plate features Karman-like vortex shedding (Braun et al., 2020), with the primary vorticity in the spanwise direction consisting of rollers. There are also spanwise structures known as ribs that

wrap around the rollers (Hemmati et al., 2018). However, the shedding is not regular and there is low-frequency modulation (Najjar and Balachandar, 1998; Wu et al., 2005). This modulation is related to changes in shedding regimes (Hemmati et al., 2016a). The regimes can be characterized by low (L), medium (M), and high (H) drag due to vortex shedding. The low regime involves a suppressed of vortex shedding process with a decrease in drag coefficient, loss of coherence in wake structures, and an elongated recirculation region. Meanwhile, the high regime has vigorous shedding and an increased drag coefficient with a shortened recirculation region, as well as coherent and long lasting ribs and rollers. The moderate regime falls between the low and high regimes in all characteristics (Hemmati et al., 2016a). Intrinsic and extrinsic three-dimensionality is also highly important for flat plates (Lisoski, 1993; Najjar and Vanka, 1995a; Braun et al., 2020). Achieving two-dimensionality can depend on the presence of walls, free surfaces, and end plates of different angles (Lisoski, 1993). Recently, Braun et al. (2020) showed that long (aspect ratio $= 38$) flat plates can exhibit a very different wake based on end conditions. In their study, an open-ended plate featured lower streamline curvature, entrainment of vorticity toward the plate, correlation of pressure and velocity signals over time, and turbulent kinetic energy dissipation compare to a plate with angled end plates. However, the spanwise variation of the flow was not characterized.

A swirling jet case is also considered in this thesis. Jets are widely studied due to their real-world applications, such as in heat transfer, deposition, and cleaning. A simple case of a jet occurs when a stream of fluid at one velocity enters a domain moving at a different velocity, such as air exiting a duct into the atmosphere (Abramovich, 1963). The result is a free-shear layer that surrounds a region of potential flow in the core of the jet. The shear layers grow as they entrain the surrounding fluid, and the jet eventually becomes self-similar (Phares et al., 2000; Durbin and Pettersson, 2011). Swirl (flow in the angular direction) is an important characteristic for jets of fluid in cylindrical domains (Herrada et al., 2009). Induced swirl changes the mechanical characteristics of the jet due to centripetal forces. Particularly, swirl in jets can induce sections of reverse flow in the axial direction called vortex breakdown (Liang and Maxworthy, 2005). These recirculation regions significantly alter the structure of the jet. They can also enforce axisymmetry, which is useful for

modeling (Herrada et al., 2009; Rojas et al., 2008). In simulations, the jet swirl is enforced through assumed boundary conditions at the jet exit (Buntine and Saffman, 1995; Herrada et al., 2003; Shuja et al., 2003; Herrada et al., 2009)

Chapter 3

DERIVATION OF FANS

This chapter provides a detailed derivation of the FANS equations for both continuous and discrete data. It also outlines the basic steps of calculating the terms in order to analyse flow data using FANS.

3.1 Continuous domain

The derivation begins by considering the incompressible Navier-Stokes equations of a Newtonian fluid:

$$\frac{\partial \mathbf{u}}{\partial t} + \mathbf{u} \cdot \nabla \mathbf{u} = -\nabla p + \frac{1}{Re} \nabla^2 \mathbf{u}, \tag{3.1}$$

where $\mathbf{u}$ is the instantaneous velocity vector field and p is the pressure field. These quantities are non-dimensionalized with length scale h and velocity scale U_∞, such that the Reynolds number is $Re = U_\infty h/\nu$, where ν is the kinematic viscosity. The flow is incompressible, so the continuity equation has the form:

$$\nabla \cdot \mathbf{u} = 0. \tag{3.2}$$

For the purposes of this method, the velocity and pressure fields are assumed to be representable as a Fourier series in time with period $1/f$:

$$\mathbf{u} = \sum_{k=-\infty}^{\infty} \hat{\mathbf{u}}_k e^{j2\pi kft} \tag{3.3}$$

and

$$p = \sum_{k=-\infty}^{\infty} \hat{p}_k e^{j2\pi kft}. \tag{3.4}$$

The coefficients in the infinite series ($\hat{\mathbf{u}}$ and $\hat{p}$) are complex-valued spatial functions that will henceforth be referred to as the velocity and pressure modes, respectively. The time-dependent part of the Fourier series is referred to as the dynamics. Substituting the Fourier series representation of the flow fields within the Navier-Stokes equations returns the following:

$$\frac{\partial}{\partial t}\sum_k \hat{\mathbf{u}}_k e^{j2\pi kft} + \sum_k \hat{\mathbf{u}}_k e^{j2\pi kft} \cdot \nabla \sum_k \hat{\mathbf{u}}_k e^{j2\pi kft} = -\nabla \sum_k \hat{p}_k e^{j2\pi kft} + \frac{1}{Re}\nabla^2 \sum_k \hat{\mathbf{u}}_k e^{j2\pi kft}. \tag{3.5}$$

This representation allows us to isolate momentum equations for the individual modes ($\hat{\mathbf{u}}_k$, $\hat{p}_k$) using the well-known orthogonality property of the dynamics under the inner product $\langle u, v\rangle = f\int_0^{1/f} uv \, \mathrm{d}t$:

$$f\int_0^{1/f} e^{j2\pi fkt} e^{j2\pi flt} \, \mathrm{d}t = \begin{cases} 1, & k = -l \\ 0, & \text{otherwise} \end{cases}, \quad k, l \in \mathbb{Z}. \tag{3.6}$$

This is useful if both sides of Equation 3.5 are multiplied with the test function $fe^{-j2\pi lft}$ and integrate over the interval $T = [0, 1/f]$:

$$f\int_T e^{-j2\pi lft} \left(\underbrace{\frac{\partial}{\partial t}\sum \hat{\mathbf{u}}_k e^{j2\pi kft}}_{\text{Unsteady term}} + \underbrace{\sum \hat{\mathbf{u}}_k e^{j2\pi kft} \cdot \nabla \sum \hat{\mathbf{u}}_k e^{j2\pi kft}}_{\text{convection term}} \right) \mathrm{d}t$$

$$= f \int_T e^{-j2\pi lft} \left(\underbrace{-\nabla \sum \hat{p}_k e^{j2\pi kft}}_{\text{pressure term}} + \underbrace{\frac{1}{Re} \nabla^2 \sum \hat{\mathbf{u}}_k e^{j2\pi kft}}_{\text{diffusion term}} \right) \, \mathrm{d}t. \tag{3.7}$$

The application of this integral will be considered term by term.

3.1.1 Pressure and Diffusion terms

The right hand side of equation 3.7 can be manipulated by commuting the integral and spatial derivative operators with the summations:

$$\begin{aligned} & f \int_T e^{-j2\pi lft} \left(-\nabla \sum \hat{p}_k e^{j2\pi kft} + \frac{1}{Re} \nabla^2 \sum \hat{\mathbf{u}}_k e^{j2\pi kft} \right) \, \mathrm{d}t \\ = & -\sum_k f \int_T e^{-j2\pi lft} e^{j2\pi kft} \nabla \hat{p}_k \, \mathrm{d}t + \frac{1}{Re} \sum_k f \int_T e^{j2\pi lft} e^{j2\pi kft} \nabla^2 \hat{\mathbf{u}}_k \, \mathrm{d}t \\ = & -\sum_k \left(f \int_T e^{-j2\pi lft} e^{j2\pi kft} \, \mathrm{d}t \right) \left(\nabla \hat{p}_k + \frac{1}{Re} \nabla^2 \hat{\mathbf{u}}_k \right). \end{aligned}$$

The integral in the final line is notably the inner product in Equation 3.6. Thus, it is only nonzero when $l = k$. As a result, the summation terms have a value of $\nabla \hat{p}_l + 1/Re \nabla^2 \hat{\mathbf{u}}_l$ for $l = -k$ and 0 otherwise. Thus, the right hand side of Equation 3.7 becomes:

$$f \int_T e^{-j2\pi lft} \left(-\nabla \sum \hat{p}_k e^{j2\pi kft} + \frac{1}{Re} \nabla^2 \sum \hat{\mathbf{u}}_k e^{j2\pi kft} \right) \, \mathrm{d}t = \frac{1}{f} \left(\nabla \hat{p}_l + \frac{1}{Re} \nabla^2 \hat{\mathbf{u}}_l \right). \tag{3.8}$$

3.1.2 Unsteady term

The unsteady term of Equation 3.7 can be written as:

$$f \int_T e^{-j2\pi lft} \frac{\partial}{\partial t} \sum \hat{\mathbf{u}}_k e^{j2\pi kft} \, \mathrm{d}t = f \int_T e^{j2\pi lft} \sum \hat{\mathbf{u}}_k \frac{\partial}{\partial t} \left(e^{j2\pi kft} \right) + \frac{\partial}{\partial t} \left(\hat{\mathbf{u}}_k \right) e^{j2\pi kft} \, \mathrm{d}t.$$

The $\frac{\partial}{\partial t}(\hat{\mathbf{u}}_k)$ term vanishes since the Fourier modes are functions of space only. Thus, the inner product can be written:

$$= f \int_T e^{-j2\pi lft} \sum \hat{\mathbf{u}}_k \left(j2\pi kf\right) e^{j2\pi kft} \, \mathrm{d}t.$$

This once again isolates $\hat{\mathbf{u}}_l$ due to the inner product property (Equation 3.6). As a result:

$$f \int_T e^{-j2\pi lft} \frac{\partial}{\partial t} \sum \hat{\mathbf{u}}_k e^{j2\pi kft} \, \mathrm{d}t = j2\pi lf \hat{\mathbf{u}}_l \tag{3.9}$$

3.1.3 Convection term

The nonlinearity of the convection term makes its treatment more complicated. With the inner product from Equation 3.7, the convection term is

$$f \int_T e^{-j2\pi lft} \sum_k \hat{\mathbf{u}}_k e^{j2\pi kft} \cdot \nabla \sum_i \hat{\mathbf{u}}_i e^{j2\pi ift} \, \mathrm{d}t \tag{3.10}$$

$$= f \int_T \sum_k \sum_i e^{-j2\pi lft} e^{j2\pi ift} e^{j2\pi kft} \left(\hat{\mathbf{u}}_k \cdot \nabla \hat{\mathbf{u}}_i\right) \, \mathrm{d}t \tag{3.11}$$

$$= \sum_k \sum_i f \int_T e^{-j2\pi lft} e^{j2\pi (i+k)ft} \, \mathrm{d}t \left(\hat{\mathbf{u}}_k \cdot \nabla \hat{\mathbf{u}}_i\right). \tag{3.12}$$

Here, the integral is nonzero only when $l = i+k$ (Equation 3.6). This reduces the double summation $\sum_k \sum_i$ to a single summation $\sum_i$ with the change of index $k = l - i$. As a result,

$$\int_T e^{-j2\pi lft} \sum_k \hat{\mathbf{u}}_k e^{j2\pi kft} \cdot \nabla \sum_i \hat{\mathbf{u}}_i e^{j2\pi ift} \, \mathrm{d}t = \sum_i \hat{\mathbf{u}}_{l-i} \cdot \nabla \hat{\mathbf{u}}_i. \tag{3.13}$$

Isolating the terms involving mode l and the mean flow in this summation connects the FANS equations to the linearized Navier-Stokes equations. This isolates the effect of inter-frequency

coupling on the mechanics. Thus,

$$\sum_i \hat{\mathbf{u}}_{l-i} \cdot \nabla \hat{\mathbf{u}}_i = \hat{\mathbf{u}}_l \cdot \nabla \mathbf{U} + \mathbf{U} \cdot \nabla \hat{\mathbf{u}}_l + \sum_{i \neq 0,l} \hat{\mathbf{u}}_{l-i} \cdot \nabla \hat{\mathbf{u}}_i, \tag{3.14}$$

where $\mathbf{U}$ is the mean velocity. The three terms can be interpreted as follows: $\hat{\mathbf{u}}_l \cdot \nabla \mathbf{U}$ and $\mathbf{U} \cdot \nabla \hat{\mathbf{u}}_l$ represent the effect of convective transport by mode l on the mean field and vice versa. These are the terms that arise from a linearization of the Navier-Stokes equations, for instance in linear stability analysis (Kirchgassner, 1975). Meanwhile, the final term $\left(\sum_{i \neq 0,l} \hat{\mathbf{u}}_{l-i} \cdot \nabla \hat{\mathbf{u}}_i\right)$ represents the effect on mode l of coupling between other modes. This can be viewed as a forcing term on the momentum equation for mode l. The forcing of the equation for mode l due to modes l and $i - l$ is part of the inspiration of higher-order spectral methods that look at triadic interactions, such as the Bispectral Mode Decomposition (Schmidt, 2020). These interactions will be referred to as the Fourier stresses as an analogy to the Reynolds stresses. This term can be written as

$$\tilde{\chi}[\mathbf{u}_l] = \sum_{i \neq 0,l} \hat{\mathbf{u}}_{l-i} \cdot \nabla \hat{\mathbf{u}}_i. \tag{3.15}$$

Using the results of Equations 3.8, 3.9, 3.14 and 3.15, the momentum equation corresponding to mode $\hat{\mathbf{u}}_l$ is:

$$j2\pi l f \hat{\mathbf{u}}_l + \hat{\mathbf{u}}_l \cdot \nabla \mathbf{U} + \mathbf{U} \cdot \nabla \hat{\mathbf{u}}_l + \tilde{\chi}[\hat{\mathbf{u}}_l] = -\nabla p_l + \frac{1}{Re} \nabla^2 \hat{\mathbf{u}}_l. \tag{3.16}$$

3.1.4 Continuity

Each velocity mode is divergence-free. Using the Fourier series representation in the continuity equation, it becomes:

$$\nabla \cdot \mathbf{u} = \nabla \cdot \sum_k \hat{\mathbf{u}}_k e^{j2\pi k f t} = 0. \tag{3.17}$$

To isolate an equation for mode $\hat{\mathbf{u}}_l$, an inner product of this equation is applied with the test function $e^{-j2\pi lft}$. This yields:

$$\int_T e^{-j2\pi lft} \nabla \cdot \sum_k \hat{\mathbf{u}}_k e^{j2\pi kft} \, \mathrm{d}t = \int_T \nabla \cdot \sum_k \left(\hat{\mathbf{u}}_k e^{j2\pi kft} e^{-j2\pi lft} \right) \, \mathrm{d}t$$

$$= \nabla \cdot \sum_k \int_T \hat{\mathbf{u}}_k e^{j2\pi(k-l)ft} \, \mathrm{d}t = \nabla \cdot \sum_k \int_T e^{j2\pi(k-l)ft} \, \mathrm{d}t \hat{\mathbf{u}}_k. \tag{3.18}$$

Once again the integral disappears except for $l = k$ (Equation 3.6):

$$\int_T e^{-j2\pi lft} \nabla \cdot \sum_k \hat{\mathbf{u}}_k e^{j2\pi kft} \, \mathrm{d}t = \nabla \cdot \hat{\mathbf{u}}_l. \tag{3.19}$$

Likewise, the integral of the right hand side of the continuity equation reduces to zero:

$$\int_T e^{-j2\pi lft}(0) \, \mathrm{d}t = 0. \tag{3.20}$$

Combining the two results of the inner product, we have:

$$\nabla \cdot \hat{\mathbf{u}}_l = 0. \tag{3.21}$$

This can be interpreted as a set of continuity equations that the velocity modes each satisfy independently.

3.2 Discrete Domain

The above results are only appropriate for continuous data, which is unrealistic for most flow analysis. In reality, discretely-sampled simulation or experimental data are collected for analysis. As a result, the continuous Equation 3.1 is approximated using discrete analogs:

$$\frac{\Delta \mathbf{u}_n}{\Delta t} + C[\mathbf{u}_n, \mathbf{u}_n] = -G[p_n] + \frac{1}{Re} L[\mathbf{u}_n] \tag{3.22}$$

where $\mathbf{u}_n$, p_n are the nth discrete snapshot of the velocity and pressure fields, $C[\cdot,\cdot]$ is a discrete convection operator, $G[\cdot]$ is a discrete gradient, and $L[\cdot]$ is a discrete Laplacian. For the purposes of this derivation, the particular choices of G and L are assumed to be linear. Assuming that the data consists of N evenly-spaced snapshots of the pressure and velocity fields, we will apply a Discrete Fourier Transform (DFT) to these fields:

$$\hat{\mathbf{u}}_k = \sum_{n}^{N} \mathbf{u}_i e^{j2\pi kn/N} \tag{3.23}$$

The discrete equations can be then cast into the frequency domain using the expansion coefficients $e^{j2\pi kn/N}$. Defining $f_n = n/N$, the discrete equations can be decomposed as:

$$j2\pi f_k \hat{\mathbf{u}}_k + C[\mathbf{U}, \hat{\mathbf{u}}_k] + C[\hat{\mathbf{u}}_k, \mathbf{U}] = -G[\hat{p}_k] + \frac{1}{Re} L[\hat{\mathbf{u}}_k] - \sum_{l \neq 0,k} C[\hat{\mathbf{u}}_l, \hat{\mathbf{u}}_{k-l}] \tag{3.24}$$

The closure term (Fourier stresses) will be represented as:

$$\sum_{l \neq 0,k} C[\hat{\mathbf{u}}_l, \hat{\mathbf{u}}_{k-l}] = \chi[\hat{\mathbf{u}}_k] \tag{3.25}$$

The discrete formulation has direct correspondence to the terms of the continuous formulation. These equations will be referenced in place of the continuous equations for the remainder of the thesis.

3.3 Application

The application and utility of the final momentum equations may not initially be clear. As a result, this chapter discusses the physical interpretation of the terms and discuss options for calculating them. Particularly, this is to distinguish this method from previous works involving similar equations such as the Time Spectral, Harmonic Balance, and Self-Consistent Methods discussed in Chapter 2. The above methods use the decomposed momentum equations for simulation of periodic flows.

Table 3.1: Names of FANS terms.

Terms	Continuous form	Discrete form
Unsteady	$j2\pi k f \hat{\mathbf{u}}_k$	$j2\pi f_k \hat{\mathbf{u}}_k$
Convection by mean	$\mathbf{U} \cdot \nabla \hat{\mathbf{u}}_k$	$C[\mathbf{U}, \hat{\mathbf{u}}_k]$
Convection of mean	$\hat{\mathbf{u}}_k \cdot \nabla \mathbf{U}$	$C[\hat{\mathbf{u}}_k, \mathbf{U}]$
Pressure	$\nabla \hat{p}_k$	$G[\hat{p}_k]$
Diffusion	$\frac{1}{Re}\nabla^2 \hat{\mathbf{u}}_k$	$\frac{1}{Re}L[\hat{\mathbf{u}}_k]$
Fourier stresses	$\tilde{\chi}[\hat{\mathbf{u}}_k]$	$\chi[\hat{\mathbf{u}}_k]$

In contrast, the idea here is to leverage the equations to extract additional information from flow field data obtained from any source, including unsteady simulations and experiment.

3.3.1 Interpretation of terms

Similar to the terms in the turbulent kinetic energy budget from RANS (Durbin and Pettersson, 2011), the FANS equations can be seen as a momentum budget for different Fourier modes. As such, it is natural to name and interpret each term separately. The names, as well as discrete and continuous forms of each term are shown in Table 3.1. The specific interpretation of each of these terms are outlined below:

Unsteady term The unsteady term (UT) is a scaled version of the corresponding velocity mode with a 90° phase shift. By interpreting this term as the difference of the other five, spatial distributions of each Fourier mode can be understood as the result of the contributions of the diffusive, pressure, and convective fluxes.

Mean flow convection terms The mean flow convection term represents the effects of transport by and on the mean flow by the mode $\hat{\mathbf{u}}_k$. These terms are similar to the convection terms that arise when the Navier-Stokes equations are linearized about the mean flow.

Fourier stresses The remaining parts of the convection term, which arise due to the coupling between modes, are called Fourier stresses. They are named as such to make an analogy to Reynolds stresses, which appear in the RANS equations.

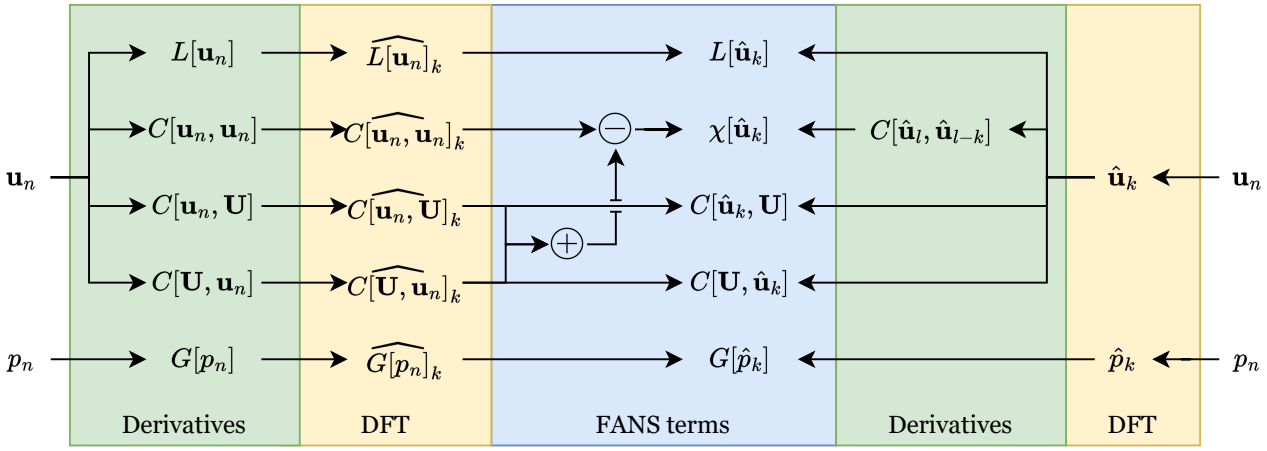

Figure 3.1: Options for calculating FANS terms

Diffusion term The diffusive fluxes at a particular timescale only affect the mode corresponding to that timescale.

Pressure term The influence of pressure fluctuations at a given frequency are isolated to the corresponding pressure modes. Pressure can be treated as an independent variable, or as another operation on the velocity field, since it can be entirely determined by the velocity field and boundary conditions in incompressible flows (Foias et al., 2001). However, the latter interpretation is less intuitive and more difficult to calculate. The pressure term requires further decomposition into mean-flow convection, Fourier stress, and boundary contributions. Thus, for the purposes of this thesis, the pressure will be treated as an additional applied force.

3.3.2 Calculation of terms

Two methods can be utilized to calculate the FANS terms from flow field data. A visualization of these processes can be seen in Figure 3.1. The first option is to calculate the Navier-Stokes terms on the original snapshots and then apply the Discrete Fourier Transform (DFT) on each set of terms. The other option is to apply the DFT to the snapshots and then calculate the FANS terms from the modes. For the unsteady, diffusion, pressure, and mean-flow convection terms, these two methods are equivalent. However, the first method allows the Fourier stresses to be

calculated quickly by calculating the derivatives in the time domain, whereas the second method requires calculating a sum of N convection terms in the frequency domain for each of the N modes. The first method is widely used in this thesis. Code for implementing this process is presented in Appendix A for OpenFOAM and Python. Meanwhile, the second method is occasionally used when the contribution of particular frequencies to the Fourier stresses is desired. Code for calculating this effect in Python is presented in Section A.8.

When the FANS equations are calculated from simulation data, it is recommended to use the same spatial discretization methods as the solver of the governing equations, when possible. For instance, if central differencing scheme was employed to calculate the convection term, then central differencing scheme should be utilized to calculate the mean flow convection and Fourier stress terms. Keeping the discretization method consistent prevents additional numerical errors. This strategy was taken in all case studies investigated as a part of this thesis.

The derivation of FANS that results in Equation 3.24 implies a single, long-time box window including all available data. As a result, the standard rules apply with regards to sampling frequency and window size. The analysis window must be sufficiently large to allow for good frequency resolution. Furthermore, utilizing the DFT in this case indicates that FANS is highly useful in cases with cyclic behaviour, either through regularly or irregularly recurring structures or processes.

Chapter 4

NUMERICAL METHODS FOR CASE STUDIES

Application of the FANS equations and the interpretation of this analysis is evaluated with several case studies. The first three case studies are used to compare the FANS terms to well-established physics in literature. These cases replicate simulations used in previous investigations. These cases are: laminar vortex shedding over a two dimensional square cylinder (Bai and Alam, 2018), impingement of a swirling axisymmetric jet onto a flat plate (Herrada et al., 2009), and the nonperiodic wake of a pair of two dimensional cylinders arranged side-by-side (Ma et al., 2017).

The next series of cases are of 3D flow over a normal flat plate at Reynolds number of 250. Several cases will be set up to analyse the effect of different end conditions on the wake and periodicity of this flow. End effects on the wake of normal flat plates are not yet fully understood (Braun et al., 2020). FANS is implemented to evaluate its utility in educing new physics in this complex wake as was discussed in Section 2.4. Simultaneously, understanding the end effects on the wake physics is valuable to the bluff body community. The computational details of each of these cases will be elaborated upon separately.

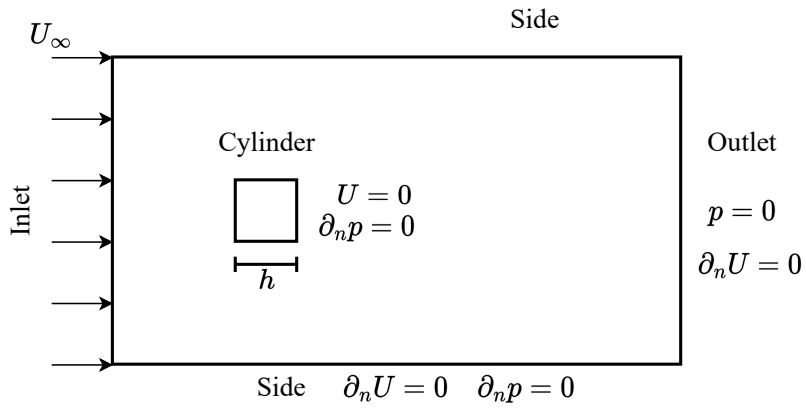

Figure 4.1: Domain setup for square cylinder at $Re = 100$.

4.1 Square cylinder

The first case study looks at the laminar flow over a square cylinder at Reynolds number of 100. This is a simple, two dimensional, and periodic flow, which constitutes a simple known problem in fluid mechanics. The simulation is set up in order to mimic the results of Bai and Alam (2018) for their two dimensional cylinder cases. The simulations are completed using the finite volume toolbox OpenFOAM (v2012). The computational domain and boundary conditions are shown in Figure 4.1. The domain extends $5h$ upstream of the cylinder, $20h$ downstream, and $8h$ in both transverse directions. Velocity boundary conditions consist of a uniform inlet condition of $U_\infty = 1$, no slip at the cylinder, and zero gradient at the sides and outlet boundaries. The pressure boundary conditions are zero gradient everywhere except at the outlet, where the pressure is set to a uniform value of $p = 0$. The OpenFOAM tool blockMesh was used to generate the mesh. 100 uniformly spaced cells are placed along each side of the cylinder, giving a minimum mesh spacing of $\delta x/h = 0.01$. The mesh spacing is smoothly inflated at a rate of 1.02 in each direction away from the cylinder. The total number of cells in the mesh is $1.4 \cdot 10^5$, which is shown in Figure 4.2, including a detailed view of the mesh around the cylinder. Second order central differencing scheme is used for all spatial discretizations. The Crank-Nicholson method with a blending factor of 0.95 is used for temporal discretization with a time step of $\delta t U_\infty/h = 0.01$ in order to hold the Courant number below 1. Pressure-velocity coupling was handled using the Pressure-implicit with Splitting of

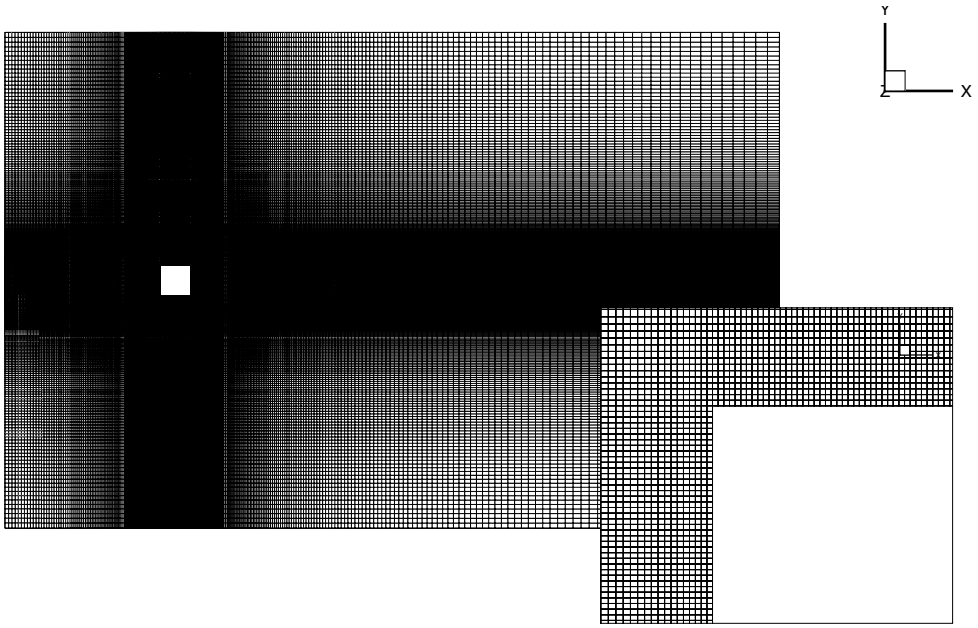

Figure 4.2: Visualization of mesh around square cylinder. Inset: Detail view of mesh at upper left corner of cylinder.

Operators (PISO) method. Two pressure correctors were used at each time step. The solution of the linear systems consisted of a Generalized Geometric-Algebraic Multi-grid (GAMG) solver with Gauss-Seidel smoothing for the pressure and velocity. The results are validated against the simulation of Bai and Alam (2018) at the same Reynolds number, which it replicates satisfactorily.

The wake at this Reynolds number consists of a single, periodic Karman vortex street that is shed from the leeward side of the cylinder. The vortices grow due to diffusion and diverge from the wake centreline as they move downstream. The interaction of these vortices in the near wake and the corresponding momentum fluxes will be analysed using the FANS formulation and analysis.

4.2 Swirling Jet

The next case involves a swirling jet impinging on a flat plate, which is incrementally more complex than the wake of a square cylinder. This case, based on Herrada et al. (2009), is selected because of its highly modulated but periodic time signature. The jet is axisymmetric, and has contributions from all three velocity components due to the swirl. OpenFOAM is used for this simulation.

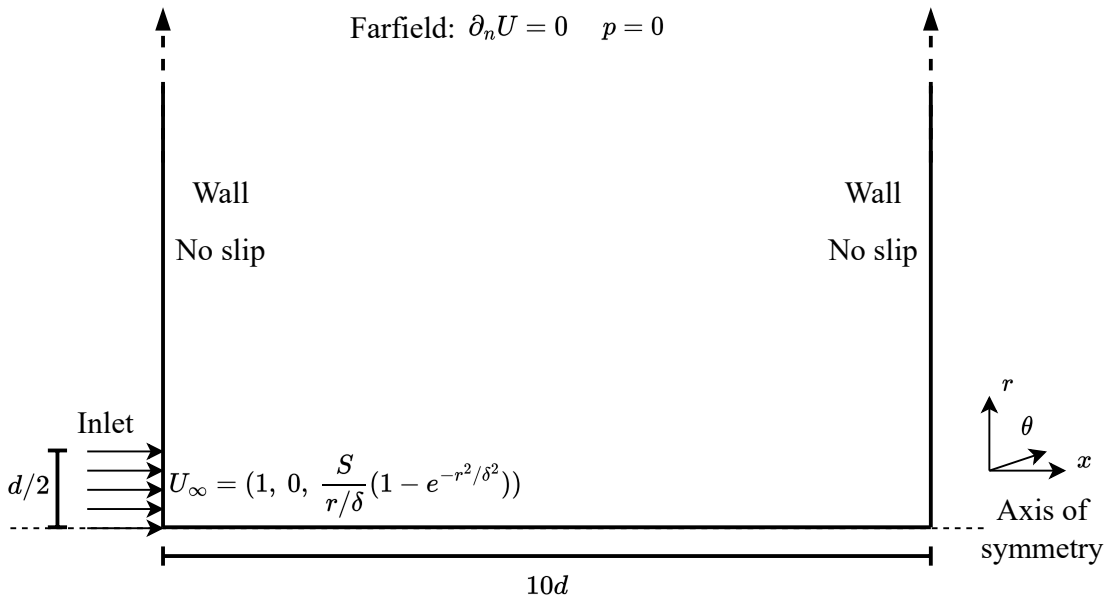

Figure 4.3: Domain setup for swirling jet at a Reynolds number of 204. The jet swirl parameter is $S = 0.3$ and the vortex core diameter is $\delta = 0.25$.

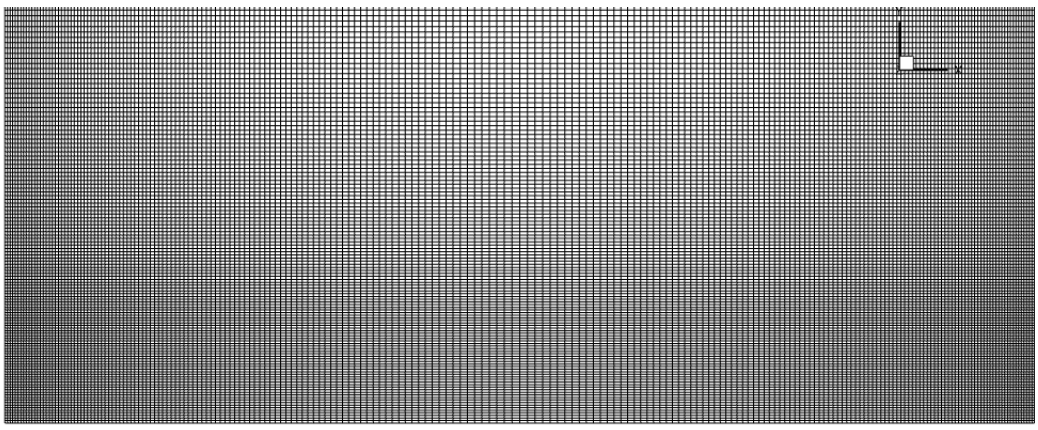

Figure 4.4: Mesh of the swirling jet case. Upper section of the domain is cut off; cells inflate uniformly towards the outlet.

The basic domain is shown in Figure 4.3. The domain consists of a jet with uniform axial velocity flowing from an inlet diameter d and Reynolds number ($Re = Ud/\nu$) of 204. A Burgers vortex is imposed on the jet to represent the swirl. The vortex is characterized by two nondimensional parameters, the swirl parameter S and a vortex core radius δ. This jet is implemented as a velocity boundary condition with a zero-gradient pressure condition. Outside the inlet, the left wall is assigned the no-slip condition. The jet impinges upon a no-slip wall (plate) placed $10d$ from the inlet. The axisymmetric domain has a total radius of $30d$ following Herrada et al. (2009) to ensure domain size independence, and the farfield is implemented as a zero-gradient velocity condition with uniform $p = 0$. The mesh is created using the blockMesh and extrudeMesh tools in OpenFOAM. A wedge domain with a swept angle of 1° is used for the axisymmetric flow simulation using Cartesian coordinates. 220 cells are placed along the axial direction with additional refinement at the inlet and wall boundaries. Cell spacing in axial direction inflates at a uniform rate of 1.01 away from the boundaries. The inlet is meshed with 60 uniformly spaced cells in the radial direction, and the remainder of the wall is meshed with 322 cells in the radial direction that inflate uniformly at a rate of 1.01. The total number of cells is $7.96 \cdot 10^4$. A view of the lower section of the mesh is shown in Figure 4.4. Second order central differencing scheme is used for spatial discretization of the governing equations. A second-order backward scheme is used for time discretization with a uniform time step of $\Delta tU/d = 0.002$, which ensures that the Courant number remains around 0.8. The PISO algorithm with two pressure correctors is used for pressure-velocity coupling. The linear systems for pressure and velocity are solved using GAMG and Preconditioned Bi-conjugate Gradient (PBiCG) solvers, respectively. A Diagonal-based Incomplete Lower-Upper (DILU) preconditioner is used for the velocity system.

The swirl parameter S and core radius δ are 0.3 and 0.25, respectively. This results in a complicated but periodic jet discussed in Herrada et al. (2009). The simulation was validated in terms of the minimum value of the axial velocity U over time, which was reported by Herrada et al. (2009) (Figure 4.5). The present simulation closely tracks their time history. The error in the period is 1%, and the mean squared error is 2% of the minimum velocity range. Herrada et al.

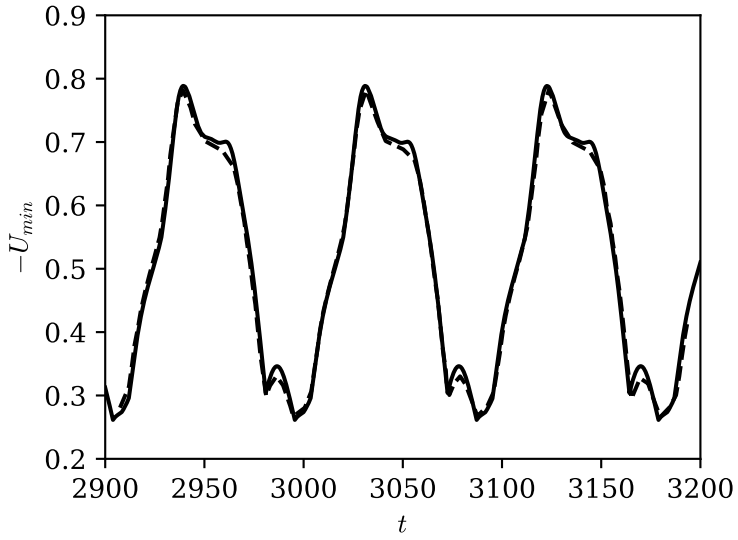

Figure 4.5: Time history of minimum streamwise velocity in the domain for verification against Herrada et al. (2009). Solid line: present study. Dashed line: Herrada et al. (2009).

(2009) noted that the jet is characterized by a large recirculating region along the central axis, called a “vortex breakdown (VB) bubble", as well as several axisymmetric vortex bubbles that originate and decay close to the wall over multiple intervals each cycle. The circulation convects outward due to radial flow from the jet impingement. The periodic origin and decay of transient vortex bubbles results in a highly modulated time signature. Consequently, the spectrum of the flow is composed of large energy concentrations at several distinct frequencies with a base frequency of $f^* = fd/U \approx 0.011$.

4.3 Side by Side cylinders

The next case study to illustrate the application and strength of FANs involves the wake of two side-by-side cylinders. This case is selected as a further increase in complexity over the first two cases. The additional complexity comes from irregularity in the vortex shedding. Instead, there are several dominant frequencies in a broadband spectrum. This complicated time signature arises from two shedding processes - shedding from the individual cylinders and a Karman wake that develops several cylinder lengths downstream. At any particular moment, the wake is asymmetric

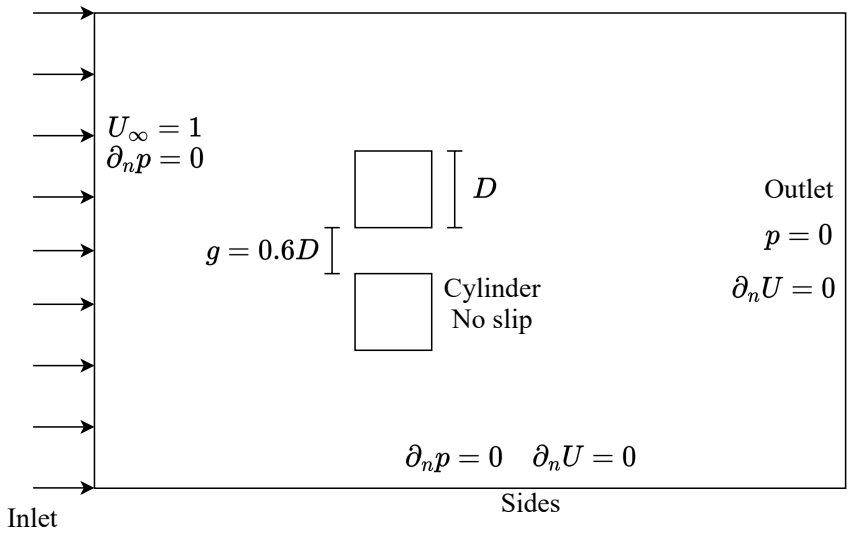

Figure 4.6: Domain setup of side-by-side cylinders with a gap ratio of 0.6 at a Reynolds number of 90. Figure not to scale.

and the shedding is stronger from one of the two cylinders. However, this asymmetry switches over time in a process known as “flip-flopping" (Burattini and Agrawal, 2013; Carini et al., 2014). The shedding and flip-flopping processes repeat irregularly over time (Ma et al., 2017).

The simulation is set up with a domain represented in Figure 4.6. The Reynolds number based on the cylinder diameter is $Re = U_\infty D/\nu = 90$. The gap between the cylinders is $g = 0.6D$. This results in an irregular, nonperiodic wake that was described by Ma et al. (2017). The mesh setup and domain are constructed to mimic the simulations of Ma et al. (2017), which assume the flow to be 2D. The domain extends $10D$ ahead, $40D$ behind, and $15D$ above and below the cylinder centrepoints to ensure domain independence. The boundary conditions consist of no-slip walls at the cylinders and slip conditions at the sides. The inlet has uniform velocity $U_\infty = 1$ and zero pressure gradient. The outlet has a uniform outlet pressure of 0 and zero velocity gradient.

There are 25 cells arranged uniformly around each side of the cylinders. The mesh spacing is finer normal to the cylinders to adequately resolve the boundary layers, with the smallest mesh spacing as $0.01D$. The mesh expansion rate is maintained below 1.02 in the domain. 55 cells are placed in the gap with a hyperbolic mesh law, with a minimum spacing of $0.01D$. There were a

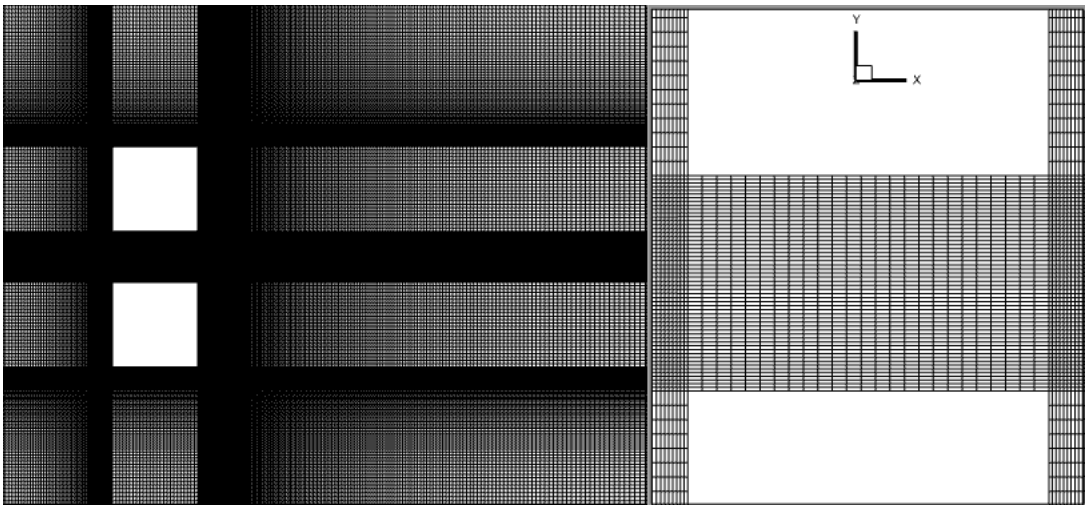

Figure 4.7: Mesh for dual cylinder case. Left: View of mesh around cylinders and in wake, Right: detail view of mesh in between cylinders.

Table 4.1: Mean drag and lift coefficients for pair of side-by-side cylinders at $Re = 90$, $g/D = 0.6$, compared to Ma et al. (2017).

Property	**Ma et al. (2017)**	**Lower cylinder**	**Upper cylinder**
C_d	1.93	1.90	1.88
C_l	0.71	-0.71	0.69

total of 515 cells in the streamwise and 474 cells in the transverse direction, for a total of $2.4 \cdot 10^5$ cells. The mesh is shown in Figure 4.7.

Simulations were completed in OpenFOAM using the PIMPLE (combined PISO-SIMPLE) algorithm for pressure-velocity coupling. Two outer (nonlinear) iterations each with three pressure corrections were used. The time step was $0.002\Delta tU/D$ to maintain the Courant number under 0.4. Second order central differencing scheme was used for spatial discretization and a second-order backward solver was used for the temporal discretization of the governing equation. GAMG was used as the solver for the pressure system and PBiCG with a DILU preconditioner was used for the velocity system. The time histories of drag and lift coefficients closely match with the results of Ma et al. (2017). Mean properties of each are shown in Table 4.1. The simulation was run for an interval over $2500D/U$ to ensure that there was sufficient data for FANS and BMD analysis, corresponding to roughly 400 shedding cycles and over 25 flip-flop processes.

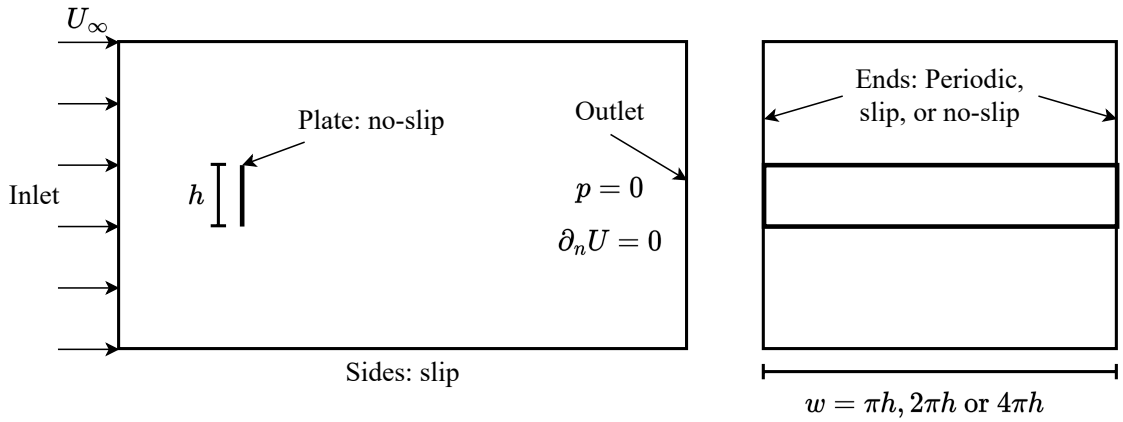

Figure 4.8: General geometry and boundary conditions of flat plate cases. Not to scale.

4.4 Flat plate

The final set of cases considered in this thesis consist of three-dimensional flow over a flat plate at a Reynolds number of 250. The purpose of this study is to consider the effect of the plate end condition on the mean and fluctuating characteristics. As a result, several cases will be considered, keeping fixed Reynolds number, with altered length and boundary conditions at the ends (spanwise edges). Normal flat plates exhibit complicated physics due to their intrinsically 3D wake (Najjar, 1994; Hemmati et al., 2018). The wake is also highly sensitive to extrinsic 3D effects due to the spanwise end conditions (Lisoski, 1993; Hemmati et al., 2016b; Braun et al., 2020). In experiments, extrinsic effects are usually eliminated through the use of long plates (Lisoski, 1993; Williamson, 1996; Braun et al., 2020), while simulations employ periodic boundary conditions (Najjar, 1994; Balachandar et al., 1997; Hemmati et al., 2018; Singh and Narasimhamurthy, 2022). However, Braun et al. (2020) recently reported a pair of flat plate wakes that were highly affected by spanwise end conditions despite a large aspect ratio. When angled end plates were used, it was shown to strongly affect the fluctuating and mean characteristics of the wake, even at the midspan. As a result, this work will also consider a simulation study of differing end-plate conditions on the fluctuating characteristics of the flow using the decomposed momentum equations.

A general domain for these cases is shown in Figure 4.8. The control volume consists of a plate that runs along the entire length of the z (spanwise) direction. The plate is oriented normal to the

Boundary	Velocity condition	Pressure condition
Inlet	Uniform $(U_\infty, 0, 0)$	Zero gradient
Outlet	Zero gradient	Uniform $p = 0$
Sides	Zero gradient	Zero gradient
Ends	Case-specific	

Table 4.2: Common boundary conditions for flat plate cases.

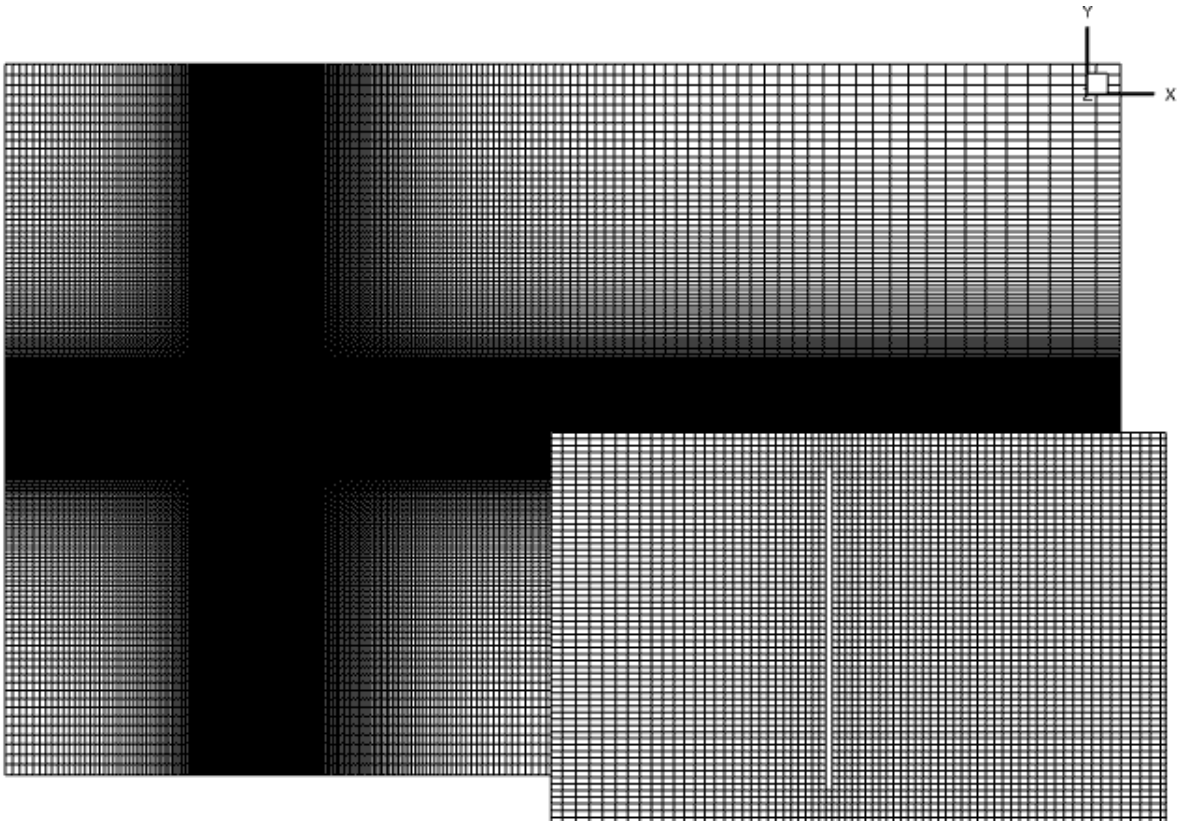

Figure 4.9: Mesh of flat plate case. Left: View of whole domain in $x - y$ plane. Inset: Detail view of mesh around plate in $x - y$ plane. Right: Uniform spanwise meshing for Case 1 and 2 seen in $z - y$ plane.

freestream. There is a distance of $5h$ ahead of the plate and $20h$ behind it. The domain extends $8h$ above and below the plate to reduce blockage effects. These dimensions are commonly used in similar simulation studies (e.g. Najjar and Vanka, 1995b; Afgan et al., 2013; Hemmati et al., 2018). The spanwise width of the domain is varied case-by-case, as will be described later. The common boundary conditions are detailed in Table 4.2. The minimum mesh spacing at the plate is $0.02h$ and the expansion rate is held under 1.03 in all directions. A reduced expansion rate of 1.01 at the plate assists in resolving the recirculation region. Details of the mesh are visualized in Figure 4.9.

Table 4.3: Flat plate cases considered in current study.

	Width	**End condition**	**Name**	**Cells in spanwise direction**	**Total cells**
Case 1	$2\pi h$	Periodic	Base	96	$5.6 \cdot 10^6$
Case 2	$2\pi h$	Slip	Slip	96	$5.6 \cdot 10^6$
Case 3	$2\pi h$	No-slip	No-slip	140	$8.2 \cdot 10^6$
Case 4	$4\pi h$	No-slip	Double	234	$13.1 \cdot 10^6$

OpenFOAM was used to complete the simulations. In all cases, the time step was $0.003h/U_\infty$ which ensured that the Courant number remains less than 0.4. Second-order backward differencing scheme was used for temporal and central differencing scheme used for spatial discretization of the governing equations. The PISO method was used for pressure-velocity coupling. GAMG was used for the pressure solver and PBICG preconditioned with the DILU method was used for the velocity solver.

The spanwise width and end boundary conditions are varied in order to analyse their effect on the flow. The cases are selected to compare a number of these conditions. Differences in the cases are detailed in Table 4.3. The base case is Case 1, which has a width of $2\pi h$ and periodic end conditions. This is a common setup for "nominally 2D" plate simulation studies (Najjar and Vanka, 1995b; Narasimhamurthy and Andersson, 2009; Afgan et al., 2013; Hemmati et al., 2018; Singh and Narasimhamurthy, 2022). Widths around $6h$ are selected based on the initial studies of Najjar (1994), who indicated that it is several times larger than the primary spanwise structures. This has been confirmed at $Re = 250$ by domain independence studies by Singh and Narasimhamurthy (2018, 2021). 96 uniformly spaced cells were used to cover the spanwise direction.

Case 2 consists of the same geometry and mesh as Case 1, but with the end conditions changed to slip walls. There is no need to modify the mesh for this case as no boundary layer develops at the wall. However, the slip condition differs from the periodic boundary as it does not allow flow or spanwise variation through the wall.

Since Case 2 does not include a boundary layer, a no-slip condition is also investigated in Case 3. The mesh in the spanwise direction is modified to adequately resolve the boundary layer, as shown in Figure 4.10. A minimum cell size at the wall of $0.02h$ is used to ensure $y^+ < 0.5$ almost

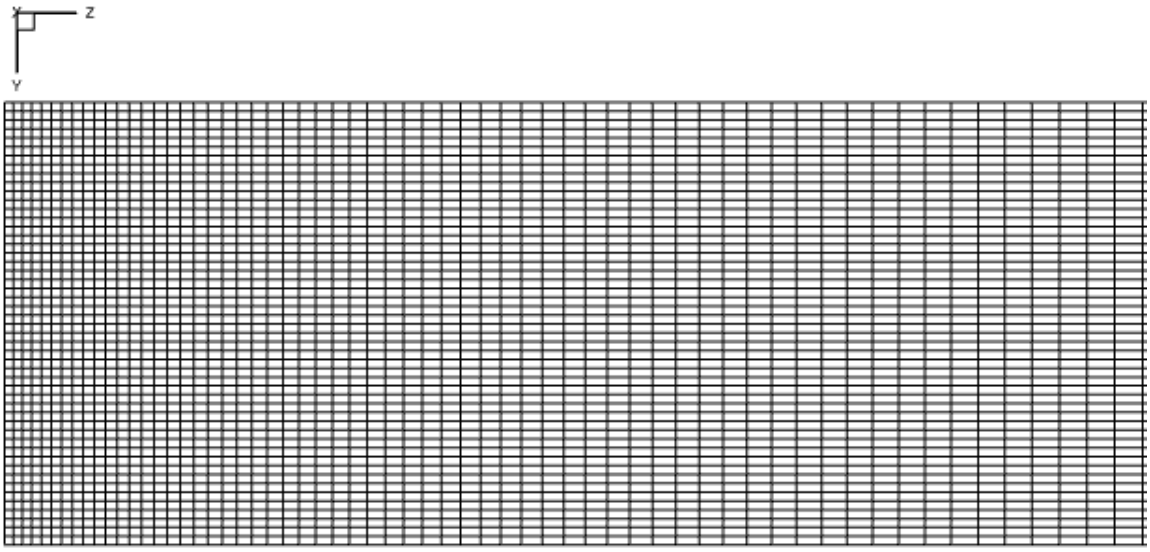

Figure 4.10: Mesh on one half of the plate in $z - y$ plane for no slip case (Case 3). The same spanwise mesh laws are applied throughout the domain.

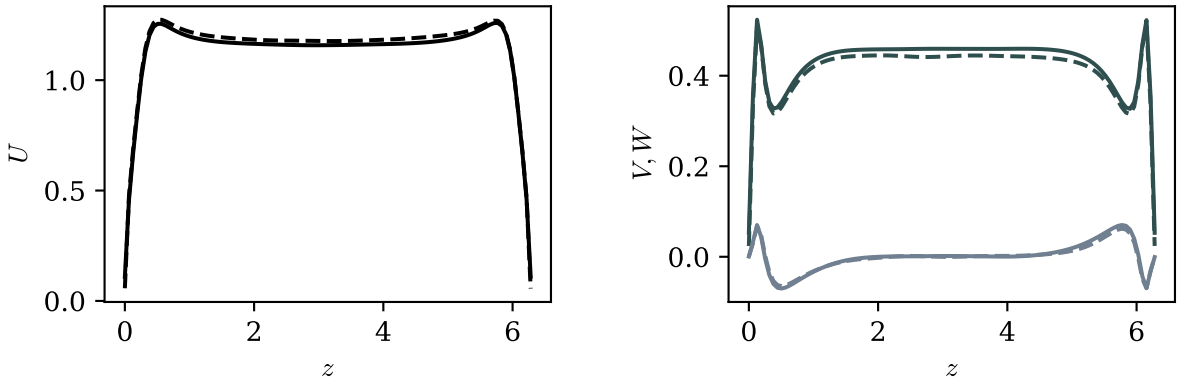

(a) (b)

Figure 4.11: Mean velocity profiles at $x = 0$, $y = 1$ for minimum wall spacings of $\Delta z = 0.02$ (solid lines) and $\Delta z = 0.01$ (dashed lines). (a) Streamwise velocity, (b) transverse velocity (dark grey) and spanwise velocity(light grey).

everywhere[1]. This minimum size was confirmed to be adequate by a test case where the boundary cell size was reduced to $0.01h$, which only minimally affected the results as shown in Figure 4.11. The maximum cell spacing in the spanwise direction is the same as in Cases 1 and 2 $(2\pi/96h)$. The spanwise geometry is effectively a channel with height $H = 2\pi h$, and the corresponding Reynolds number based on height of $Re_H = 1571$. This is above the transition Reynolds number for spot

[1]There are limited regions near the plate where $y^+ > 1$ due to deflection of the flow toward the wall.

Table 4.4: Comparison of properties of plate with periodic end conditions (Case 1) at $Re = 250$ with Singh and Narasimhamurthy (2022).

Source	$\overline{C_d}$	St	L_w
Present	2.29	1.65	$2.06h$
Singh and Narasimhamurthy (2022)	2.22	1.64	$2.04h$

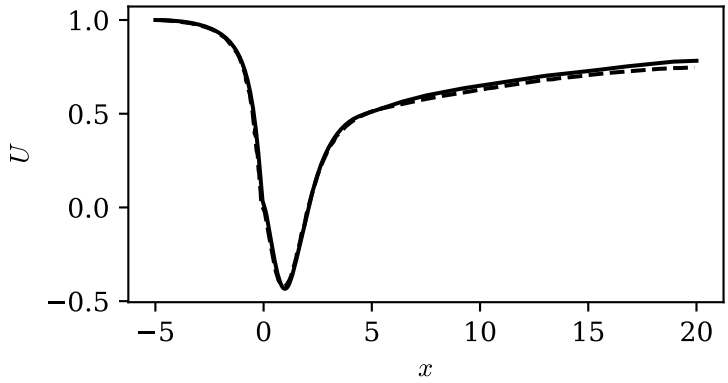

Figure 4.12: Mean streamwise velocity along plate centreline of flat plate with periodic end conditions compared to Singh and Narasimhamurthy (2022). Solid line: present, Dashed line: Singh and Narasimhamurthy (2022).

turbulence in a channel, but below the linear stability threshold (Carlson et al., 1982). However, turbulent spots are not expected to appear as the domain is shorter than the development length, which is roughly $120H$ at this Reynolds number (Sadri, 1999)[2]. As a result, the boundary layer is assumed laminar.

Case 1 is used as a validation case against the results of Singh and Narasimhamurthy (2022). The mean drag coefficient (C_d), Strouhal number (St) and recirculation length (L_w) are shown in Table 4.4. Additionally, the mean streamwise velocity is compared between the two cases in Figure 4.12. All measured properties closely match the published results of Singh and Narasimhamurthy (2022).

[2]Figure 10.11, based on most conservative criteria (vii) - incremental pressure loss at 95% of final value.

Chapter 5

CASE STUDIES

In this chapter, three of the four case studies that were established in Chapter 4 are presented. The purpose of these case studies is to establish the use of FANS on flow data, and to compare its conclusions to known physics. In this way, the purpose of these cases is to validate the method, in line with the second and third objectives detailed in Section 1.2. Section 5.1 is on the analysis of the wake of a square cylinder. This is followed by Section 5.2 on a swirling jet, and the chapter closes with analysis of the wake of two cylinders arranged side-by-side in Section 5.3.

5.1 Square cylinder

We begin with the simple case of flow over a 2D square cylinder at Reynolds number of 100. The numerical details of this simulation are described in Section 4.1. The flow is periodic, exhibiting a dominant frequency and harmonics. This makes this a natural starting point for illustrating FANS-based analysis.

The wake behind the cylinder is characterized as a classic periodic (Karman) vortex shedding process, described by Williamson (1996). These vortices grow due to diffusion and diverge from the centreline as they are convected downstream. This shedding results in a velocity spectrum characterized by distinct peaks that diminish rapidly in magnitude as the mode number increases, as seen in figure 5.1. As a result, only the mean and modes at the fundamental frequency and

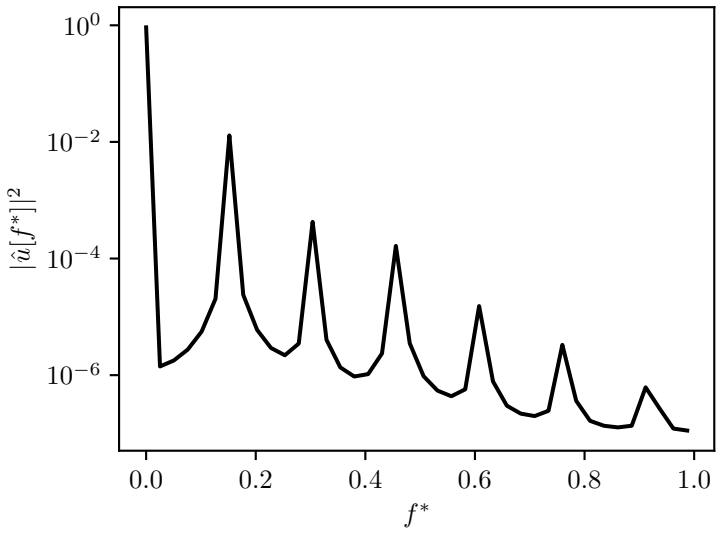

Figure 5.1: Velocity spectrum in the wake of a square cylinder at a $Re = 100$. The fundamental frequency is $f^* = 0.15$.

second harmonic are considered. These modes have a maximum magnitude of $1.3U_\infty$, $0.3U_\infty$, and $0.07U_\infty$, respectively. Here, FANS is used to explore the momentum transportation associated with the vortex street as well as the interactions between newly-formed vortices immediately behind the cylinder.

Figure 5.2 shows the real values of FANS terms at the fundamental frequency ($f^* = fh/U_\infty = 0.15$) for the streamwise velocity, $\hat{u}^1$. The data are represented as a fraction of the maximum of the UT in the domain at the same frequency and direction, T^1_{max}:

$$T^k_{max} = \max_{\vec{x}}(|j2\pi f k\hat{u}^k(\vec{x})|). \tag{5.1}$$

For example, the value displayed in figure 5.2(a) is $j2\pi f^* k\hat{u}^1/T^1_{max}$. By applying this same normalization to each flux at a given frequency, the relative contribution of each term can be compared. Figure 5.2(a) shows UT ($j2\pi f^*\hat{u}^1$) of the fundamental frequency in the streamwise direction. Contours of the UT are associated with the large-scale fluctuations of the vortices. Figure 5.2(b) shows the mean flow convection term $C[\mathbf{U}, \hat{u}^1] + C[\hat{\mathbf{u}}^1, U]$. Figure 5.2(c) shows the pressure term and figure 5.2(d) shows the Fourier stresses. The viscous dissipation is of negligible

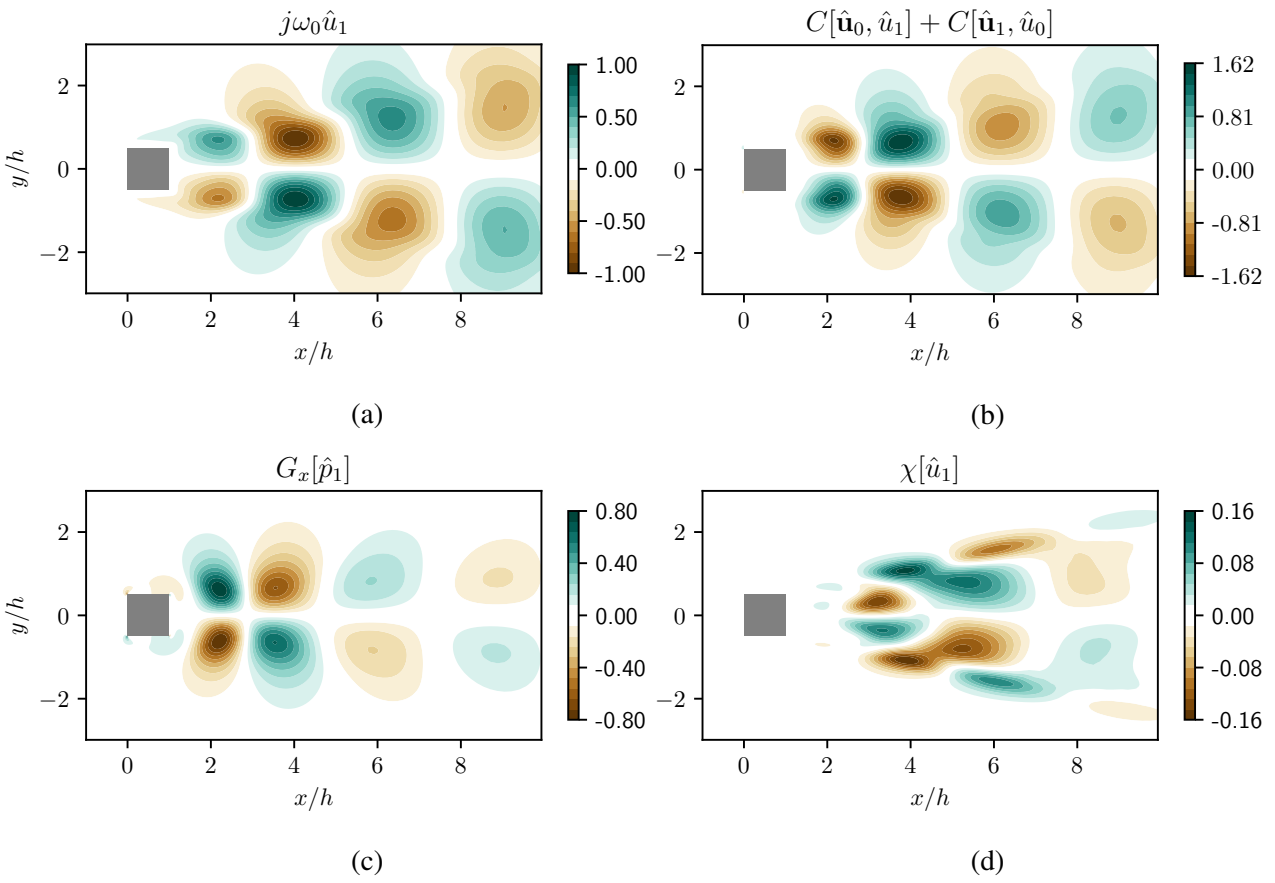

Figure 5.2: Streamwise momentum terms for mode 1 (at the fundamental frequency) in the wake of a square cylinder at $Re = 100$: (a) UT (b) mean-flow convection (c) pressure gradient and (d) Fourier stress terms.

magnitude and it is not shown here for brevity. Downstream of the cylinder (past $x = 8h$), the only force with significant magnitude is the mean-flow convection. This represents the region where fully-formed vortices are convected downstream. In FANS terms, the mean-flow convection is nearly balanced by the UT.

Immediately behind the cylinder, there are pressure gradients of large magnitude, which are related to the vortex formation. This is contrary to the downstream wake region. This way of comparing the magnitude of momentum terms identifies the critical forces by region. The pressure gradient in this region is in-phase with the UT and out-of-phase with the mean-flow convection. From this phase relationship, the pressure gradient reduces the overall fluctuation magnitude of the velocity field caused by movement of the vortices.

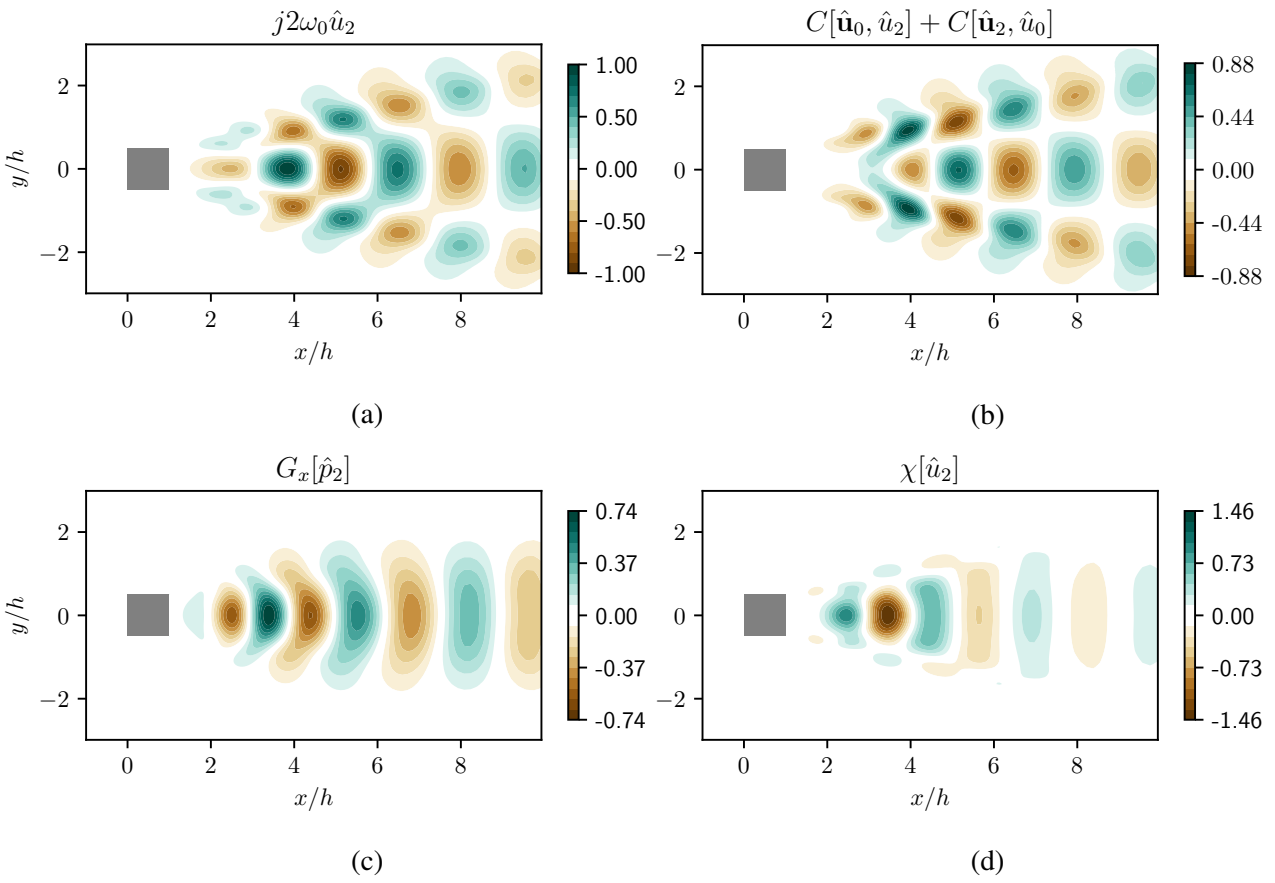

Figure 5.3: Real part of streamwise (a) unsteady (b) mean-flow convection (c) pressure gradient and (d) Fourier stress terms for the second harmonic of vortex shedding over a square cylinder at $Re = 100$.

The low magnitude of the Fourier stress term indicates that the inter-frequency interactions do not have a significant effect on the mode at the fundamental frequency. This is consistent with the findings of other methods, such as linear stability or the Self Consistent Method (Meliga et al., 2016). These stresses are generated by interaction of modes $\hat{u}_1$ and $\hat{u}_2$ in the form $\hat{\mathbf{u}}_{-1} \cdot \nabla \hat{u}_2$. The significantly reduced magnitude of the harmonic (mode 2) with respect to mode 1 results in the low magnitude of these stresses. A representation of mode 2 is shown in figure 5.3(a) in the form of the UT. The magnitude of the harmonic is elevated at the centreline and in two branches diverging from the centreline, which correspond to the edges of each vortex track.

The other momentum components in the streamwise direction for the second harmonic are also shown in figure 5.3(b), (c), and (d). The relationships between different momentum fluxes are the

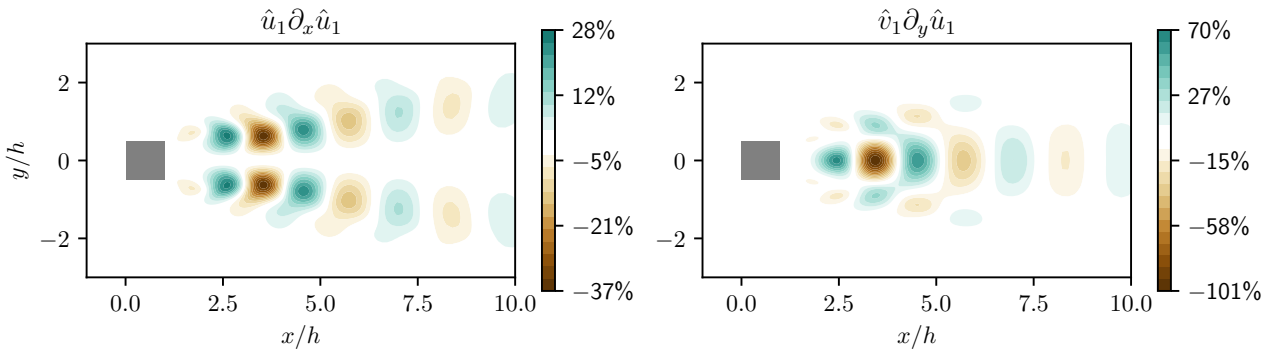

(a) (b)

Figure 5.4: Constituent terms of the Fourier stresses ($\chi[\hat{u}^2]$) in the streamwise direction at the second harmonic for a square cylinder at $Re = 100$. (a) first term (b) second term. Only the real parts of the stresses are shown.

same as they are in the fundamental frequency. Away from the axis and farther downstream in the wake, the unsteady and convection terms are nearly balanced. Behind the cylinder, the pressure term is significant and in-phase with the velocity fluctuations.

The Fourier stresses play a more critical role in affecting the balance at the harmonic compared to the fundamental frequency modes. The convective interactions represented by this term are significant to the momentum transport at this frequency. This momentum flux is strong and symmetric about the wake centreline, and dissipates rapidly moving downstream. To better understand this momentum flux, the constituent terms of the Fourier stresses are analysed. These terms arise from the expansion of $\chi[\hat{u}^2]$:

$$\chi[\hat{u}^2] = ... + \hat{u}^{-1}\partial_x\hat{u}^3 + \hat{v}^{-1}\partial_y\hat{u}^3 + \hat{u}^1\partial_x\hat{u}^1 + \hat{v}^1\partial_y\hat{u}^1 + \hat{u}^3\partial_x\hat{u}^{-1} + \hat{v}^3\partial_y\hat{u}^{-1} + ... \tag{5.2}$$

For this flow, terms other than $\hat{u}^1\partial_x\hat{u}^1$ and $\hat{v}^1\partial_y\hat{u}^1$ are negligible. This is similar to the results of Mantic-Lugo et al. (2015) using self-consistent analysis of a cylinder wake. Due to their influence on the momentum flux of velocity mode 2, these terms can be interpreted as the driving force of triadic interactions between the fundamental frequency, itself, and the second harmonic. The real parts of these terms are depicted in figure 5.4. The values are normalized to the maximum Fourier stress in the domain ($\chi[\hat{u}^2]$). The first term ($\hat{u}^1\partial_x\hat{u}^1$) roughly follows the track of the vortex street.

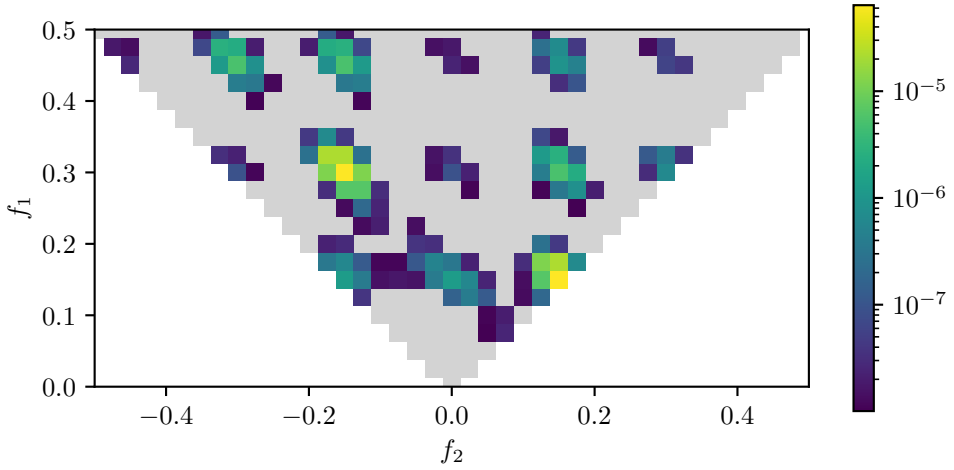

Figure 5.5: BMD mode bispectrum of square cylinder at $Re = 100$.

This flux is strongest near the vortex formation region, and then dissipates as the vortices separate and lose strength downstream. Hence, this term is a result of convective momentum transport between streamwise velocity fluctuations within an individual vortex. Peaking at roughly 40% of the magnitude of $\chi[\hat{u}^2]$, this component makes a significant contribution to the momentum flux, especially in the vortex formation region. However, the other term ($\hat{v}^1\partial_y\hat{u}^1$) in figure 5.4(b) has a more significant effect. This term attains 100% of the maximum Fourier stress in the vortex formation region. Thus, this is the primary term of the Fourier stresses at the second harmonic of the streamwise velocity. The presence of this momentum transport at the vortex formation region indicates that the second harmonic is a product of interactions between pairs of counter-rotating vortices formed off of the top and bottom surfaces of the cylinder. Interactions between these vortices will occur every half-cycle, hence the appearance of this process in the momentum equation at the second harmonic. This shows how interactions at the fundamental frequency result in increased energy content of the second mode.

FANS analysis can directly deduce interactions between timescales, as discussed above. These interactions can also be deduced using BMD, however this method can be more cumbersome. For this flow, the BMD modes and bispectrum have been calculated for two regions of the BMD search space described by Schmidt (2020). Two regions are considered as there are symmetries in the

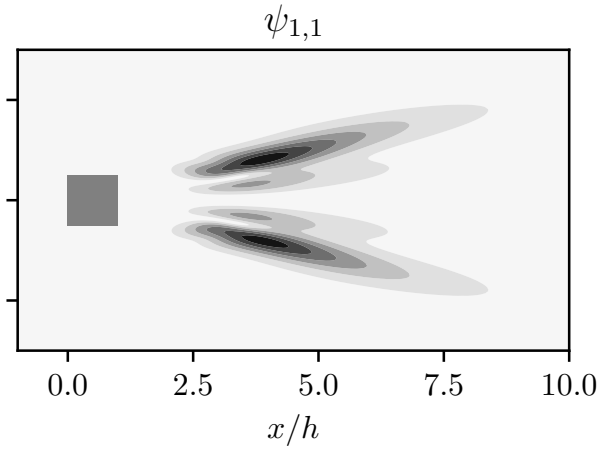

Figure 5.6: BMD interaction map of triad $\{f_1, f_1, f_2\}$ in the streamwise direction for a square cylinder at $Re = 100$.

results due to the periodicity and real-valued flow field data fed into the Fourier decomposition. Results for these regions, consisting of sums and differences of two base frequencies (f_1 and f_2) are presented in figure 5.5. The BMD mode bispectrum shows the value of λ_1 for each triad, representing the maximized bicorrelation between each triplet of modes. This spectrum shows the cascade starting from mode 1 at the shedding frequency of $f^* = 0.15$, which continues through higher modes at the harmonics of this frequency. This is seen in the local maxima of the bispectrum at $(f_1^* = 0.15, f_2^* = 0.15)$ which is correlated to $f_3^* = 0.3$. This interaction, and ensuing interactions between the fundamental frequency and the harmonics, results in the series of peaks in the mode bispectrum that attenuate with increasing frequencies f_1^* and f_2^*. This is similar to the results of Schmidt (2020) for the case of a circular cylinder. This cascade is represented in FANS by the Fourier stress terms in figures 5.2(d) and 5.3(d).

Components of the bispectral mode (ϕ_{1+1}) and interaction map ($\psi_{1,1}$) that correspond to the triad $(f_1 = 0.15, f_2 = 0.15, f_3 = 0.30)$ are shown in figure 5.6 for the streamwise direction. The interaction maps clearly show the interactions between the fundamental frequency and second harmonic that occur in the Karman wake behind the cylinder. This interaction of the triad is similar to the streamwise Fourier stresses on the second harmonic, shown in figure 5.4(a). For the square cylinder case, the local interactions detected by BMD are also captured by FANS. An added benefit

of FANS analysis is that those interactions can be related to other momentum transport terms and the time dependence of the flow, as seen in figures 5.2 and 5.3. This case study supports that FANS is a simpler method that produces insights into flow features and their interactions for for periodic wakes characterised by a single fundamental frequency and its harmonics.

5.2 Swirling Jet

The second flow considered is an axisymmetric swirling jet impinging on a flat plate. This jet flow is selected due to its complicated periodic time signature and the effect of the third velocity component, which arises due to the swirl. The simulation setup and validation are described in Section 4.2.

Herrada et al. (2009) characterized the jet by a large recirculating region along the central axis, called a “vortex breakdown (VB) bubble". There are also several axisymmetric vortex bubbles that originate and decay close to the wall over multiple intervals in each cycle. Herrada et al. (2009) noted the significant outward convection of the circulation due to radial flow from the jet impingement.

The transient vortex bubbles result in a time signature that is composed of large energy concentrations at several discrete frequencies with a base frequency of $f^* = fd/U \approx 0.011$. The energy contained in each mode is shown in figure 5.7. The modes decay exponentially in energy content with increasing frequency. The right bound of the plot represents the Nyquist frequency at $f^* = 0.100$. Modes beyond this frequency are of extremely low magnitude and are thus they are ignored.

Figure 5.8 shows the values of the UTs in FANS at the fundamental frequency. These correspond to the highest energy peak shown in figure 5.7. Significant axial velocity fluctuations are seen throughout the domain. Radial fluctuations are likewise present throughout but become stronger in magnitude downstream due to the presence of vortex bubbles close to the wall. Finally, the azimuthal fluctuations start strongly near the inlet and diminish toward the wall. This gradual

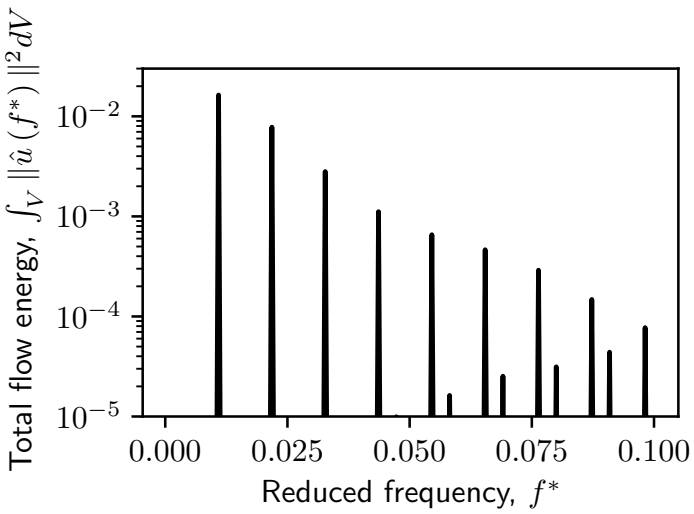

Figure 5.7: Energy contained in each Fourier mode of the swirling jet. Off-harmonic peaks seen between $0.05 < f^* < 0.1$ are due to aliasing but have negligible energy content.

diminishment of fluctuations is due to the outward convection of the swirl noted by Herrada et al. (2009).

Figures 5.9(a) and (b) show the radial mean-flow convection and pressure gradient in the near-inlet region, respectively. These momentum fluxes are of considerably larger magnitude than the UT, peaking at over 45 times the maximum magnitude of the UT. The significant radial force fluctuations are due to the deflection of incoming flow against the VB bubble as indicated in figure 5.9. The interaction of the incoming jet with the VB bubble results in a large opposing pressure gradient. The relative magnitude of the forces combined with the phase of the UT (which can be compared through the sign of the value) shows that the pressure gradients dominate the convection in this region and drive the radial fluctuations. These radial fluctuations are important as they are related to the vortex bubbles that dominate the fluctuating flow. Thus, FANS can be used to elucidate the effect of large counteracting forces and compare them to the time dependent term, which represents the fluctuations at that particular timescale.

Herrada et al. (2009) found that this jet flow is highly sensitive to changes in viscosity. The significant viscous contribution to the momentum transfer close to the inlet in figure 5.10 implies a similar sensitivity. The phase and high magnitude of the azimuthal shear suggests that there is

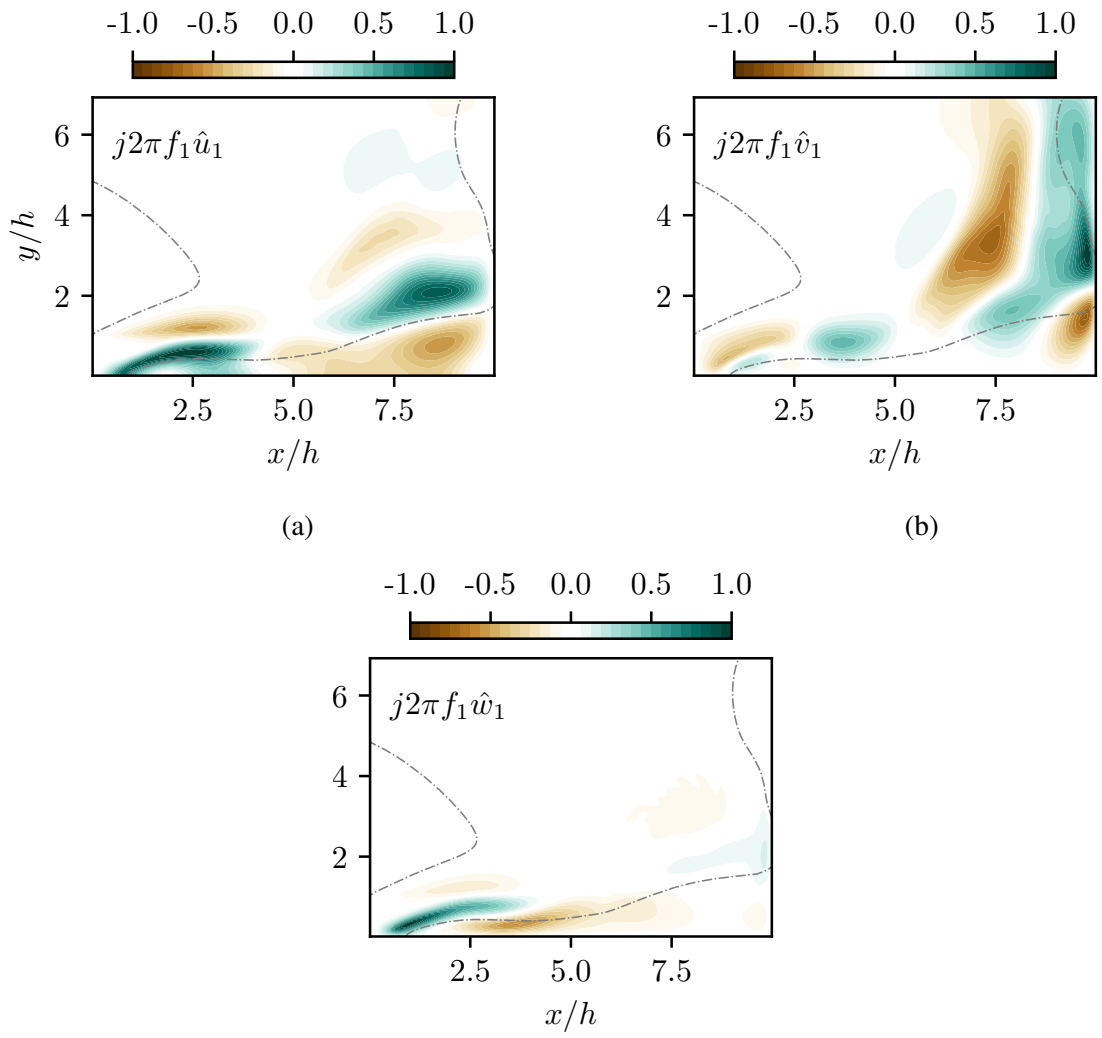

Figure 5.8: Real value of FANS UTs of the swirling jet at the fundamental frequency in each coordinate direction: (a) axial, (b) radial, (c) azimuthal. Grey dashed line indicates $U = 0$ which is extent of VB bubble along the axis.

a dampening effect on the corresponding azimuthal fluctuations. This high shear stress shows the significant effect of the viscosity that results in high sensitivity of the flow physics to changes in the Reynolds number. In this way, FANS provides a platform to gain insight into the stability of the flow configuration.

The intermittent nature of the near-wall vortex bubbles observed in this flow results in a complicated time signature, where the vortex structures are observed across several frequencies.

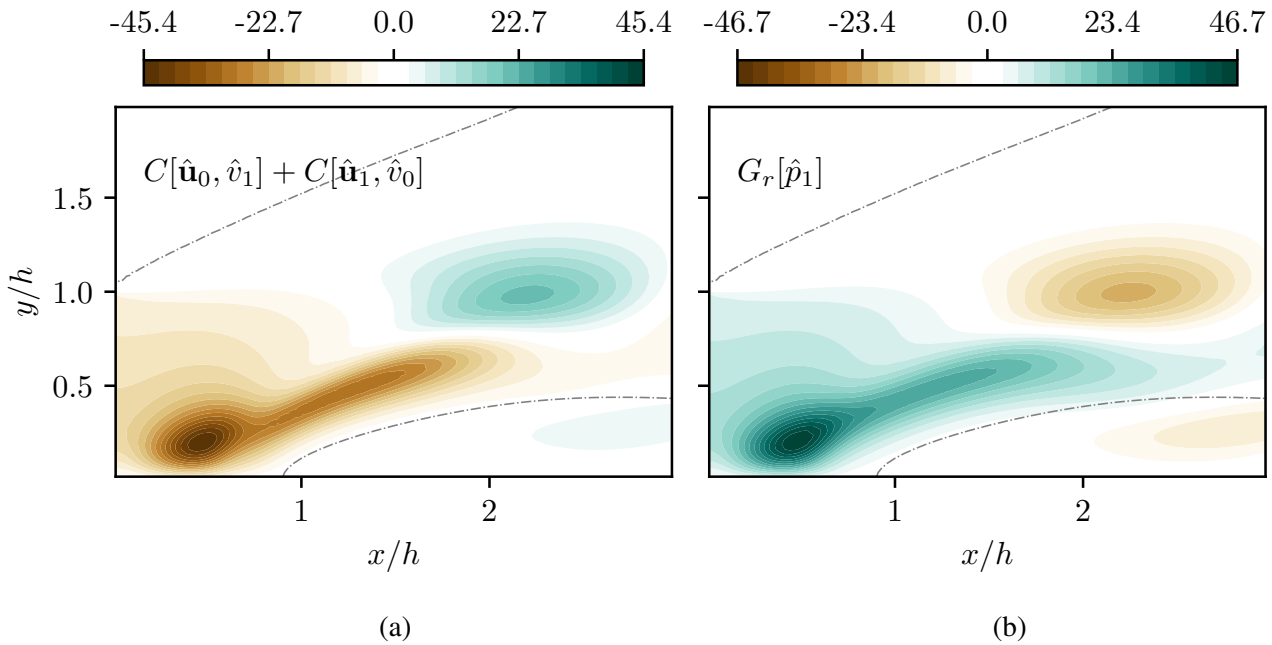

(a) (b)

Figure 5.9: Real value of FANS terms in the radial direction near the inlet of the swirling jet at the fundamental frequency: (a) Mean-flow convection, (b) pressure gradient. Grey line shows extent of VB bubble as in figure 5.8.

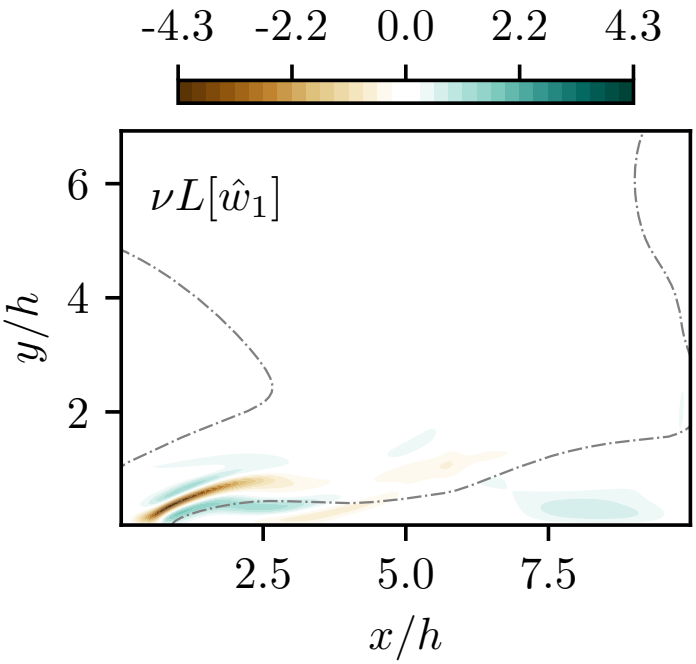

Figure 5.10: Real value of FANS viscous diffusion term of the swirling jet in the azimuthal direction at the fundamental frequency.

This suggests significant coupling between frequency components. To more thoroughly analyse this inter-frequency coupling of the jet flow and its relationship to the flow physics, Fourier stresses are analysed in more detail. Specifically, Fourier stresses represent the interactions that are generated by motion of the intermittent vortex bubbles.

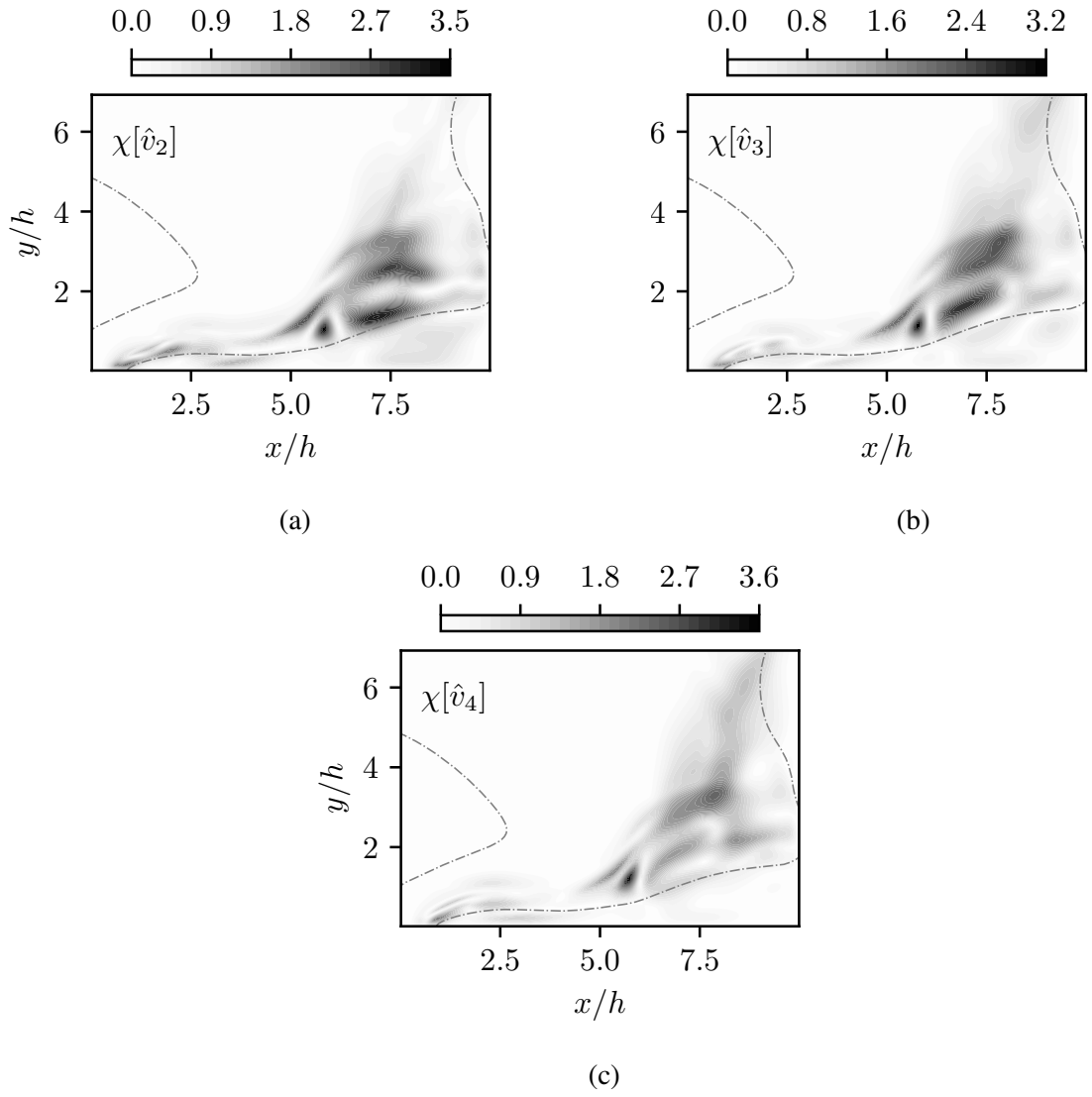

Figure 5.11: Fourier stress magnitude in the radial direction of the swirling jet for (a) Mode 2, (b) Mode 3, (c) Mode 4.

The radial Fourier stress magnitude for modes 2-4 are shown in figure 5.11. The radial terms are selected since they are characteristic of the vortex bubbles but not the swirling inlet flow. Notably, the vast majority of interactions occur outside of the recirculation region, which sits along the

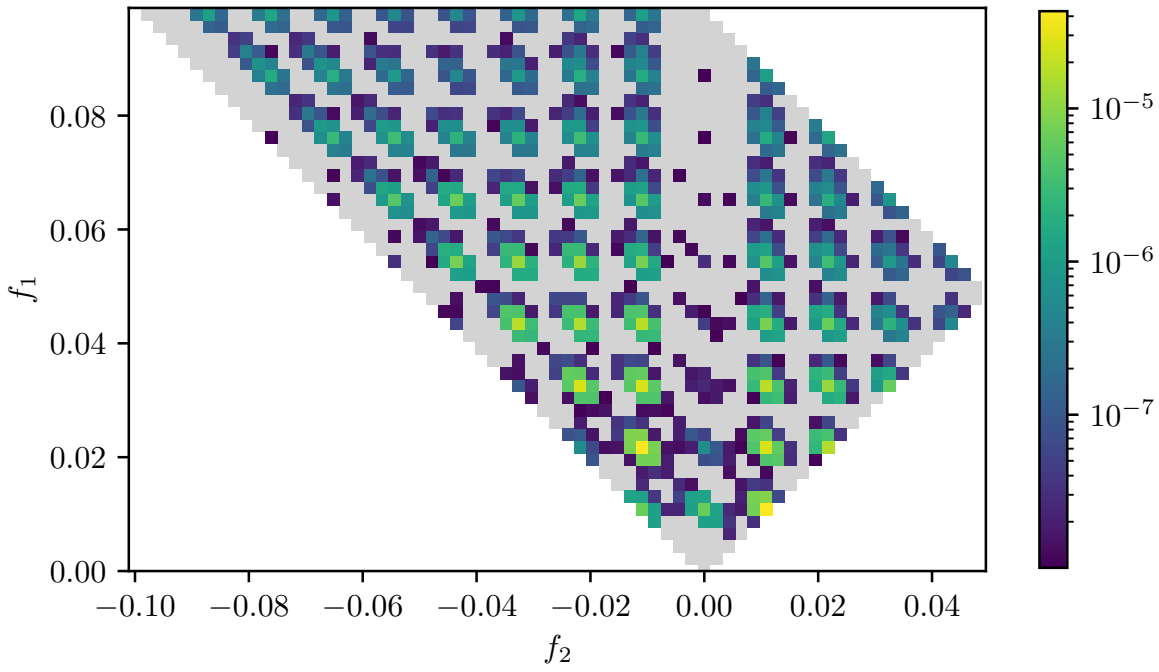

Figure 5.12: Mode bispectrum of the swirling jet flow.

symmetry axis at $y/h = 0$. This follows with the radial movement of the velocity fluctuations as seen in figure 5.9, which is due to interaction of the jet with the recirculation region and the wall. The Fourier stresses have significant magnitude at each mode. This is consistent with the expectation from a cascade of frequency content resulting in a large number of modes. Regions of elevated Fourier stresses are localized well downstream of the inlet and outside of the recirculation region. This matches the expected location of enhanced interaction due to fluctuations induced by the vortex bubbles. Thus, FANS analysis of the convective coupling coincides with physical intuition about the interactions and time signature of the flow.

To further corroborate the influence of the vortex bubble on the inter-harmonic coupling, we explore the flow dynamics using BMD. Results of the bicorrelation coefficients λ_1 for the bispectrum analysis of the jet are shown in figure 5.12. As this flow is periodic, the BMD mode

bispectrum shows a cascade of harmonics, starting with triads involving the fundamental frequency $f^* = fh/U \approx 0.011$. This agrees with the observations of interactions between several modes as seen in figure 5.11.

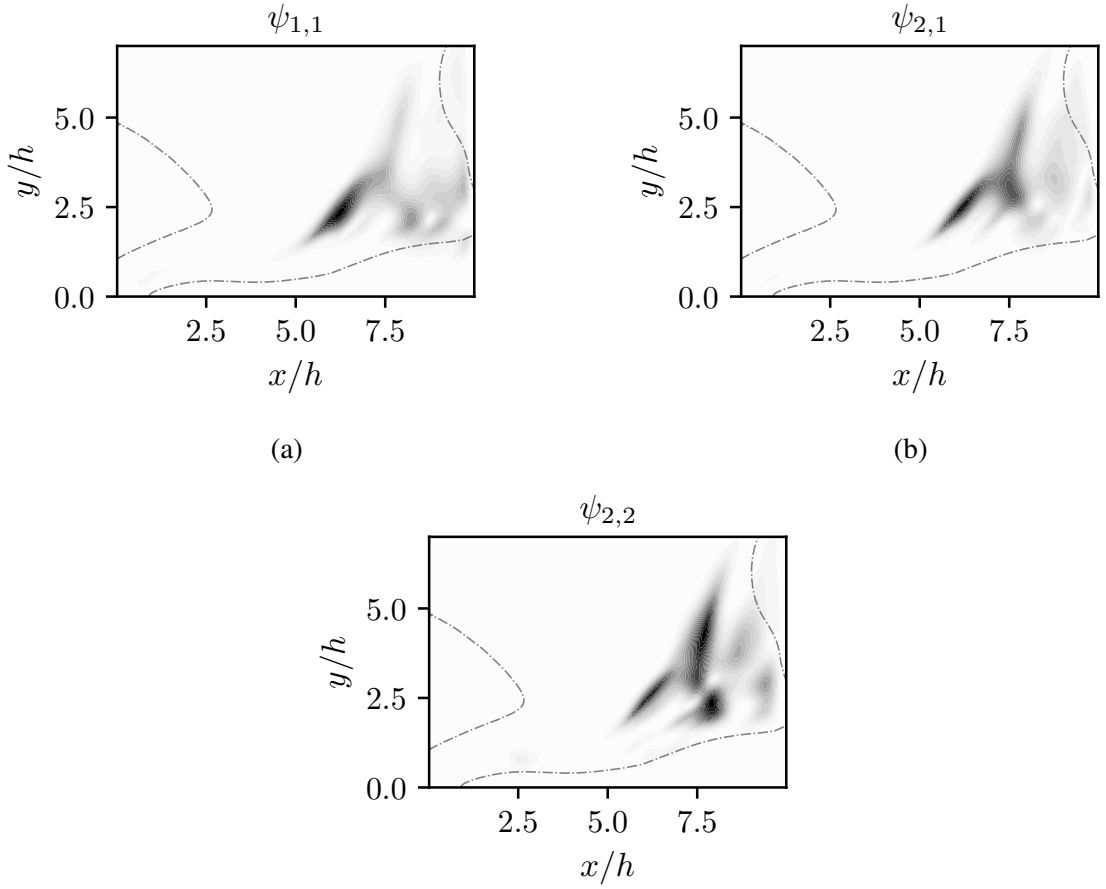

(a) (b) (c)

Figure 5.13: Interaction maps in the radial direction of the swirling jet flow for triads (a) $\psi_{1,1}$, (b) $\psi_{2,1}$ (c) $\psi_{2,2}$.

Figure 5.13 shows the BMD-calculated interaction maps for selected triads corresponding to $(f_1^* = f^*, f_2^* = f^*, f_3^* = 2f^*)$, $(f_1^* = 2f^*, f_2^* = f^*, f_3^* = 3f^*)$, and $(f_1^* = 2f^*, f_2^* = 2f^*, f_3^* = 4f^*)$. Figures 5.13(a-c) represent the radial component of the interaction map for each triad. Similar to FANS, the interactions are found to remain outside of the recirculation region. This is due to the outward forcing of the flow as discussed above. This finding about the interactions supports the conclusions brought by Fourier stresses. The BMD-calculated interaction maps also show the

localization of interactions downstream ($x/h > 5$) and outside of the recirculation region (figure 5.13). This suggests a similar relationship to the vortex bubbles to what was previously observed with radial Fourier stresses. The intermittent motion of the vortex bubbles results in significant interaction between modes, which then appears as enhanced triadic interactions or Fourier stresses detected by BMD and FANS, respectively.

5.3 Side-by-side cylinders

The final case considered is that of two side-by-side cylinders of diameter D at Reynolds number of ($Re = U_\infty D/\nu$) 90. The cylinders are separated by a gap of $0.6D$. These settings and the corresponding mesh requirements were taken from Ma et al. (2017), against which the results are verified, as described in Section 4.3. This flow configuration results in an asymmetric, irregularly oscillating wake characterized by multiple shedding processes and their interaction. There is vortex shedding behind each of the two cylinders, which then merges into a single Karman street far downstream. There is also a “flip-flopping" process where the wake asymmetry changes orientation (Ma et al., 2017). The flip-flop occurs randomly at a frequency much lower than that of the shedding (see Burattini and Agrawal, 2013; Carini et al., 2014). As a result, there are multiple dominant frequencies. Depending on the location in the wake, the flow may be dominated by the low-frequency flip-flopping in between the cylinders, the high-frequency shedding process behind each of the cylinders, or the moderate-frequency shedding process in the wake far from the cylinders due to wake merging. This case is selected to investigate the momentum transport processes detailed by FANS in a nonperiodic case with multiple characteristic frequencies.

The spectrum of the flow energy fluctuations and the estimated power spectral density (S_{xx}) of the drag and lift coefficients on the lower of the two cylinders are shown in figures 5.14(a) and (b) respectively. These broadband spectra show that the flow is irregular and not characterized by discrete frequency content. Within figure 5.14(a), there is a broadband spectrum centred about $f^* = 0.7$, whereas the drag and lift spectrum shows dominant frequencies that are centred around

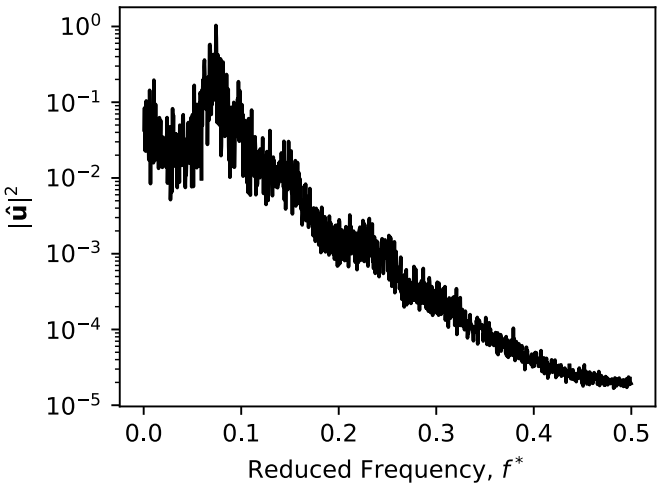

(a)

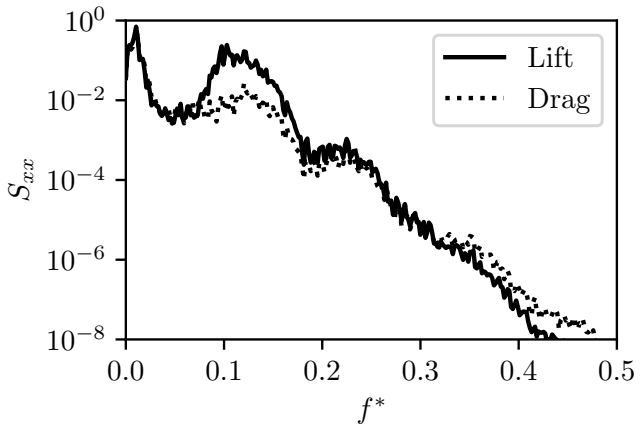

(b)

Figure 5.14: (a) Spectrum of flow energy fluctuations (b) power spectral density of drag and lift coefficients on the lower cylinder.

0.01 and 1.2. The lowest frequency ($f^* = fD/U_\infty \approx 0.01$) corresponds to the flip-flopping process, which occurs on irregular intervals at about this frequency. The moderate frequency shown in the energy spectrum corresponds to the moderate frequency shedding in the merged wake. The highest dominant frequencies in the lift and drag spectra ($0.9 < f^* < 1.5$) correspond to vortex shedding on the cylinder body. The flip-flopping and two vortex production processes will be analyzed using the FANS framework.

Figure 5.15 shows the UT $f^* = 0.0105$. This frequency corresponds to the flip-flopping process. Each of the lobes stemming from the gap represents a state of the flow, where the flow

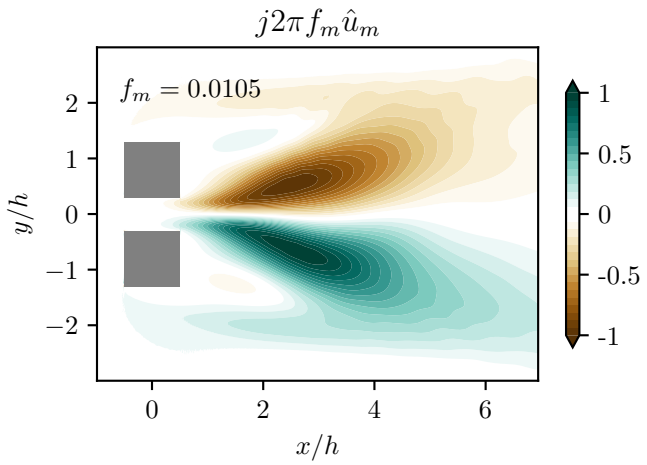

Figure 5.15: Real value of UT at flip-flopping frequency.

through the gap moves toward either the upper or lower cylinder at a given time. Ma et al. (2017) discusses the importance of the gap flow in this regime. Figures 5.16(a-c) show the momentum fluxes in the streamwise direction at the flip-flopping frequency, where the mean-flow convection (figure 5.16a), Fourier stresses (figure 5.16b) and pressure gradient (figure 5.16c) are significant. The diffusion does not contribute significantly to the transport process. These momentum fluxes show the importance of the gap flow to the flip-flopping effect. Large velocity gradients on the leeward side of the gap result in the large convective flux seen in figure 5.16(a) that sustains the switching process. These large velocity gradients are due to the combination of significant gap flow and tight spacing between the cylinders. This combination was highlighted by Ma et al. (2017) as important to the instability that leads to the irregular flow, which is reflected here.

There are also significant Fourier stresses at this frequency, immediately behind the cylinders. These stresses represent interactions of different frequencies within the bands of shedding and Karman street frequencies. Since the bandwidth of the energy and force coefficient spectra is larger than the flip-flopping frequency, interactions between modes that lie within these bands result in Fourier stresses at this frequency.

Figures 5.17 and 5.18 shows the significant momentum fluxes at $f^* = 0.148$. This frequency corresponds to vortex shedding from the individual cylinders, which appears in the force spectra in figure 5.14(b). Evidence of shedding near the cylinders can be seen in the UT and pressure

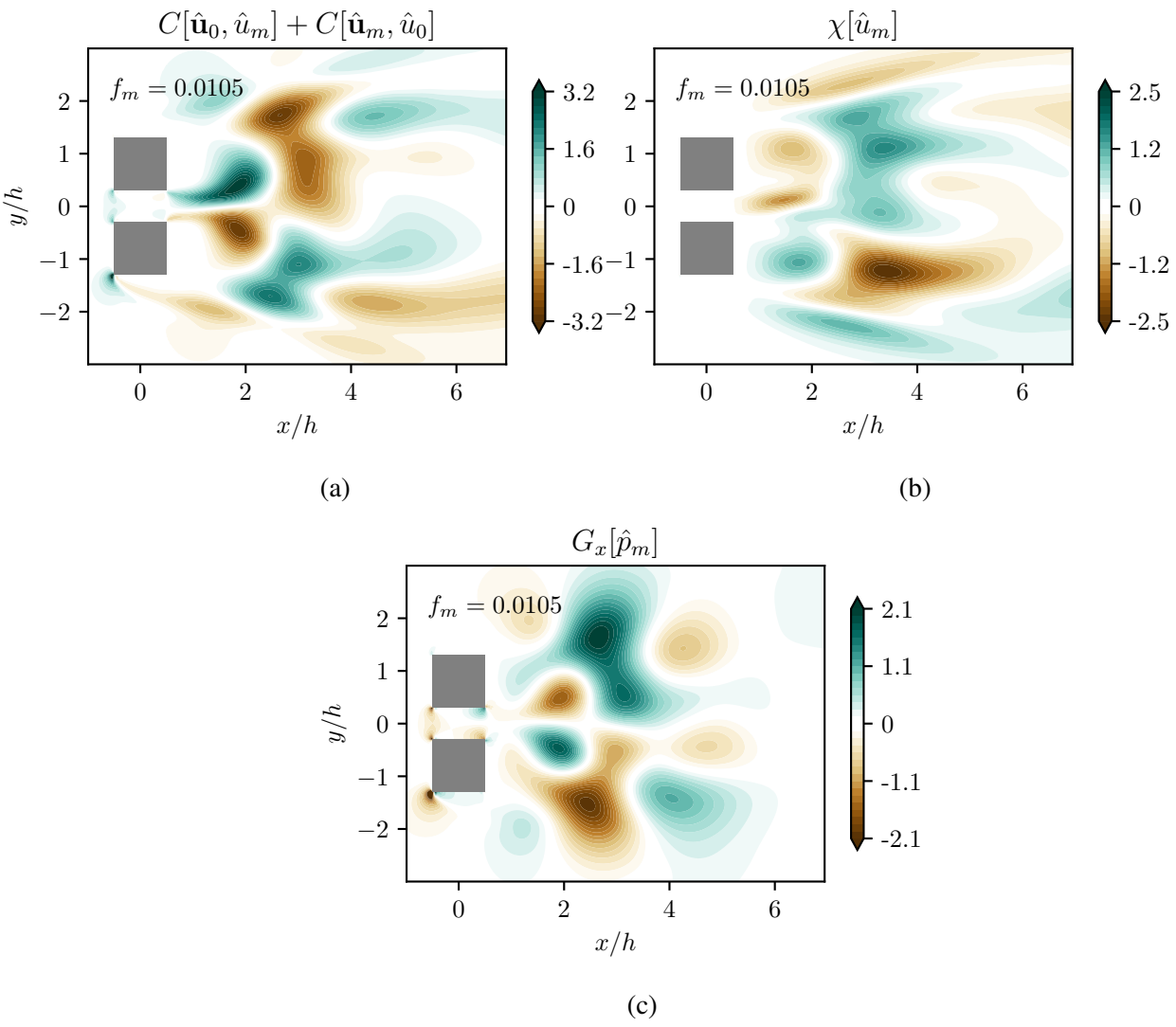

Figure 5.16: Real value of FANS terms in the streamwise direction corresponding to flip-flopping frequencies: (a) Mean-flow convection, (b) Fourier stresses, (c) pressure gradient.

gradient in figures 5.17(a) and 5.18(a), repectively. This aligns with our expectations due to the force fluctuations at this frequency. This mode persists into the far wake, where the Karman vortex street is dominant (figure 5.17(a). This persistence shows that this mode has an effect on the Karman vortex street. This effect is not immediately apparent from the energy spectrum in figure 5.14(a) due to dominance of the lower frequency shedding at $f^* \approx 0.73$ on the overall velocity fluctuations in the wake.

The Fourier stresses in figure 5.18(b) extend throughout the domain and have similar magnitude to the UT. The localization of wake phenomena, such as flip-flopping and the Karman street,

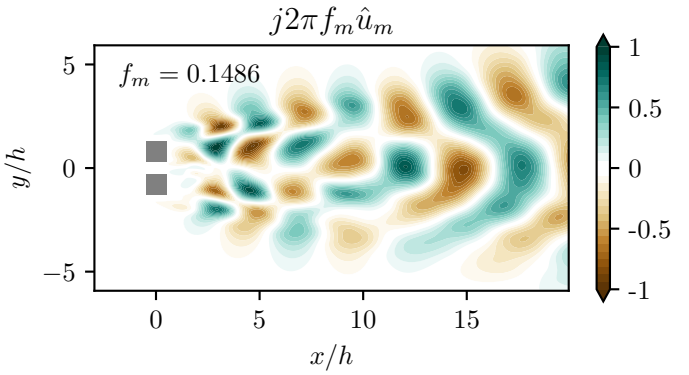

(a)

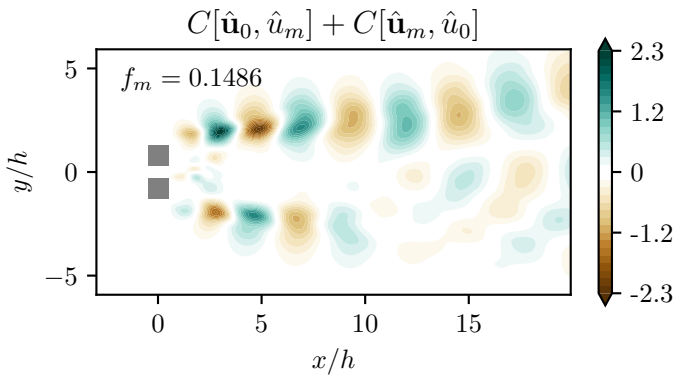

(b)

Figure 5.17: Real values of streamwise momentum fluxes at $f_m^* = 0.148$: (a) UT, (b) mean-flow convection.

suggest that the Fourier stresses at this frequency are due to a broad range of interactions. FANS provides a method to detect the primary mechanisms that contribute to these stresses in the form of individual terms in the Fourier stress term. Select terms are shown in figures 5.19. Modes are subscripted with their frequency due to the broadband spectrum of this flow. For instance, $\hat{u}_{0.075}$ is the streamwise direction of the velocity Fourier mode at $f_m^* = 0.075$. The Fourier stress terms corresponding to the contribution of the main Karman shedding frequency in the far wake is represented in figure 5.19(a). The momentum flux due to this term shows increased magnitude in the region of $x/h > 10$. The increased stress magnitude in this region is related to the formation of the Karman street and the interaction between resultant vortices. Thus, it may be said that the primary driver of Fourier stresses in the far wake is the existence of Karman vortices in this region.

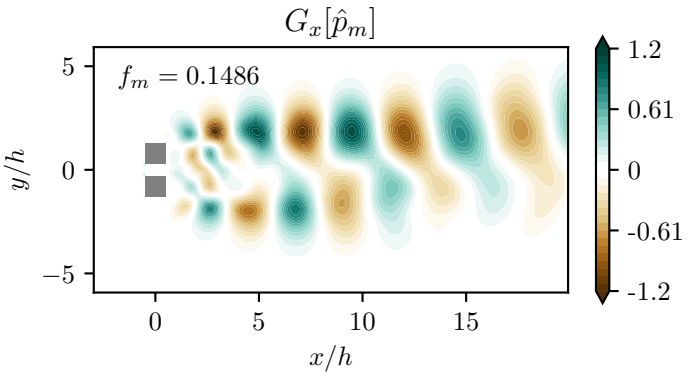

(a)

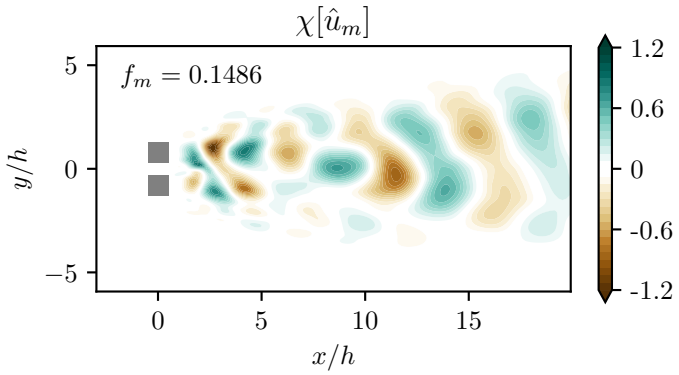

(b)

Figure 5.18: Real values of streamwise momentum fluxes at $f_m^* = 0.148$: (a) pressure, (b) Fourier stresses.

Figure 5.19(b) shows the momentum flux in the same Fourier stress term due to a triad, $(f_1^* = 0.010, f_2^* = 0.138, f_3^* = 0.148)$. The low frequency of 0.010 corresponds to the flip-flopping process. The higher frequency 0.138 is within the frequency band of lift and drag fluctuations. This triad represents one of several similar interactions between these processes (other relevant triads are not shown here for brevity). Magnitude of the convective flux shown in figure 5.19(b) shows that the interaction between these modes is a significant source of momentum for the fluctuations at $f^* \approx 0.148$ immediately behind the cylinders. This suggests that the gap flow and flip-flopping process modulates the vortex shedding. This is supportive of the findings of Ma et al. (2017), who also reported this modulation of the shedding behind the cylinders.

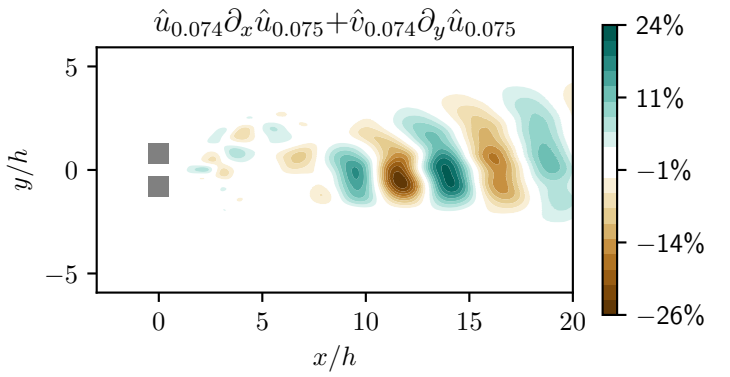

(a)

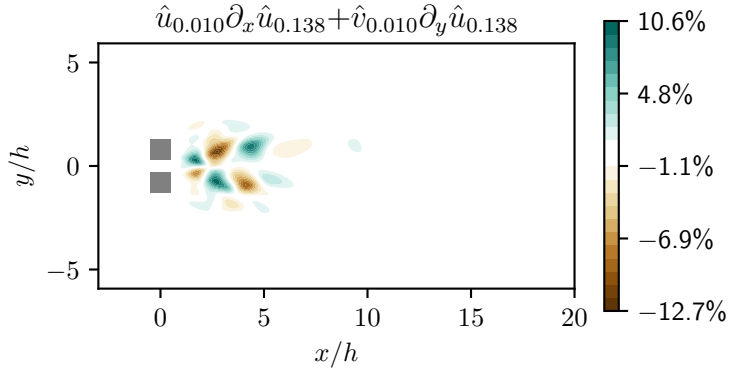

(b)

Figure 5.19: Real values of components of Fourier stresses at $f^* = 0.148$ in the streamwise direction (a) $(f_1^* = 0.074, f_2^* = 0.075)$ (b) $(f_1^* = 0.011, f_2^* = 0.138)$.

We once again utilize BMD to explore the flow dynamics. The spectrum of λ_1 is shown in figure 5.20. There are local maxima in the bispectrum involving frequencies at $f^* \approx 0.73$. The diagonal and vertical bands of elevated correlation around these maxima may be due to spectral leakage (Schmidt, 2020). Locations of the maxima correspond to triads around $(f_1^* \approx 0.73, f_2^* \approx 0.73, f_3^* \approx 0.147)$ and $(f_1^* \approx 0.147, f_2^* \approx -0.73, f_3^* \approx 0.73)$. These triads involve the same frequencies, indicating that they are mirrored and capture the same interactions. The lack of strongly bicorrelated triads involving low frequencies ($f^* \approx 0.01$) is surprising given the significant modulation of the wake due to these frequencies reported by Ma et al. (2017), which were corroborated by the Fourier stresses in figure 5.19(b).

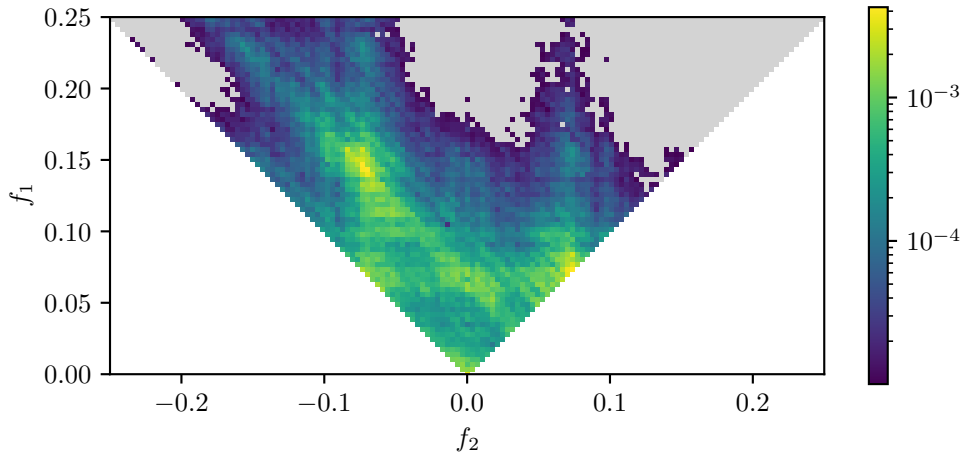

Figure 5.20: BMD mode bispectrum for the dual cylinder case. Spectrum is blanked below 10^{-5} to highlight strongly interacting triads.

Interaction maps corresponding to the triad $(f_1^* \approx 0.73, f_2^* \approx 0.73, f_3^* \approx 0.147)$ are shown in figure 5.21. These correspond to the same wake processes discussed above using FANS. The exact listed frequency is slightly different from the FANS analysis due to the change in resolution, where BMD has lost some frequency resolution due to utilization of multiple windows. The interaction maps show significant triadic interaction beyond $x/D \approx 10$. This corresponds to the merger region, where the wakes of the individual cylinders combine and turn into a single Karman street. The driving frequency of $f_1^* = 0.73$ is characteristic of the vortex street. This frequency is outside of the range of important force spectra seen in figure 5.14. The resultant frequency of $f_3^* = 0.147$ is characteristic of the cylinder-shedding, which continues to have an influence downstream, as was deduced from the FANS analysis. The maps show interaction between these modes in the vortex street far from the cylinders. This interaction is consistent with the behaviour of the Fourier stresses in figure 5.19(a).

Through these case studies, analysing these FANS terms has been shown to be a strong method with easy application and interpretability for providing insights into flow physics. The method directly addresses nonlinear interactions due to convection and relates them to the magnitude of other forces. FANS also includes phase information that can indicate when forces may be counteracting. These properties ease the physical interpretation of flow physics by isolating individual timescales,

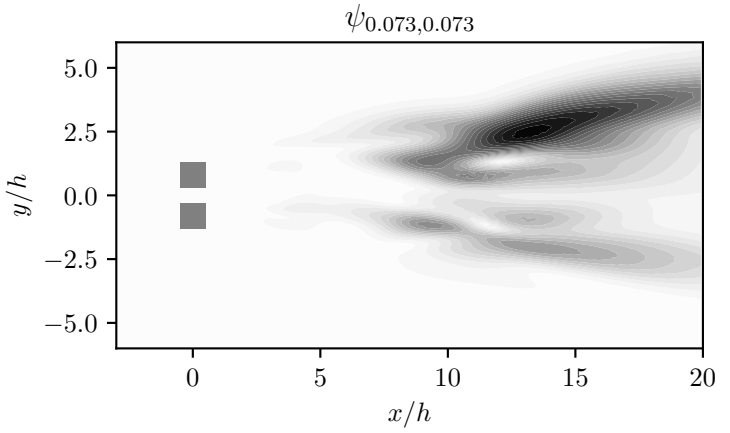

(a)

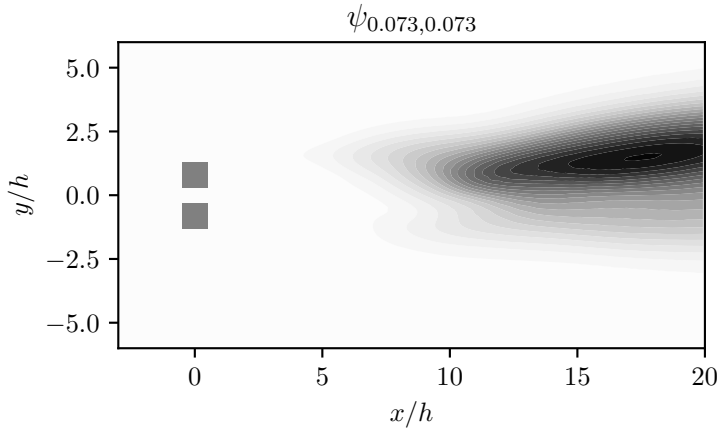

(b)

Figure 5.21: Bispectral interaction maps corresponding to far-wake frequencies, represented by the triad $(f_1^* = 0.073, f_2^* = 0.073, f_3^* = 0.147)$: (a) streamwise (b) transverse components.

and directly relating mode shapes to the governing equations. The method has been shown to be applicable to both periodic and nonperiodic flows. Since the FANS equations are a viable method to identify and describe the behaviour of flows, the method can be applied to more complicated cases to identify new physics.

Chapter 6

THE WAKE OF THIN FLAT PLATES

The final case study in this dissertation involves the effect of end conditions on the three-dimensional wake of long, thin flat plates. This problem is investigated at $Re = 250$ using FANS. End effects on flat plates are a useful final case study because they have highly modulated and three-dimensional wakes (Hemmati et al., 2016a). The implications of end conditions on the wake dynamics are also not yet fully understood (Braun et al., 2020). Thus, the case evaluates the ability of FANS to reveal new physics in a compplex flow. A detailed background on the wake of normal flat plates have been presented in Section 2.4. Mainly, it is not well determined how the end conditions (end plates in experimental setups, spanwise boundary conditions in simulations) impact the force variations on the body, as well as the three-dimensional characteristics of the wake structures behind thin flat plates (Lisoski, 1993; Braun et al., 2020). Flow over three plates with a height of h and width of $2\pi h$ are simulated to investigate the effect of end conditions:

Case 1 has periodic end conditions to establish the dynamics of a plate with an infinite span. The three-dimensional variations of this wake are entirely due to the intrinsically-3D nature of the flow at this Reynolds number. The periodic end condition is the most common in flat-plate simulations for this reason (Najjar, 1994; Hemmati et al., 2018; Singh and Narasimhamurthy, 2018).

Table 6.1: Mean properties of flat plates at $Re = 250$ with different end conditions.

	$\overline{C_d}$	C_l'	St	L_w	h_w
Case 1 (Periodic)	2.29	0.051	0.165	$2.1h$	$0.72h$
Case 2 (Slip)	2.30	0.048	0.166	$2.0h$	$0.73h$
Case 3 (No slip)	2.23	0.021	0.167	$2.6h$	$0.80h$

Case 2 has slip end conditions. This case mimics the effect of end plates without a boundary layer. This case addresses the impact of constraining the spanwise flow along the plate.

Case 3 has no-slip end conditions. This case is implemented to investigate the resulting boundary layer, and the effects of that boundary layer on the wake development and interaction.

The setup and validation of these cases have been shown in Section 4.4.

6.1 Wake observations

Time histories of the force coefficients are shown in Figure 6.1. Cases 1-3 shows evidence of irregular vortex shedding with a low-frequency modulation (Figures 6.1a, 6.1c, 6.1e). Case 3, with no-slip end condition, shows dampening of the overall force fluctuations in both drag and lift compared to Case 1 and Case 2. The maximum drag and lift magnitude for this case is also significantly reduced. Rare spikes of $C_d > 3$ are present in Case 1 and 2 that are not seen in Case 3. The shedding Strouhal number is not significantly different between the cases (Table 6.1). Qualitatively, there is also little change in the shedding structures between cases, shown in terms of λ_2 in Figure 6.2. All three cases are characterized by shedding of spanwise rollers, punctuated by pairs of ribs spaced roughly evenly along the cylinder length. However, Case 3 also has a horseshoe vortex at each wall (Figure 6.2c). This is consistent with boundary layer roll-up in front of an obstacle (Simpson, 2001). The ribs also diffuse more rapidly for Case 3 than Case 1 or Case 2, although the reason for this diffusion is not immediately clear.

Greater differences between the cases are identified in the mean flow characteristics. Table 6.1 shows the recirculation length (L_w) and the wake bubble half-height (h_w) for each case, measured

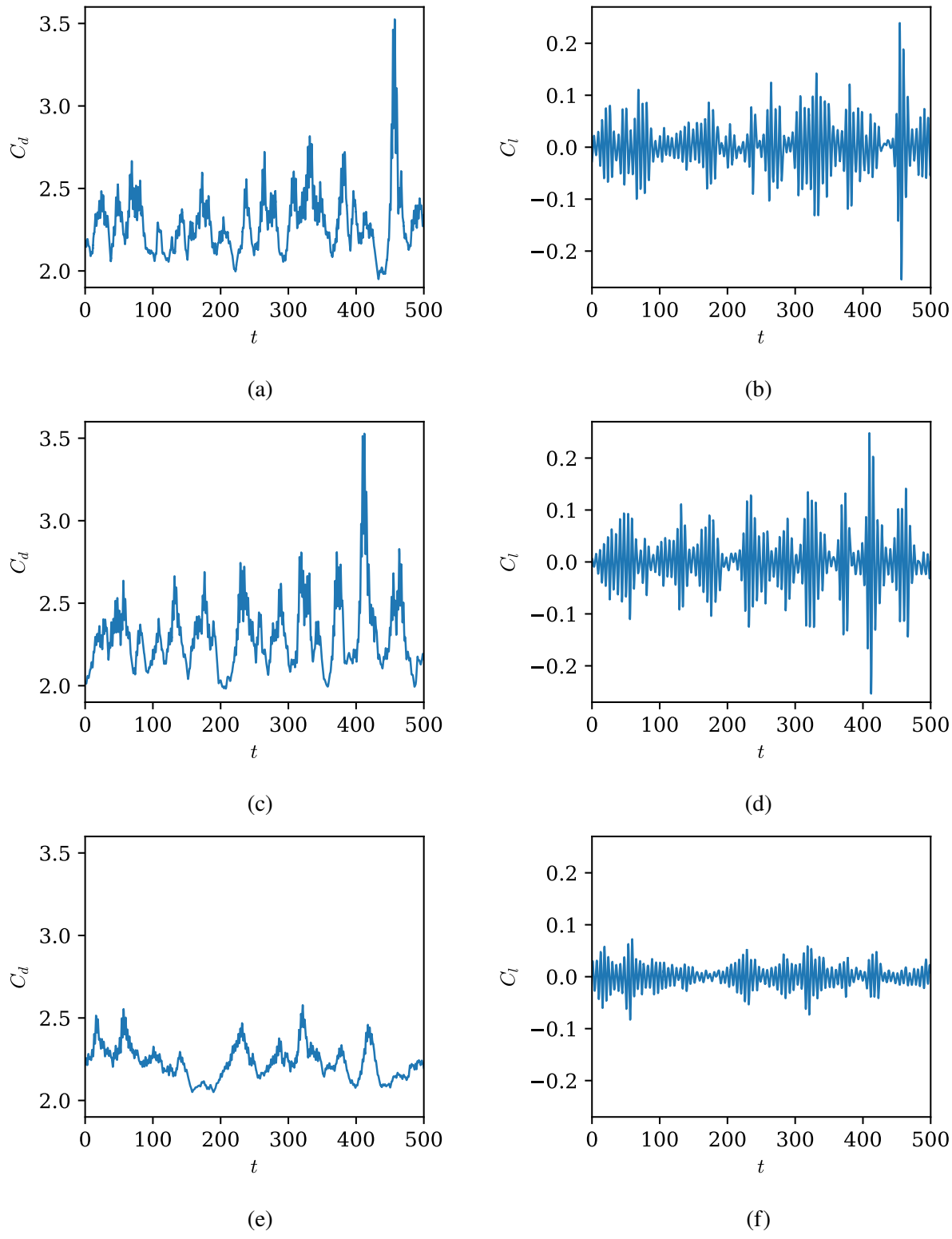

Figure 6.1: Time histories of force coefficients for flat plates at $Re = 250$ with different end conditions: (a),(d) Case 1 (periodic), (b),(e) Case 2 (slip), (c),(f) Case 3 (no slip). Upper row: Drag coefficients. Lower row: Lift coefficients.

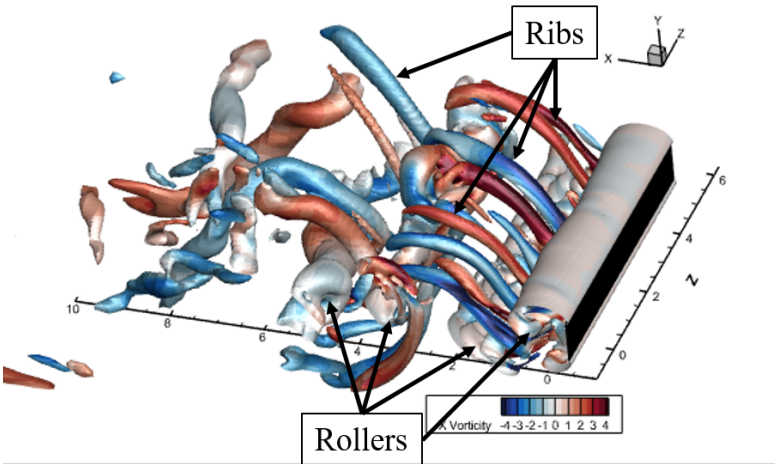

(a)

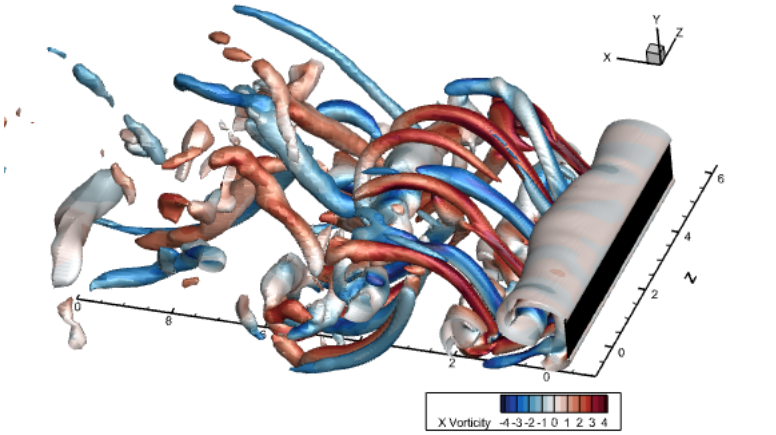

(b)

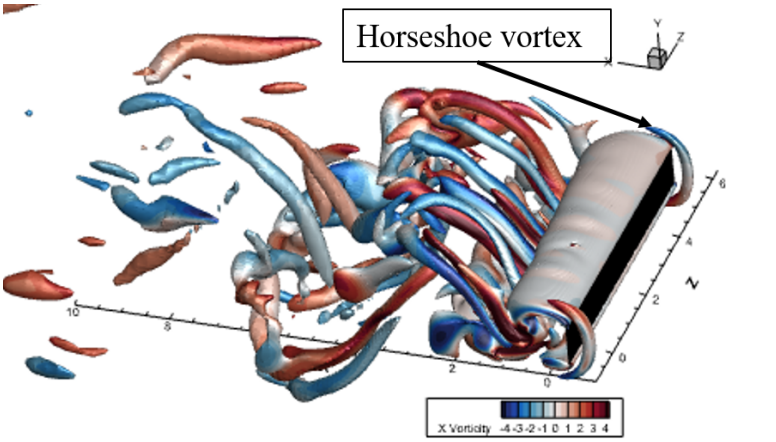

(c)

Figure 6.2: Isosurfaces of $\lambda_2 = 1$ for flat plates with different end conditions at $Re = 250$. (a) Case 1 (periodic), (b) Case 2 (slip), (c) Case 3 (no slip). Snapshots are taken during periods of elevated shedding intensity for comparability.

at the mid-span. There is little difference between Case 1 and Case 2, which have little difference in L_w and h_w. However, the recirculation bubble is larger for Case 3 compared to the other two, i.e. 10% wider and 30% longer than the other two cases. The recirculation regions for each case are shown in Figure 6.3 in terms of mean streamlines at the mid-span. The recirculation regions are qualitatively similar at the midspan, but differ in length and height. The recirculation bubble of Case 3, shown in Figure 6.3(c), is longer and wider than it is for Case 1 and Case 2 (Figures 6.3a and 6.3b), which are almost identical. The no-slip walls in Case 3 also resulted in altered behaviour of the mean wake at the spanwise boundaries. This behaviour is shown in Figure 6.4 using isosurfaces of $U = 0$ and $W = \pm 0.2$. There is recirculating flow immediately in front of the plate, which corresponds to the location of the boundary-layer roll up and the horseshoe vortex. The latter is also characterized by mean spanwise flow toward the walls, shown by the red and blue surfaces in Figure 6.4. Immediately behind the plate, the recirculating region is pushed away from the wall due to the spanwise flow around the plate. The recirculation reattaches to the wall shortly downstream of this position, which is characterized by mean spanwise flow away from the wall in the same region. The boundary layer effects observed here are also important to changes in the fluctuating flow.

The spectrum of the average streamwise energy for each case is shown in Figures 6.5(a), 6.5(c), 6.5(e). All three cases are characterized by a steady reduction of energy fluctuations with increasing frequency, punctuated by sharp increases in fluctuating energy at the Strouhal number and second harmonic. This corresponds to the energy stored in the Karman vortex shedding. However, the most significant changes in the spectrum due to the end conditions are visible in the spanwise energy fluctuations (Figures 6.5b, 6.5d, and 6.5f). The periodic and slip end conditions are characterized by broadband spanwise energy fluctuations in Figures 6.5(b) and 6.5(d), respectively, that notably do not feature significant peaks at the Strouhal number or the harmonics. In contrast, the no-slip end condition (representing a physical end plate) results in peaks at the Strouhal number and second harmonic (Figure 6.5f). Due to the established similarity between Cases 1 and 2, only results from Cases 1 and 3 will be presented from this point on.

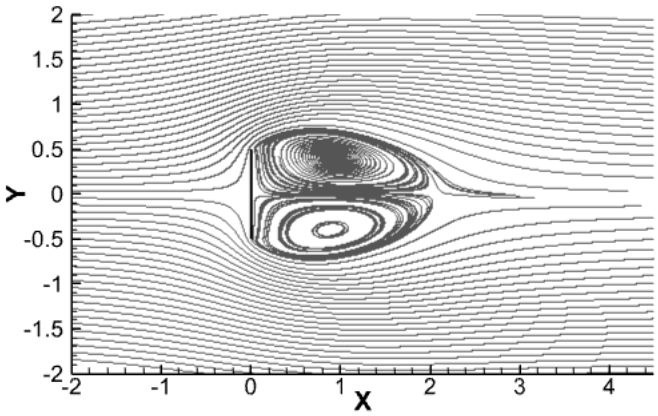

(a)

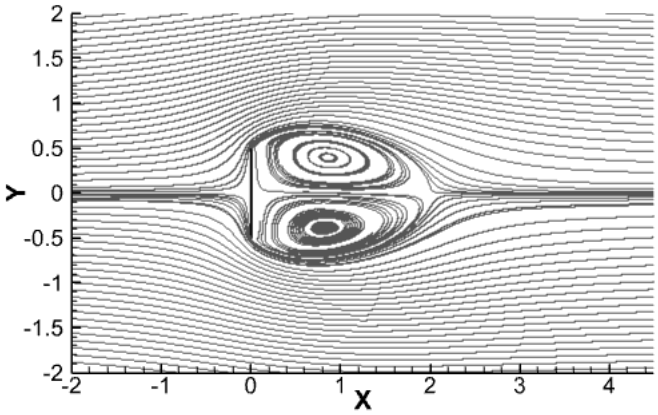

(b)

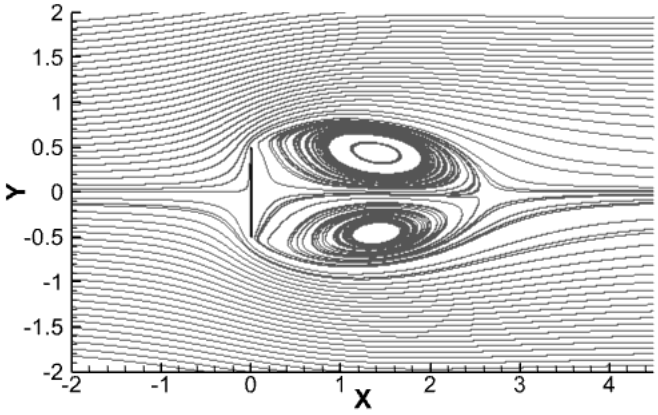

(c)

Figure 6.3: Mean streamlines at vertical centre plane for flat plates with different end conditions at $Re = 250$. (a) Case 1 (periodic), (b) Case 2 (slip), (c) Case 3 (no slip).

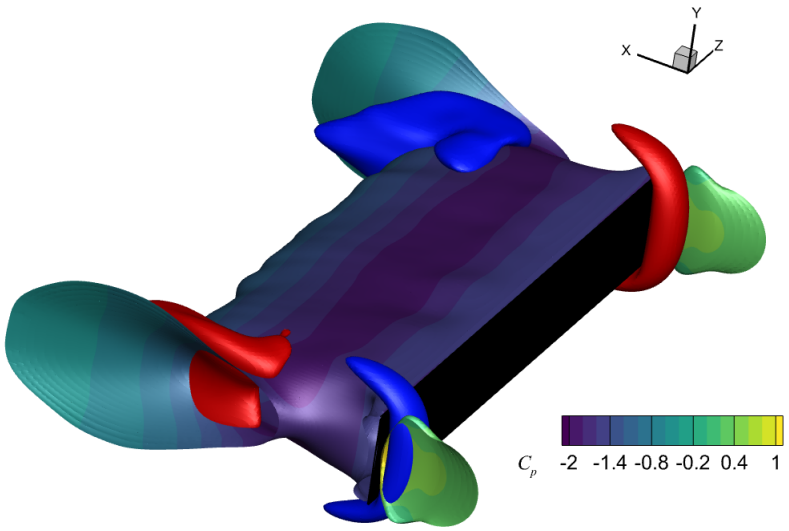

Figure 6.4: Isosurfaces of $U = 0$ for flat plates for Case 3 (no-slip end condition) at $Re = 250$. Blue and red surfaces in are at $W = \pm 0.2$.

6.2 FANS Analysis

Due to the considerable changes in the fluctuating field between cases, the distinct peaks in the energy spectrum that can be associated to the vortex shedding, and the clear role of the boundary layer on these changes, the FANS equations can be easily applied to this case. Transverse Fourier modes are shown at the fundamental frequency (mode 1) in Figure 6.6 for Case 1 and Case 3. The transverse velocity fluctuations are considerably diminished at the mid span in the no slip case. This is consistent with the lowered lift fluctuations in Figure 6.1(f). In order to relate this change to the momentum transport, Figures 6.7 shows the magnitude of the transverse mean-flow convection and pressure gradient terms, measured along the centreline of Figure 6.6. Case 1 is shown in blue and Case 3 in black. The terms are nondimensionalized against the same values in order for direct comparison between cases. Case 3 exhibits a reduction in the peak magnitude of both terms, and this peak occurs further downstream. This lag is connected to the observed reduction in lift fluctuations. The reduced pressure fluctuations immediately behind the plate result in overall lowered pressure differential on the body.

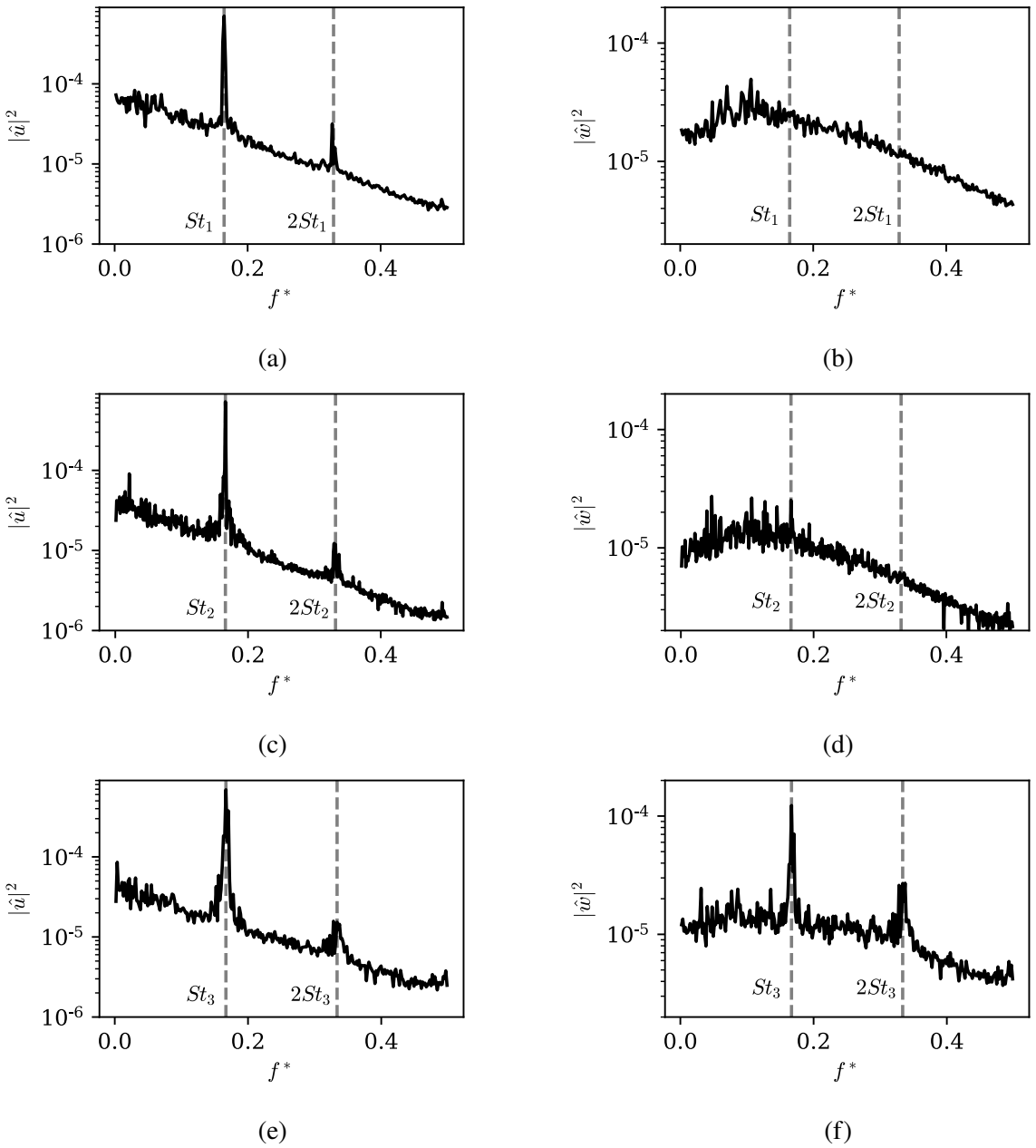

Figure 6.5: Spectrum of energy fluctuations for flat plates with different end conditions at $Re = 250$. Left column (a,c,e): streamwise energy fluctuations. Right column (b,e,f): spanwise energy fluctuations. (a-b) Case 1 (periodic), (c-d) Case 2 (slip), (e-f) Case 3 (no slip).

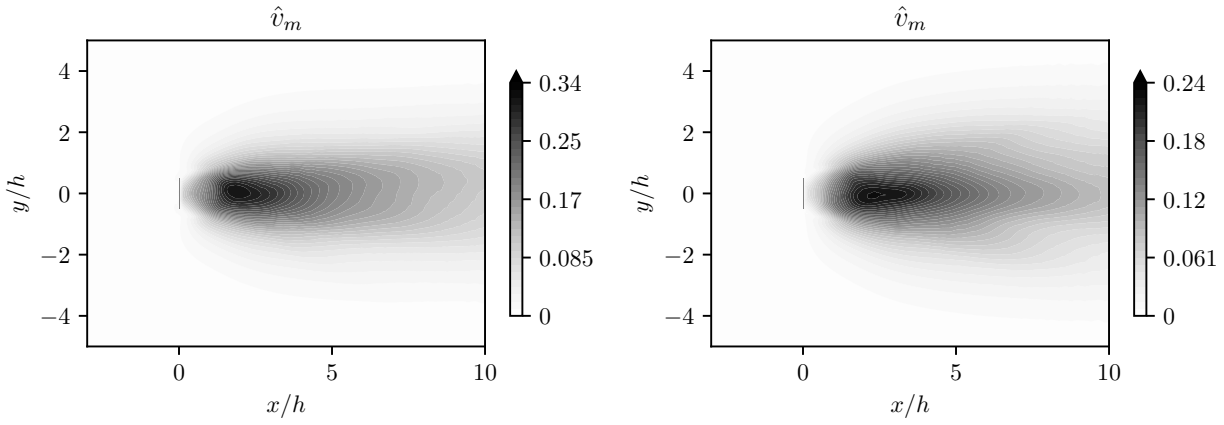

(a) (b)

Figure 6.6: Magnitude of the transverse Fourier mode along the mid-span at the fundamental frequency: (a) Case 1 (periodic), (b) Case 3 (no slip).

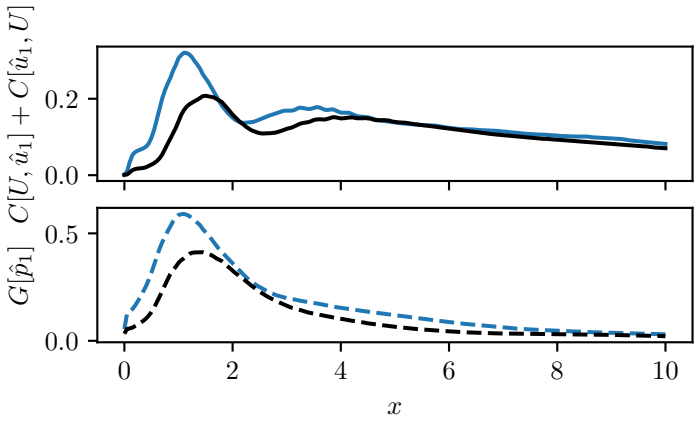

Figure 6.7: Magnitude of the transverse FANS terms along the mid-plate and mid-span ($y = 0$) at the fundamental frequency: Upper: Mean-flow convection. Lower: pressure gradient. Blue lines correspond to Case 1, black lines to Case 3.

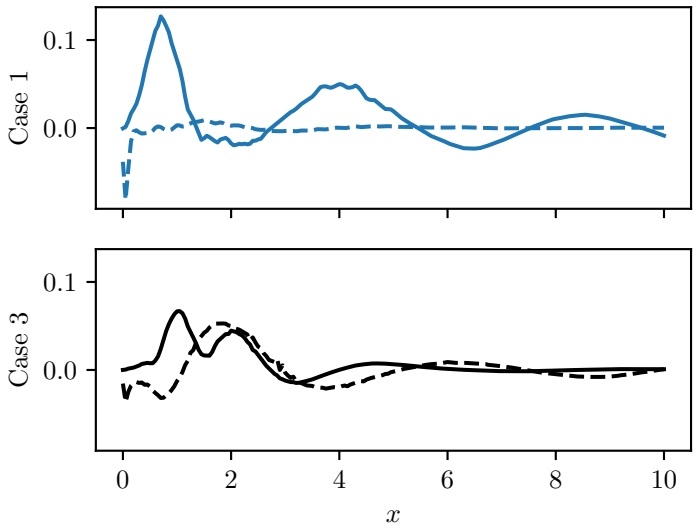

Figure 6.8: Real part of transverse UT and diffusion terms for mode 1 at the mid-plate, near the end plates ($y = 0, z = \pi h$). Solid lines: UT ($j2\pi St\hat{u}_1$), dashed lines: diffusion ($L[\hat{u}_1]$).

Figure 6.8 shows the real component of the spanwise UT and diffusion terms for mode 1, measured at the upper edge of the plate, near the spanwise walls. For Case 3, this location is near or fully in the boundary layer, depending on the streamwise location. The upper plot shows the values for Case 1. The diffusion term (dashed line) has considerably lower magnitude than the UT (solid line) except at the plate ($x = 0$). This aligns with expectations as this represents flow unimpeded by friction against a solid boundary. In contrast, Case 3 (lower plot) shows a relative increase in friction. This is also in line with expectations due to the presence of the boundary layer. Likewise, the two terms are in phase in the region of $1.5 < x/h < 3$. This phase relationship indicates that friction is resisting the fluctuating motion of the flow in this region. Consequently, friction due to the end plates plays a role in diminishing the transverse velocity fluctuations in the flow. This damping effect propagates in the spanwise direction along the plate, which results in the diminished fluctuations in Figure 6.6(b).

The boundary layer also has a significant effect on the spanwise fluctuations in the flow. The spanwise component of Mode 1 for Case 1 and Case 3 are shown in Figure 6.9, taken at the upper edges of the plates. There is a clear increase in the magnitude of fluctuation at this frequency for Case 3, relative to Case 1. This increase in energy, which was also seen in Figure 6.5(f), coincides

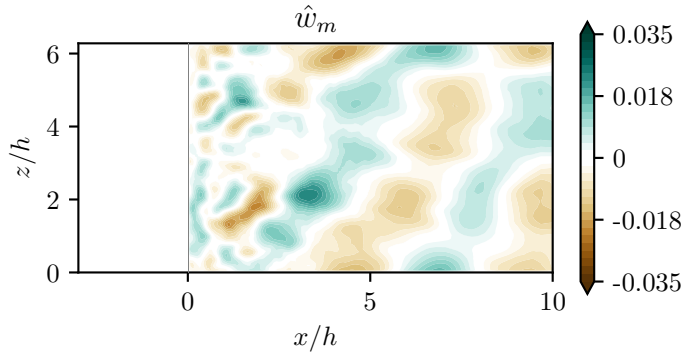

(a)

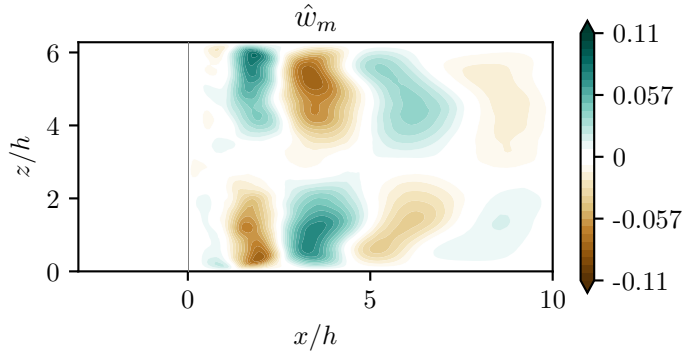

(b)

Figure 6.9: Spanwise Fourier modes at fundamental frequency, measured at the top edge of the plate ($y = 0.5h$). (a) Case 1 (periodic), (b) Case 3 (no slip).

with much greater spatial coherence in the mode. It is also possible that these fluctuations are responsible for the decay of the structures in Figure 6.2(c). The energy is generated by interactions between the boundary layer and the vortex shedding. The momentum fluxes corresponding to the mode in Figure 6.9(b) are shown in Figure 6.10. Cores of the mean-flow convection, pressure gradient, and Fourier stresses (Figure 6.10b, 6.10c, and 6.10d) are localized near the edge of the boundary layer in the range of $2 < x/h < 5$. The strength of these momentum fluxes at the boundary suggests that they are related to the manipulation of the boundary layer by the rollers. The rollers entrain quiescent fluid in the boundary layer as they pass by. This results in spanwise fluctuations of this fluid, which appears as a coherent Fourier mode at the fundamental frequency. These fluctuations then propagate past $x/h = 5$ by the mean-flow convection, while the pressure gradient and Fourier stresses dissipate.

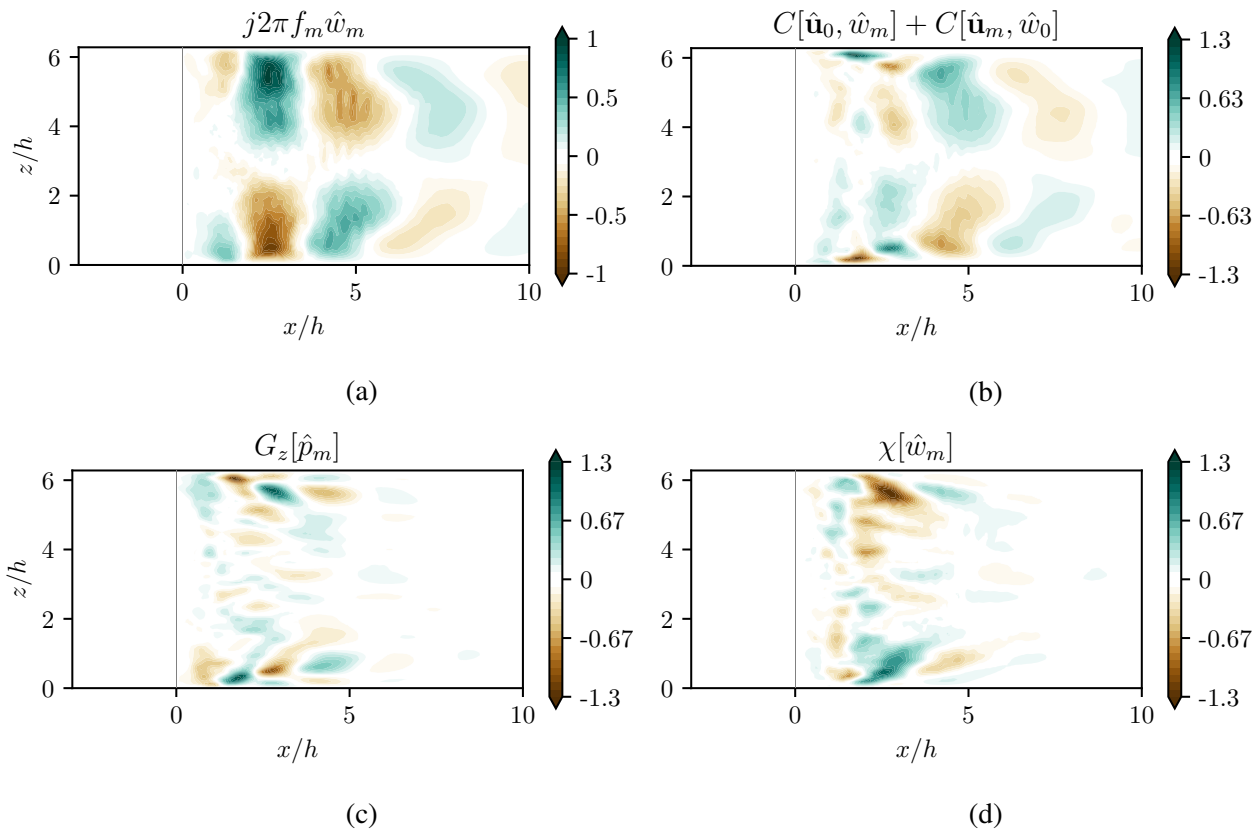

Figure 6.10: Spanwise FANS terms at the top of the plate at the fundamental frequency with no-slip end condition (Case 3, no slip): (a) UT, (b) mean-flow convection, (c) pressure gradient, (d) Fourier stresses. Values are normalized to maximum spanwise acceleration.

It is notable that this spanwise fluctuation is not apparent in the isosurface of λ_2 (Figure 6.2c), and that the Fourier mode by itself does not provide any firm answers as to its origin (Figure 6.9b). This illustrates that the addition of momentum analysis, which is the defining feature of FANS, is useful in educing the mechanisms behind fluctuations in a flow. The remarkable coherence of the Fourier mode at the fundamental frequency also allowed for a straightforward discussion of the average behaviour of the vortex shedding over all time. However, this limited the ability of the method to analyse the mechanism of the low-frequency fluctuations. Overall, this case study showed that FANS-based analysis is a strong option for physics investigations, as it was able to extract previously unknown physics even in a three-dimensional, highly modulated wake.

Chapter 7

CONCLUSIONS

This dissertation presents a new method for analyzing fluid flows governed by the incompressible Navier-Stokes equations. The method utilizes the momentum equations for individual Fourier modes to analyse simulated or experimental flow fields. These equations are referred to as the Fourier-Averaged Navier-Stokes (FANS) equations. The rationale for using these equations is to allow for the direct, localized analysis of recurring forces and interactions in a fluid flow. This is in contrast to other methods, such as Proper Orthogonal Decomposition and Dynamic Mode Decomposition, which do not provide spatial information about interactions in the flow (Schmidt, 2020). As well, those methods are not constructed to consider the Navier-Stokes equations, which makes them flexible (Kutz et al., 2016), but omits key information about the convective, pressure, and viscous forces that govern the flow. In this work, the FANS equations are derived from a Fourier series representation of unsteady pressure and velocity fields that is incorporated into the incompressible Navier-Stokes equations. The basic interpretation of individual terms is discussed alongside practical recommendations for calculating them from flow field snapshots. The method is shown to be successful for analysing regularly and irregularly recurring flow behaviour through case studies. The first three of these cases were periodic vortex shedding in the wake of a square cylinder, a periodic axisymmetric swirling jet impinging on a plate, and nonperiodic shedding over a pair of square cylinders. These cases provided examples of the application of the method and

interpretation of its analysis. In these case studies, the results of the FANS terms are compared to known physics and results from Bispectral Mode Decomposition (BMD). These investigations show that the FANS terms can be related to the physics of the flow in both periodic and nonperiodic cases. The method is then used to investigate previously unknown physics in the 3D wake of thin flat plates. FANS-based analysis is applied to long, thin flat plates with varying spanwise end conditions at Reynolds number of 250. These include a spanwise-periodic base case to represent an infinite span flat plate. This is compared to a case with no-slip end conditions, which are used to mimic the end plates used in wind tunnel experiments. A case with slip end conditions is also presented, in order elucidate the effect of eliminating spanwise flow without creating a boundary layer. These cases are analyzed using FANS to address changes in the lift and transverse velocity fluctuations. The role of the boundary layer in the development of coherent spanwise fluctuations is also demonstrated.

Through these applications, the FANS equations are shown to be particularly strong for momentum analysis of recurring flows. This technique has the capacity to detect similar interactions as BMD, with reduced requirements for the number of samples to capture a particular structure, and without the non-intuitive use of a spectral radius calculation. The interactions can also be directly related to other momentum transport processes. This allows for a quantitative description of the magnitude of a particular interaction between frequency components in terms of the forces that they exert on the flow. The benefits in terms of ease of use and interpretability are especially evident for periodic flows. The analysis is still applicable to irregularly recurring flows, although the interpretation becomes more challenging in situations with broadband spectra. Challenges related to irregularity include the need for additional data to adequately capture all processes, as well as incoherence of individual modes within the broad bands. It should be noted that these challenges are also shared by BMD and other decomposition methods. The method is promising overall, and can be deployed for additional studies into cyclic effects in fluid dynamics.

7.1 Future Work

Beyond applying the method to other cases, there are several avenues to augment the FANS equations and expand its capabilities.

7.1.1 Role of pressure

Pressure in incompressible flows can be viewed as a way of enforcing the conservation of mass (Ferziger et al., 2019). This arises by replacing the pressure in the Navier-Stokes equations as a solution to its Poisson equation:

$$\frac{\partial \mathbf{u}}{\partial t} + \left(I - \nabla\nabla^{-2}\nabla\cdot\right)\mathbf{u}\cdot\nabla\mathbf{u} = \frac{1}{Re}\nabla^2\mathbf{u}$$

The operator $(I - \nabla\nabla^{-2}\nabla\cdot)$ is a projection operator that only preserves the divergence-free component of the convection term, which allows the momentum equations to satisfy conservation of mass. For the FANS equations, this relationship between the pressure and convection indicates that only some of the Fourier stresses have an effect on their corresponding velocity modes, while the remainder only increase the pressure fluctuations. The degree to which the effects of the Fourier stresses on the velocity modes are amplified or diminished by the pressure term can be investigated in future research.

7.1.2 Turbulent kinetic energy and Fourier stresses

A famous consequence of the RANS equations is the turbulent kinetic energy equation and the closure problem that results when models of the Reynolds' stresses are developed (Durbin and Pettersson, 2011). If a truncated series of FANS equations is considered, there would be an analogous closure problem to be considered. The characteristics of the mechanisms that contribute to the Fourier stresses would advance the study of how energy and momentum are transported in turbulent flows.

7.1.3 Modifications of the base method

There are potential modifications of the method that may be implemented to increase the number of use cases and improve the statistical power. For instance, ensemble averaging or the SPOD of Towne et al. (2018) could be added. The application of new operations will result in additional closure terms.

Bibliography

Abramovich, G. (1963). *The theory of turbulent jets*. M.I.T. Press, 1 edition.

Afgan, I., Benhamadouche, S., Han, X., Sagaut, P., and Laurence, D. (2013). Flow over a flat plate with uniform inlet and incident coherent gusts. *Journal of Fluid Mechanics*, 720:457–485.

Agrey, K. (2021). Coherent dynamics and energetics in thin flat plate wakes. Master's thesis, University of Calgary.

Ahmed, S., Ramm, G., and Faltin, G. (1984). Some salient features of the time-averaged ground vehicle wake. In *SAE International Congress and Exposition*. SAE International.

Araya, D. B., Colonius, T., and Dabiri, J. O. (2017). Transition to bluff-body dynamics in the wake of vertical-axis wind turbines. *Journal of Fluid Mechanics*, 813:346–381.

Aris, R. (1989). *Vectors, Tensors, and the Basic Equations of Fluid Mechanics*. Dover Publications Inc., 1 edition.

Bai, H. and Alam, M. M. (2018). Dependence of square cylinder wake on reynolds number. *Physics of Fluids*, 30(1):015102.

Balachandar, S., Mittal, R., and Najjar, F. M. (1997). Properties of the mean recirculation region in the wakes of two-dimensional bluff bodies. *Journal of Fluid Mechanics*, 351:167–199.

Barkley, D. and Henderson, R. D. (1996). Three-dimensional floquet stability analysis of the wake of a circular cylinder. *Journal of Fluid Mechanics*, 322:215–241.

Batchelor, G. K. (1999). *An Introduction to Fluid Dynamics.*, volume 2nd pbk. ed of *Cambridge Mathematical Library*. Cambridge University Press.

Bauer, W., Cotter, C., and Wingate, B. (2022). Higher order phase averaging for highly oscillatory systems. *Multiscale Modeling & Simulation*, 20(3):936–956.

Beneddine, S. (2017). *Characterization of unsteady flow behavior by linear stability analysis*. Theses, Univ. Paris-Saclay.

Bistafa, S. R. (2018). On the development of the navier-stokes equation by navier. *Revista Brasileira de Ensino de Física*, 40(2).

Braun, E., Agrey, K., and Martinuzzi, R. J. (2020). End effects of nominally two-dimensional thin flat plates. *International Journal of Heat and Fluid Flow*, 86:108719.

Buntine, J. D. and Saffman, P. G. (1995). Inviscid swirling flows and vortex breakdown. *Proceedings of the Royal Society of London. Series A: Mathematical and Physical Sciences*, 449(1935):139–153.

Burattini, P. and Agrawal, A. (2013). Wake interaction between two side-by-side square cylinders in channel flow. *Computers & Fluids*, 77:134–142.

Carini, M., Giannetti, F., and Auteri, F. (2014). On the origin of the flip–flop instability of two side-by-side cylinder wakes. *Journal of Fluid Mechanics*, 742:552–576.

Carlson, D. R., Widnall, S. E., and Peeters, M. F. (1982). A flow-visualization study of transition in plane poiseuille flow. *Journal of Fluid Mechanics*, 121:487–505.

Carte, G., Dušek, J., and Fraunié, P. (1995). A spectral time discretization for flows with dominant periodicity. *Journal of Computational Physics*, 120(2):171–183.

Chen, K. K., Tu, J. H., and Rowley, C. W. (2012). Variants of dynamic mode decomposition: Boundary condition, koopman, and fourier analyses. *Journal of Nonlinear Science*, 22:887–915.

Drazin, P. and Riley, N. (2006). *The Navier-Stokes equations: a classification of flows and exact solutions*. Cambridge University Press.

Duraisamy, K., Iaccarino, G., and Xiao, H. (2019). Turbulence modeling in the age of data. *Annual Review of Fluid Mechanics*, 51:357–377.

Durbin, P. A. and Pettersson, R. B. A. (2011). *Statistical theory and modeling for turbulent flows*. Wiley, 2 edition.

Eriksen, P. E. and Krogstad, P. (2017). An experimental study of the wake of a model wind turbine using phase-averaging. *International Journal of Heat and Fluid Flow*, 67:52–62. Symposium on Experiments and Simulations in Fluid Dynamics Research.

Ferziger, J. H., Perić, M., and Street, R. L. (2019). *Computational Methods for Fluid Dynamics*. Springer Cham, 4 edition.

Fogaing, M. B. T., Hemmati, A., Lange, C. F., and Fleck, B. A. (2019). Performance of turbulence models in simulating wind loads on photovoltaics modules. *Energies*, 12(17).

Foias, C., Manley, O., Rosa, R., and Temam, R. (2001). *Navier-Stokes Equations and Turbulence*. Encyclopedia of Mathematics and its Applications. Cambridge University Press.

Garrick, I. (1936). Propulsion of a flapping and oscillating foil, NACA Tech. Rep. 567.

Gioria, R., Jabardo, P., Carmo, B., and Meneghini, J. (2009). Floquet stability analysis of the flow around an oscillating cylinder. *Journal of Fluids and Structures*, pages 676–686.

Girimaji, S. S. (2005). Partially-Averaged Navier-Stokes Model for Turbulence: A Reynolds-Averaged Navier-Stokes to Direct Numerical Simulation Bridging Method. *Journal of Applied Mechanics*, 73(3):413–421.

Goldstein, S. (1969). Fluid mechanics in the first half of this century. *Annual Review of Fluid Mechanics*, 1(1):1–29.

Gómez, F., Blackburn, H. M., Rudman, M., McKeon, B. J., Luhar, M., Moarref, R., and Sharma, A. S. (2014). On the origin of frequency sparsity in direct numerical simulations of turbulent pipe flow. *Physics of Fluids*, 26(10):101703.

Hall, K. C., Thomas, J. P., and Clark, W. S. (2002). Computation of unsteady nonlinear flows in cascades using a harmonic balance technique. *AIAA J.*, 40(5):879–886.

He, K., Minelli, G., Wang, J., Dong, T., Gao, G., and Krajnović, S. (2021). Numerical investigation of the wake bi-stability behind a notchback ahmed body. *Journal of Fluid Mechanics*, 926:A36.

Hemmati, A. (2016). *Evolution of Large-Scale Structures in the Wake of Sharp-Edge Thin Flat Bodies*. PhD thesis, University of Calgary.

Hemmati, A., Wood, D. H., and Martinuzzi, R. J. (2016a). Characteristics of distinct flow regimes in the wake of an infinite span normal thin flat plate. *International Journal of Heat and Fluid Flow*, 62:423–436.

Hemmati, A., Wood, D. H., and Martinuzzi, R. J. (2016b). Effect of side-edge vortices and secondary induced flow on the wake of normal thin flat plates. *International Journal of Heat and Fluid Flow*, 61:197–212. SI TSFP9 special issue.

Hemmati, A., Wood, D. H., and Martinuzzi, R. J. (2018). On simulating the flow past a normal thin flat plate. *Journal of Wind Engineering and Industrial Aerodynamics*, 174:170–187.

Herrada, M. A., Del Pino, C., and Ortega-Casanova, J. (2009). Confined swirling jet impingement on a flat plate at moderate reynolds numbers. *Physics of Fluids*, 21(1):013601.

Herrada, M. A., Pérez-Saborid, M., and Barrero, A. (2003). Vortex breakdown in compressible flows in pipes. *Physics of Fluids*, 15(8):2208–2218.

Holmes, P., Lumley, J. L., Berkooz, G., and Rowley, C. W. (2012). *Turbulence, Coherent Structures, Dynamical Systems and Symmetry.*, volume 2nd ed of *Cambridge Monographs on Mechanics*. Cambridge University Press.

Iaccarino, G., Ooi, A., Durbin, P., and Behnia, M. (2003). Reynolds averaged simulation of unsteady separated flow. *International Journal of Heat and Fluid Flow*, 24(2):147–156.

Jakirlić, S. and Maduta, R. (2015). Extending the bounds of "steady" rans closures: Toward an instability-sensitive reynolds stress model. *International Journal of Heat and Fluid Flow*, 51:175–194. Theme special issue celebrating the 75th birthdays of Brian Launder and Kemo Hanjalic.

Jang, H. K., Ozdemir, C. E., Liang, J.-H., and Tyagi, M. (2021). Oscillatory flow around a vertical wall-mounted cylinder: Dynamic mode decomposition. *Physics of Fluids*, 33(2):025113.

Jeong, J. and Hussain, F. (1995). On the identification of a vortex. *Journal of Fluid Mechanics*, 285:69–94.

Khalid, M. S. U., Wang, J., Akhtar, I., Dong, H., and Liu, M. (2020). Modal decompositions of the kinematics of crevalle jack and the fluid–caudal fin interaction. *Bioinspiration and Biomimetics*, 16(1):016018.

Kirchgassner, K. (1975). Bifurcation in nonlinear hydrodynamic stability. *SIAM Review*, 17(4):652–683.

Krumbein, B., Maduta, R., Jakirlić, S., and Tropea, C. (2020). A scale-resolving elliptic-relaxation-based eddy-viscosity model: Development and validation. In Dillmann, A., Heller, G., Krämer, E., Wagner, C., Tropea, C., and Jakirlić, S., editors, *New Results in Numerical and Experimental Fluid Mechanics XII*, pages 90–100, Cham. Springer International Publishing.

Kutz, J. N., Brunton, S. L., Brunton, B. W., and Proctor, J. L. (2016). *Dynamic Mode Decomposition: Data-Driven Modeling of Complex Systems*. Society for Industrial and Applied Mathematics, 1 edition.

Liang, H. and Maxworthy, T. (2005). An experimental investigation of swirling jets. *Journal of Fluid Mechanics*, 525:115–159.

Lisoski, D. (1993). *Nominally 2-dimensional flow about a normal flat plate*. PhD thesis, California Institute of Technology.

Liu, I.-H. and Oztekin, A. (2018). Three-dimensional transient flows past plates translating near a wall. *Ocean Engineering*, 159:9–21.

Lumley, J. (1970). *Stochastic Tools in Turbulence*. Academic Press, 1 edition.

Ma, S., Kang, C.-W., Lim, T.-B. A., Wu, C.-H., and Tutty, O. (2017). Wake of two side-by-side square cylinders at low reynolds numbers. *Physics of Fluids*, 29(3):033604.

Mantic-Lugo, V., Arratia, C., and Gallaire, F. (2015). A self-consistent model for the saturation dynamics of the vortex shedding around the mean flow in the unstable cylinder wake. *Physics of Fluids*, 27(7):074103.

Meliga, P. (2017). Harmonics generation and the mechanics of saturation in flow over an open cavity: a second-order self-consistent description. *Journal of Fluid Mechanics*, 826:503–521.

Meliga, P., Boujo, E., and Gallaire, F. (2016). A self-consistent formulation for the sensitivity analysis of finite-amplitude vortex shedding in the cylinder wake. *Journal of Fluid Mechanics*, 800:327–357.

Menter, F. R. and Egorov, Y. (2010). The scale-adaptive simulation method for unsteady turbulent flow predictions. part 1: Theory and model description. *Flow, Turbulence and Combustion*, 85:113–138.

Najjar, F. M. (1994). *Direct Numerical Simulations of Separated and Separated-Reattaching Flows on Massively Parallel Processing Computers*. PhD thesis, University of Illinois at Urbana-Champaign.

Najjar, F. M. and Balachandar, S. (1998). Low-frequency unsteadiness in the wake of a normal flat plate. *Journal of Fluid Mechanics*, 370:101–147.

Najjar, F. M. and Vanka, S. P. (1995a). Effects of intrinsic three-dimensionality on the drag characteristics of a normal flat plate. *Physics of Fluids*.

Najjar, F. M. and Vanka, S. P. (1995b). Simulations of the unsteady separated flow past a normal flat plate. *International Journal for Numerical Methods in Fluids*, pages 525–547.

Narasimhamurthy, V. D. and Andersson, H. I. (2009). Numerical simulation of the turbulent wake behind a normal flat plate. *International Journal of Heat and Fluid Flow*, 30(6):1037–1043.

Noack, B. R., Afanasiev, K., Morzynski, M., Tadmor, G., and Thiele, F. (2003). A hierarchy of low-dimensional models for the transient and post-transient cylinder wake. *Journal of Fluid Mechanics*, 497:335–363.

Noack, B. R., Stankiewicz, W., Morzyński, M., and Schmid, P. J. (2016). Recursive dynamic mode decomposition of transient and post-transient wake flows. *Journal of Fluid Mechanics*, 809:843–872.

Ostermann, F., Woszidlo, R., Nayeri, C. N., and Paschereit, C. O. (2015). Phase-averaging methods for the natural flowfield of a fluidic oscillator. *AIAA Journal*, 53(8):2359–2368.

Phares, D. J., Smedley, G. T., and Flagan, R. C. (2000). The wall shear stress produced by the normal impingement of a jet on a flat surface. *Journal of Fluid Mechanics*, 418:351–375.

Picard, C. and Delville, J. (2000). Pressure velocity coupling in a subsonic round jet. *International Journal of Heat and Fluid Flow*, 21(3):359–364.

Qing, L. (2004). *Development of Reduced-Order Models for Lift and Drag on Oscillating Cylinders with Higher-Order Spectral Moments*. PhD thesis, Virginia Tech.

Rojas, E., Burgos Olmos, M., Pino, C., and Fernandez-Feria, R. (2008). Three-dimensional structure of confined swirling jets at moderately large reynolds numbers. *Physics of Fluids*, 20.

Roshko, A. (1993). Perspectives on bluff body aerodynamics. *Journal of Wind Engineering and Industrial Aerodynamics*, 49(1):79–100.

Rowley, C. W. and Dawson, S. T. (2017). Model reduction for flow analysis and control. *Annual Review of Fluid Mechanics*, 49(1):387–417.

Rowley, C. W., Mezic, I., Bagheri, S., Schlatter, P., and Henningson, D. S. (2009). Spectral analysis of nonlinear flows. *Journal of Fluid Mechanics*, 641:115–127.

Sadri, R. M. (1999). *Channel entrance flow.* PhD thesis, University of Western Ontario.

Schlichting, H., Gersten, K., Krause, E., Oertel, H., and Mayes, K. (2000). *Boundary-layer theory.* Springer-Verlag.

Schmid, P., Li, L., Juniper, M., and Pust, O. (2011). Applications of the dynamic mode decomposition. *Theoretical Computational Fluid Dynamics*, 25:249–259.

Schmid, P. J. and Henningson, D. S. (2001). *Stability and Transition in Shear Flows*. Springer, 1 edition.

Schmidt, O. T. (2020). Bispectral mode decomposition of nonlinear flows. *Nonlinear Dynamics*, 102(4):2479–2501.

Schmidt, O. T. and Colonius, T. (2020). Guide to spectral proper orthogonal decomposition. *AIAA Journal*, 58(3):1023–1033.

Seydel, R. (2010). *Practical Bifurcation and Stability Analysis*. Springer, 3 edition.

Shuja, S., Yilbas, B., and Rashid, M. (2003). Confined swirling jet impingement onto an adiabatic wall. *International Journal of Heat and Mass Transfer*, 46(16):2947–2955.

Sieber, M. (2021). *Data-driven identification and modelling of coherent dynamics in turbulent flows*. PhD thesis, Technische Universitat Berlin.

Sieber, M., Paschereit, C. O., and Oberleithner, K. (2016). Spectral proper orthogonal decomposition. *Journal of Fluid Mechanics*, 792:798–828.

Sierra-Ausin, J., Citro, V., Giannetti, F., and Fabre, D. (2022). Efficient computation of time-periodic compressible flows with spectral techniques. *Computer Methods in Applied Mechanics and Engineering*, 393:114736.

Simpson, R. L. (2001). Junction flows. *Annual Review of Fluid Mechanics*, 33:415.

Singh, A. and Narasimhamurthy, V. D. (2018). Perforated bluff-body wake simulations: Influence of aspect ratio. In *2018 IEEE 25th International Conference on High Performance Computing Workshops (HiPCW)*, pages 32–35.

Singh, A. and Narasimhamurthy, V. D. (2021). Dns of wake from perforated plates: aspect ratio effects. *Progress in Computational Fluid Dynamics, an International Journal*, 21(6):355–368.

Singh, A. and Narasimhamurthy, V. D. (2022). Perforation effects on the wake dynamics of normal flat plates. *Journal of Fluid Mechanics*, 947:A23.

Sullivan, C. B. and Kaszynski, A. A. (2019). Pyvista: 3d plotting and mesh analysis through a streamlined interface for the visualization toolkit (vtk). *Journal of Open Source Software*, 4(37):1450.

Sychev, V. V., Ruban, A. I., Sychev, V. V., and Korolev, G. L. (1998). *Asymptotic Theory of Separated Flows (Trans. E.V. Maroko)*. Cambridge University Press.

Towne, A., Schmidt, O. T., and Colonius, T. (2018). Spectral proper orthogonal decomposition and its relationship to dynamic mode decomposition and resolvent analysis. *Journal of Fluid Mechanics*, 847:821–867.

Verma, S., Freeman, B. R. S., and Hemmati, A. (2022). Effects of reynolds number and average angle of attack on the laminar scaling of oscillating foils. *Phys. Fluids*, 34(3):031905.

Wang, H. F., Zhou, Y., and Mi, J. (2012). Effects of aspect ratio on the drag of a wall-mounted finite-length cylinder in subcritical and critical regimes. *Experiments in Fluids*, 53(2):423–436.

Wang, L., Pan, C., Wang, J., and Gao, Q. (2022). Statistical signatures of u component wall-attached eddies in proper orthogonal decomposition modes of a turbulent boundary layer. *Journal of Fluid Mechanics*, 944:A26.

Williamson, C. H. K. (1996). Vortex dynamics in the cylinder wake. *Annual Review of Fluid Mechanics*, 28(1):477–539.

Wu, S. J., Miau, J. J., Hu, C. C., and Chou, J. H. (2005). On low-frequency modulations and three-dimensionality in vortex shedding behind a normal plate. *Journal of Fluid Mechanics*, 526:117–146.

Appendix A

FANS Code

In this chapter, the code used in calculating the FANS terms for this thesis are presented. Section A.1 details custom OpenFOAM function objects for calculating the Navier-Stokes terms during postprocessing, and a Python utility for calculating the mean of an interval as an OpenFOAM field. Sections A.2 and A.3 display Python scripts including common simulation information and functions that feature in several pipeline scripts. The code would be executed starting with the script in Section A.4, which samples the fields found in the OpenFOAM directories. These samples would be processed using Fourier decomposition in the script in Section A.5. Important frequencies could then be screened with the code in Section A.6, and the FANS terms corresponding to interesting frequencies from screening are fully calculated using Section A.7. As well, functions and minimal examples for calculating the convection terms from the Fourier modes using the Python library PyVista (Sullivan and Kaszynski, 2019) is shown in Section A.8.

A.1 OpenFOAM postprocessing

Code for custom OpenFOAM functions to calculate spatial derivatives (ESI version, tested with OpenFOAM v2012). Part of an overall pipeline for obtaining data from OpenFOAM using Python.

```
functions
{
diffusion
{
    libs (utilityFunctionObjects);

    type coded;
    name diffusion;

    codeWrite
    #{
        // lookup U
        Info << "Looking␣up␣field␣U\n" << endl;
        const volVectorField& U = mesh().lookupObject<volVectorField>("U");
```

```
        Info << "calculating␣laplacian\n" << endl;
        const volVectorField lapU = fvc::laplacian(U);

        Info << "writing␣laplacian␣to␣" << lapU.objectPath() << endl;
        lapU.write();
    #};

    executeControl writeTime;
    executeInterval 1;
    writeControl writeTime;
    writeInterval 1;
}

convection
{
    libs (utilityFunctionObjects);

    type coded;
    name convection;

    codeWrite
    #{
        // lookup U, phi
        const volVectorField& U = mesh().lookupObject<volVectorField>("U");

        const surfaceScalarField phi
        (
            IOobject
            (
                "phi",
                mesh().time().timeName(),
                U.mesh(),
                IOobject::READ_IF_PRESENT,
                IOobject::NO_WRITE
            ),
            fvc::flux(U)
        );

        Info << "calculating␣divergence\n" << endl;
        const volVectorField divPhiU = fvc::div(phi, U);

        divPhiU.write();
    #};
    executeControl writeTime;
    executeInterval 1;
    writeControl writeTime;
    writeInterval 1;
```

```
}

gradP
{
    type grad;
    libs (fieldFunctionObjects);
    field p;
    executeControl writeTime;
    executeInterval 1;
    writeControl writeTime;
    writeInterval 1;
}

convecOfMean
{
    libs (utilityFunctionObjects);

    type coded;
    name convecOfMean;

    codeWrite
    #{
        // lookup U, phi
        const volVectorField& U = mesh().lookupObject<volVectorField>("U");
        const volVectorField UMean
        (
            IOobject
            (
                "UMeanFinal",
                mesh().time().timeName(),
                U.mesh(),
                IOobject::MUST_READ,
                IOobject::NO_WRITE
            ),
            mesh()
        );

        const surfaceScalarField phi
        (
            IOobject
            (
                "phi",
                mesh().time().timeName(),
                U.mesh(),
                IOobject::READ_IF_PRESENT,
                IOobject::NO_WRITE
            ),
```

```
            fvc::flux(U)
        );

        Info << "calculating convection of mean field by transient\n" << endl;
        const volVectorField divPhiU = fvc::div(phi, UMean);

        divPhiU.write();
    #};

    executeControl writeTime;
    executeInterval 1;
    writeControl writeTime;
    writeInterval 1;
}

convecByMean
{
    libs (utilityFunctionObjects);

    type coded;
    name convecByMean;

    codeWrite
    #{
        // lookup U, phi
        const volVectorField& U = mesh().lookupObject<volVectorField>("U");
        const volVectorField UMean
        (
            IOobject
            (
                "UMeanFinal",
                mesh().time().timeName(),
                U.mesh(),
                IOobject::MUST_READ,
                IOobject::NO_WRITE
            ),
            mesh()
        );
        const surfaceScalarField phiMean
        (
            IOobject
            (
                "phiMeanFinal",
                mesh().time().timeName(),
                U.mesh(),
                IOobject::READ_IF_PRESENT,
                IOobject::NO_WRITE
```

```
            ),
            fvc::flux(UMean)
        );


        Info << "calculating convection of transient field by mean\n" << endl;
        const volVectorField divPhiU = fvc::div(phiMean, U);

        divPhiU.write();
    #};

    executeControl writeTime;
    executeInterval 1;
    writeControl writeTime;
    writeInterval 1;
}
};
```

These functions require a field UMeanFinal, representing the actual mean of the interval in question, written in every directory. This can be calculated using PyFOAM as follows:

```
import numpy as np
from copy import deepcopy
import pickle
from PyFoam.RunDictionary.ParsedParameterFile import ParsedParameterFile
from PyFoam.RunDictionary.SolutionDirectory import SolutionDirectory


t_end = 603.45  # end of window
t_start = 0  # start of window
t0 = 0  # start of mean calculation

UMeanFinal = ParsedParameterFile(f'{t_end}/UMean')
UMeanRunIn = ParsedParameterFile(f'{t_start}/UMean')

# extract values for calculation
def convert_list(field):
    return np.array([
        str(fi).strip('(').strip(')').split(' ')
        for fi in field
    ]).astype(float)

UMeanEstimated = deepcopy(UMeanFinal)

# estimate
internalFieldEstimate = (
    (t_end-t0)*convert_list(UMeanFinal['internalField'])
    - (t_start-t0)*convert_list(UMeanRunIn['internalField'])
) / (t_end - t_start)
```

```
# format and replace internal field values
for i in range(len(UMeanEstimated['internalField'])):
    UMeanEstimated['internalField'][i] = (
        f'({internalFieldEstimate[i]})'
        .replace('[', '')
        .replace(']', '')
    )

UMeanEstimated.header['object'] = 'UMeanFinal'

# Write to directories
sol = SolutionDirectory('.')

UMeanEstimated.writeFileAs(f'{t_end}/UMeanFinal')
```

The remainder of this pipeline consists of the following scripts:

A.2 common.py

```
from collections import namedtuple
from pathlib import Path
import pickle

import numpy as np

def load(path):
    with open(path, 'rb') as file:
        q = pickle.load(file)
    return q


def save(obj, path):
    with open(path, 'wb') as file:
        pickle.dump(obj, file)

UINF = 1
HEIGHT = 1
Re = 250
NU = UINF * HEIGHT / Re
WIDTH = 6.28
THICKNESS = .02

fields = [
    'U',
    'convection(phi,U)',
```

```
    'convection(phi,UMeanFinal)',
    'convection(phiMeanFinal,U)',
    'grad(p)',
    'laplacian(U)'
]
scaling = {
    'U': 1/UINF,
    'convection(phi,U)': HEIGHT/UINF**2,
    'convection(phi,UMeanFinal)': HEIGHT/UINF**2,
    'convection(phiMeanFinal,U)': HEIGHT/UINF**2,
    'grad(p)': HEIGHT/UINF**2,
    'laplacian(U)': HEIGHT**2 / UINF
}
```

A.3 util.py

```
import linecache
import matplotlib.pyplot as plt
import numpy as np
from scipy.interpolate import griddata


def read_vector(fname, start, nrows):
    """read vector field at a timestep into numpy, e.g. U, grad(p)"""

    tab = np.loadtxt(fname, dtype=float, skiprows=start, max_rows=nrows,
                     converters={
                         0: lambda s: float(s[1:]),
                         1: lambda s: float(s),
                         2: lambda s: float(s[:-1])
                     })
    return tab.T


def read_scalar(fname, start, nrows):
    """read scalar data file at a timestep"""
    tab = np.loadtxt(fname, dtype=float, skiprows=start, max_rows=nrows,)

    return tab


def nearest(array, value, idx=False):
    """return entry in array that is nearest to value"""
    arg = np.argmin(np.abs(array-value))
    if idx:
        return array[arg], arg
```

```
    else:
        return array[arg]
```

A.4 sample_data.py

```
from collections import defaultdict
import gzip as gz
from pathlib import Path
from time import time

import numpy as np

import common as com
import util

# ------- INPUTS ---------
# path to openfoam data
SAMPLES_PATH = Path('.')
# path to save to
SAVE_PATH = Path('data/')

LATEST_TIME = '603.45'
# path to raw cell center data
CELL_PATH = SAMPLES_PATH / LATEST_TIME / 'C.gz'
# whether or not to generate a new random sample
GENERATE_SAMPLE = False
# which fields to load, downsample, and save
SAMPLE_FIELDS = com.fields
# overwrite files without asking
OVERWRITE = True

t_start = 0

# startline of internalField
start = 23
with gz.open(CELL_PATH) as f:
    for i in range(21):
        f.readline()
    nrows = int(f.readline()[:-1])

# allow for startlines that may not be consistent from field to field
startline = defaultdict(lambda: start)

# Find a set of points to sample and save those points
# A random sample is generated, but the random seed is fixed
# so that it gives consistent results
```

```
if GENERATE_SAMPLE:

    cell_centres = util.read_vector(CELL_PATH, start, nrows)
    n_total = cell_centres.shape[1]
    rng = np.random.default_rng(seed=0)

    # generate sample - subregion of field can be isolated optionally
    sample = rng.choice(
        np.argwhere(
            (cell_centres[0] <= 20) & (np.abs(cell_centres[1]) < 5)
        ).flatten(),
        size=n_total//5,
        replace=False
    )

    com.save(sample, SAVE_PATH/'sample_points')

    c_sample = cell_centres[:, sample] / com.HEIGHT
    x = c_sample[0]
    y = c_sample[1]
    z = c_sample[2]
    com.save(x, SAVE_PATH/'x')
    com.save(y, SAVE_PATH/'y')
    com.save(z, SAVE_PATH/'z')

else:
    sample = com.load(SAVE_PATH/'sample_points')

n_cells = len(sample)

vol = util.read_scalar(SAMPLES_PATH/LATEST_TIME/'V.gz', start, nrows)
com.save(vol[sample], SAVE_PATH/'vol')

# find and filter data folders
data_folders = [
    path
    for path in SAMPLES_PATH.iterdir()
    if (
        path.is_dir()
        & path.stem.isnumeric()
        & (path/'UMeanFinal.gz').exists()
    )
]

data_folders = [path for path in data_folders if int(path.stem) > t_start]

# extract and save field data
```

```
n_steps = len(data_folders)
t = np.array([float(folder.name) for folder in data_folders])
t_order = np.argsort(t)
t = t[t_order]
com.save(t, SAVE_PATH/'t')

for field_name in SAMPLE_FIELDS:
    if not OVERWRITE:
        if (SAVE_PATH/field_name).exists():
            overwrite = input(
                f'A␣sample␣of␣{field_name}␣already␣exists.␣Overwrite?␣[y]/n'
            )
            if overwrite == 'n':
                continue  # skip this field

    sampled_field = np.zeros((n_steps, 3, n_cells))
    print('reading␣', field_name)
    total = len(data_folders)

    t0 = time()
    for (i, folder) in enumerate(data_folders):
        try:
            field = util.read_vector(
                folder/field_name,
                startline[field_name],
                nrows
            )
            sampled_field[i] = field[:, sample] * com.scaling[field_name]

        except:
            field = util.read_scalar(
                folder/field_name,
                startline[field_name],
                nrows
            )
            sampled_field[i] = field[sample] * com.scaling[field_name]

        print(f'{i}/{total},␣{folder},␣{time()␣-␣t0:.2f}')

    del field

    sampled_field = sampled_field[t_order]

    com.save(sampled_field, SAVE_PATH/field_name)
```

A.5 fourier_decomp.py

```
import gzip as gz
from pathlib import Path
import pickle
from time import time

import matplotlib.pyplot as plt
import numpy as np

from common import *
import util

NEW_DECOMP = True
SAVE_PATH = Path('data/')

# load time
t = load(SAVE_PATH/'t')
# set window
window = t > 0

fields = {
    'convection(phi,U)': 'div(u,u)hat',
    'convection(phiMeanFinal,U)': 'div(U,u)hat',
    'convection(phi,UMeanFinal)': 'div(u,U)hat',
    'laplacian(U)': 'Lhat',
    'grad(p)': 'Phat'
}

def get_spectrum_and_compress(Q, dt, n, vol=1):
    """load data, take the real fft, and sample number of modes"""

    n_samples = Q.shape[0]

    f = np.fft.rfftfreq(n_samples, d=dt)

    Qhat = np.zeros(f.shape + Q.shape[1:], dtype=complex)
    mode_energy = np.zeros(f.shape)
    t0 = time()
    n_points = Q.shape[2]

    for i in range(n_points):
        Qhat[:, :, i] =  np.fft.rfft(Q[:, :, i], axis=0) / n_samples

        mode_energy += vol[i] * np.sum(np.abs(Qhat[:, :, i])**2, axis=1)

        if i % (n_points//10) == 0:
```

```
            print(
                f'{i/n_points*100:.1f}% complete ({time() - t0:.1f} s)'
            )


    mode_order = np.argsort(mode_energy)[::-1]

    f_idx = mode_order[:n]
    f_keep = f[f_idx]

    energy_residual = np.sum(mode_energy[f_idx]) / np.sum(mode_energy)

    print(
        f'selected modes contain '
        +'{energy_residual*100:.5f}% '
        +'of the total energy'
    )

    return f_keep, f_idx, Qhat[f_idx]


def apply_dynamics(Q, f_idx, vol):
    n = Q.shape[0]
    Q_mean = np.mean(Q, axis=0)
    # print(dyn.shape, Q.shape)
    Qhat = np.zeros((len(f_idx),) + Q.shape[1:], dtype=complex)
    spectrum_energy = 0
    Raa = 0
    n_points = Qhat.shape[2]
    t0 = time()
    for i in range(n_points):
        Qhat[:, :, i] = np.fft.rfft(Q[:, :, i], axis=0)[f_idx] / n
        spectrum_energy += 2*np.sum(
                vol[i]*np.abs(Qhat[1:, :, i])**2
            )
        Raa += np.sum(vol[i]*(Q[:, :, i]-Q_mean[:, i])**2) / n

        if i % (n_points//10) == 0:
            print(f'{i/n_points*100:.1f}% complete ({time() - t0:.1f} s)')


    energy_residual = spectrum_energy / Raa
    print(
        f'selected modes contain '
        + '{energy_residual*100:.5f}% '
        + 'of the fluctuating energy'
    )
```

```
    return Qhat


def load_decompose_erase(loc, window, f_idx, vol):

    q = load(loc)[window]
    qhat = apply_dynamics(q, f_idx, vol)
    return qhat


def load_transform_erase(loc, window, dt, n, vol):
    q = load(loc)[window]
    f, f_idx, qhat = get_spectrum_and_compress(q, dt, n, vol)
    return f, f_idx, qhat

dt = np.median(np.diff(t))
vol = load(SAVE_PATH/'vol')


if NEW_DECOMP:
    # decompose velocity field and keep only some frequencies
    print('Getting U dynamics')
    f, f_idx, uhat = load_transform_erase(
        SAVE_PATH/'U',
        window,
        dt,
        int(np.sum(window)/2),  # keep half the data
        vol
    )
    print('saving f')
    save(f, SAVE_PATH/'f')
    save(f_idx, SAVE_PATH/'f_idx')

    print('saving uhat')
    save(uhat, SAVE_PATH/'uhat')
    del uhat

else:
    # load previously saved frequencies
    print('loading frequencies to save')
    f_idx = load(SAVE_PATH/'f_idx')

for field, name in fields.items():
    print(f'decomposing {field} ({name})')
    try:
        qhat = load_decompose_erase(SAVE_PATH/field, window, f_idx, vol)
```

```
        save(qhat, SAVE_PATH/name)

        del qhat
    except pickle.UnpicklingError:
        print(field, ' is corrupted')
```

A.6 screen_frequencies.py

```
from multiprocessing import Pool
from pathlib import Path

import matplotlib.pyplot as plt
plt.rcParams['font.family'] = 'serif'
import numpy as np
from scipy.spatial import Delaunay

from common import *
from util import nearest
SAVE_PATH = Path('data/')


print('loading data')

t = load(SAVE_PATH/'t')
x = load(SAVE_PATH/'x')
y = load(SAVE_PATH/'y')
z = load(SAVE_PATH/'z')

# complete list of frequencies
f = load(SAVE_PATH/'f')
n_f = len(f)

uhat = load(SAVE_PATH/'uhat')

vol = load(SAVE_PATH/'vol')

print('find highest energy modes')
mode_energy = np.zeros(n_f)
for i in range(n_f):
    mode_energy[i] = np.sum(vol*np.abs(uhat[i])**2)

energy_order = np.argsort(mode_energy)[::-1]

plt.figure(figsize=(3,3))
plt.plot(f, mode_energy, 'k.')
plt.yscale('log')
```

```
plt.xlabel('$f^*$')
plt.ylabel(r'$\vert␣\hat{u}\vert^2')
plt.savefig('figure/mode_energy.pdf', bbox_inches='tight')
plt.close()
```

A.7 terms.py

In this script the actual Fourier terms at frequencies selected from screening are calculated, which can then be saved or used in visualizations.

```
from pathlib import Path

import numpy as np

from common import *
from util import nearest

SAVE_PATH = Path('data/')

t = load(SAVE_PATH/'t')
x = load(SAVE_PATH/'x')
y = load(SAVE_PATH/'y')
z = load(SAVE_PATH/'z')

# complete list of frequencies
f = load(SAVE_PATH/'f')

# list of estimated interesting frequencies from screening
freq_list = [0, 0.1660, 0.3319]

# index of estimated frequencies in complete liist
freq_idx = np.array([
    nearest(f, freq, idx=True)[1]
    for freq in freq_list
])

# selected frequencies
f_selected = f[freq_idx]
uhat = load(SAVE_PATH/'uhat')
P = load(SAVE_PATH/'Phat')[freq_idx]
D = load(SAVE_PATH/'Lhat')[freq_idx] / Re
C = load(SAVE_PATH/'div(U,u)hat')[freq_idx]
C[1:] += load(SAVE_PATH/'div(u,U)hat')[freq_idx[1:]]
chi = load(SAVE_PATH/'div(u,u)hat')[freq_idx]
chi -= C
T = -P - chi - C + D
```

```
fields = {
    '$T$': T,
    '$P$': P,
    '$D$': D,
    r'$\chi$': chi,
    '$C$': C
}
```

A.8 convection.py

Alternatively, if the gradients are not available, the FANS terms can be calculated through numerical differentiation on the modes:

```
from pathlib import Path

import matplotlib.pyplot as plt
plt.rcParams['text.usetex'] = True
plt.rcParams['font.family'] = 'serif'
plt.rcParams['mathtext.fontset'] = 'cm'
from matplotlib.ticker import LinearLocator, PercentFormatter
import numpy as np
import pyvista as pv
from scipy.interpolate import LinearNDInterpolator
from scipy.spatial import Delaunay
import vtk

from common import *


BASE_PATH = Path('data')

x = load(BASE_PATH/'x')
y = load(BASE_PATH/'y')
z = load(BASE_PATH/'z')


def pyvista_convection(surf, q, U):

    surf.point_data['qU'] = (q*U).T
    div = surf.compute_derivative(
        scalars='qU',
        gradient=False,
        divergence='div_qU'
    )

    return div.point_data['div_qU']
```

```
def convection_components(surf, q, U):
    """calculate terms U dx q, V dy q, W dz q as a vector"""
    surf.point_data['q'] = q
    grad = surf.compute_derivative(
        scalars='q',
        gradient='grad_q'
    )

    grad_q = grad.point_data['grad_q']

    return grad_q*U.T


# Construct Delaunay triangulation
tri = Delaunay(np.array([x, y, z]).T)

# convert Delaunay simplices to pyvista cell representation
cells = []
for simplex in tri.simplices:
    cells += [len(simplex)] + list(simplex)
cells = np.array(cells)

# assign cell types (all tetras)
cell_types = np.array([vtk.VTK_TETRA]*len(tri.simplices))

# construct pyvista ugrid
ugrid = pv.UnstructuredGrid(cells, cell_types, tri.points)

uhat = load(BASE_PATH/'uhat')

UMean = np.real(uhat[0])

# examples of calculating convective fluxes with pyvista
UU_est = pyvista_convection(ugrid, UMean[0], UMean)

Uv_real = pyvista_convection(ugrid, np.real(uhat[1,1]), UMean)

Uv_imag = pyvista_convection(ugrid, np.imag(uhat[1,1]), UMean)
```